



## THESIS / THÈSE

### DOCTOR OF SCIENCES

#### Electronic and magnetic properties of MoS<sub>2</sub> sheets and nanoribbons subjected to external perturbations

Castenetto, Pauline

*Award date:*  
2024

*Awarding institution:*  
University of Namur

[Link to publication](#)

#### General rights

Copyright and moral rights for the publications made accessible in the public portal are retained by the authors and/or other copyright owners and it is a condition of accessing publications that users recognise and abide by the legal requirements associated with these rights.

- Users may download and print one copy of any publication from the public portal for the purpose of private study or research.
- You may not further distribute the material or use it for any profit-making activity or commercial gain
- You may freely distribute the URL identifying the publication in the public portal ?

#### Take down policy

If you believe that this document breaches copyright please contact us providing details, and we will remove access to the work immediately and investigate your claim.

---

# Electronic and magnetic properties of $\text{MoS}_2$ sheets and nanoribbons subjected to external perturbations

---

**Castenetto Pauline**

Thèse présentée en vue de l'obtention du grade de docteur en sciences

Soutenue le 9 janvier 2024, devant le jury composé de :

<b>Pr. COLOMER</b> Jean-François	- Président
<b>Pr. HENRARD</b> Luc	- Promoteur
<b>Pr. LAMBIN</b> Philippe	- Co-promoteur
<b>Pr. CHARLIER</b> Jean-Christophe	- Examineur
<b>Pr. SPORKEN</b> Robert	- Examineur
<b>Pr. VANCSÓ</b> Péter	- Examineur

**Année universitaire 2023-2024**

# Abstract

Comprehensive research on electronic and spintronic properties of graphene and MoS<sub>2</sub> has been the focus of scientific attention for several years and still is. An important issue, however, is the presence of defects that can influence these. In the case of MoS<sub>2</sub>, experiments have demonstrated that edges (1D defect) can host local magnetic moments. However the computational cost of the ab-initio DFT calculations for experimentally relevant system size is a downside.

In this work, we first apply tight-binding numerical simulations to reproduce the band-structure of monolayer, bilayer, trilayer and bulk MoS<sub>2</sub> 2H and 3R and of monomolecular zigzag asymmetric MoS<sub>2</sub> nanoribbons whose edge terminated by Mo atoms is passivated with sulfur dimers. The tight-binding Hamiltonian proposed by E. Cappelluti and al [Physical Review B 88, 075409 2013] is used for the planar structures. We have shown that sulfur vacancies in monolayer MoS<sub>2</sub> induce gap states in the electronic band structures. We have investigated theoretically the magnetic properties for several nanometers long MoS<sub>2</sub> nanoribbons with zigzag edges using fine-tuned parameters in a tight-binding (TB)-Hubbard Hamiltonian. We could successfully reproduce the metallic state induced by the edges, compute large-scale nanoribbons and predict the spin domain-wall energy as well as study the effect of edge disorders on the magnetic properties. Besides the full TB parametrization of the nanoribbon, we also described the bands crossing the Fermi level with a one-dimensional linear chain model, allowing us to easily compare ferromagnetic and anti-ferromagnetic configurations and giving us a useful tool to study the energy cost for switching spins on various spots and scales. This model can be useful to study the stability and the properties of real size nanoribbons presenting spin defects and their applications.



Science isn't about why, it's about why not.

- *Cave Johnson (Portal)*



# Acknowledgements

First and foremost, I would like to express my gratitude to my supervisor, Pr. Philippe Lambin, for his unwavering support, valuable advice, flexibility and guidance throughout my entire PhD. His calm strength has been a guiding light during challenging moments and his humane approach to management has been truly invaluable. I will miss his ability to explain complex concepts in the most understandable way. Words come short to express my gratitude for always supporting me, both in the scientific and teaching fields.

I also would like to extend my thank Pr. Luc Henrard for his support and advice particularly for his attentive and prompt proofreading as well as for being that little voice reminding me of deadlines and setting limits when necessary.

I'd also like to thank Péter Vancsó for his eternal kindness and availability. I will never cease to be impressed by the depth of his scientific insights and his laughter and infectious good humour have been invaluable over the years.

I would like to thank all my present or past colleagues, whether in my laboratory or others, in teaching, technical services or administration, with whom I have had rich and/or funny exchanges, making going to the office a pleasure. While I can't list everyone, they will surely recognize themselves. Their kind support and assistance provided along all these years were precious. I will miss our moments of grumbling together.

I'd also like to thank all the students I've met over the years. The exchanges with them have been invaluable and a real motivation to constantly improve. It's been a real pleasure to have the opportunity to teach them a little of what I know and I hope I've been able to help them develop into 'good' scientists.

I want to thank my friends from physics or other fields who have contributed morally to the existence of this thesis and who still had the courage to ask for news. A special acknowledgment goes to David for his support over the years. Our scientific exchanges on my thesis topic helped me to present it in an understandable way and his help in combating my procrastination was precious.

Last but not least, an infinite thank you to my family, who have always been there to support me. Thank you for waking me up when I wasn't feeling well, for listening to me moan for hours when I needed to get things off my chest, for your unfailing support at all times, for the endless and precious discussions about teaching and human beings, and for believing in me more than I believed in myself. Without you, this thesis wouldn't exist.

# Contents

<b>1</b>	<b>Introduction</b>	<b>9</b>
<b>2</b>	<b>Physical properties of TMD-based 2D materials</b>	<b>13</b>
2.1	Introduction . . . . .	13
2.2	TMDs . . . . .	14
2.2.1	Planar structures . . . . .	14
2.2.2	Electronic properties . . . . .	16
2.2.3	Optical properties . . . . .	18
2.2.4	Magnetism and spintronic . . . . .	19
2.3	Nanoribbons of TMDs . . . . .	20
2.3.1	Structure . . . . .	20
2.3.2	Properties . . . . .	23
<b>3</b>	<b>Computational methods</b>	<b>27</b>
3.1	Density Functional Theory . . . . .	27
3.2	Tight-binding theory . . . . .	28
3.3	Tight-binding models for TMDs . . . . .	33
3.4	Hubbard model . . . . .	34
<b>4</b>	<b>Tight-binding parametrization from DFT calculations</b>	<b>39</b>
4.1	Sheets of MoS <sub>2</sub> and WS <sub>2</sub> . . . . .	39
4.2	Zigzag MoS <sub>2</sub> nanoribbons with sulfur dimer passivation of the Mo edge . . .	46

<b>5</b>	<b>Defects and disorder</b>	<b>51</b>
5.1	Domain wall in nanoribbons . . . . .	51
5.2	Local perturbations in nanoribbons . . . . .	53
5.3	Atomic vacancies in nanosheets (ongoing) . . . . .	58
<b>6</b>	<b>Magnetic order in MoS<sub>2</sub> nanoribbons</b>	<b>63</b>
6.1	One-dimensional atomic chain model . . . . .	63
6.2	Magnetic configurations and energetics of the atomic chain . . . . .	65
6.3	Bloch wall and small Bloch domains . . . . .	69
<b>7</b>	<b>Conclusion</b>	<b>75</b>
<b>A</b>	<b>Spherical harmonics and matrix elements</b>	<b>79</b>
<b>B</b>	<b>Linear chain in mean field approximation</b>	<b>83</b>
<b>C</b>	<b>Spin flip in a ferromagnetic linear chain</b>	<b>89</b>

# Chapter 1

## Introduction

The groundbreaking synthesis of graphene, the first single-atom thick material, in 2004 by Novoselov and Geim [1,2] has ignited a surge in research on atomically thin two-dimensional (2D) materials, raising the interest in their fundamental properties and potential applications. Distinguished by their inherent flexibility, strength, and extreme thinness, 2D materials exhibit phenomena vastly different from their bulk counterparts. Their unique composition, being entirely made up of their surface, makes them susceptible to alterations in properties due to the interface between the surface and the substrate, as well as the presence of adatoms and defects. The advancement of 2D materials is anticipated to revolutionize current device technology and offer new prospects for spintronic devices and quantum computing [3,4,5]. Extensive research on graphene and other two-dimensional atomic crystals has yielded diverse methods for synthesis, transfer, detection, characterization, and manipulation of their properties [3,6]. Although the electronic mobility of graphene at room temperature has boosted proposals for graphene-based electronic devices [7], a challenge lies in the absence of a gap in pristine monolayer samples and the difficulty in opening a gap in multilayer systems without compromising mobility. An alternative path involves reassembling isolated atomic planes into precisely sequenced heterostructures layer by layer, known as 'van der Waals' heterostructures, showcasing unique properties and phenomena [3]. The ability to manipulate and reassemble single atomic layers, forming heterostructures in a precise sequence, presents vast possibilities for applications [3,8,9,10].

Researchers are also increasingly directing their attention towards other 2D atomic crystals, including isolated monolayers and few-layer crystals. However, many theoretically stable 2D crystals face challenges in real-world applications due to issues such as corrosion, decomposition, segregation, contamination, and oxidation. Notable exceptions, such as semiconducting dichalcogenides, stand out as promising compounds since they can be easily

exfoliated and maintain a suitable small gap in both bulk and single-layer forms. Additionally, layers of hexagonal boron nitride (hBN), molybdenum disulfide ( $\text{MoS}_2$ ), and other dichalcogenides have demonstrated stability under ambient conditions [3].

In 2D dichalcogenides systems, monolayers of molybdenum disulfide ( $\text{MoS}_2$ ) have recently gained attention for their ability to mix an electron mobility comparable to that of graphene devices with a finite energy gap [11]. Monolayer  $\text{MoS}_2$  has a direct gap unlike its bulk form which is an indirect semiconductor, undergoing a transition from an indirect band gap of 1.3 eV in its bulk structure to a direct band gap of 1.8 eV in the monolayer configuration. [3,11]. This direct band gap, with the valence band maximum and conduction band minimum localised at the K point of the Brillouin zone, falls within the visible frequency range, making it particularly favorable for optoelectronic applications [11].

Recently, 2D atomic crystals have emerged as a promising alternative to bulk semiconductors for modulating optical properties in photonic applications [12,13]. In the case of graphene, changes in optical absorption exceeding 100% induced by the electric field effect have been harnessed to showcase nanoscale electro-optical modulators in the infrared range [14]. However, the lack of a band gap in pristine graphene makes it unpractical for application at visible frequencies. In the case of monolayer dichalcogenides like  $\text{MoS}_2$ , electrical control of photoluminescence quantum yield and absorption coefficient in the visible range has been demonstrated [15]. The importance of many-body interactions in monolayer  $\text{MoS}_2$  is crucial. In particular, the optical properties are dominated by excitonic transitions [16].

Furthermore, these 2D materials exhibit intriguing thermal and thermoelectrical properties. Due to the absence of interlayer phonon scattering, the anticipated thermal conductivity in ideal conditions is expected to surpass the values observed in bulk. Another noteworthy characteristic is the high sensitivity of their electronic properties to external factors such as pressure [17], strain [18,19,20], and temperature [21]. These external influences not only impact the energy gap but, under specific conditions, can also trigger an insulator-to-metal transition. Moreover, the absence of lattice inversion symmetry, coupled with spin-orbit coupling (SOC), results in intertwined spin and valley physics within monolayers of  $\text{MoS}_2$  and other group-VI dichalcogenides [13]. This unique combination enables the manipulation and control of spin and valley properties in these materials [9,22].  $\text{MoS}_2$  monolayers have been suggested for a wide variety of nanoelectronics applications due to their distinctive band structures, such as valleytronics, spintronics, optoelectronics and room temperature transistor [8,9,23].

The interest in the electronic and mechanical properties of graphene and other 2D materials has also triggered an intense investigation and production efforts focusing on nanowires

and nanoribbons. As in graphene, the presence of edges modifies the band structure of monolayer TMDs. The necessity of a simple framework to study the electronic properties of nanoribbons of MoS<sub>2</sub> arises from these observations and motivated us to create the model used in this thesis.

While much of the theoretical work on graphene has employed tight-binding-like approaches, the exploration of the electronic properties of single-layer, few-layer, and nanoribbon dichalcogenides has primarily been based on *ab initio* calculations, based on Density Functional Theory (DFT) [22,18]. Although these methods give valuable insights of the electronic properties of pristine dichalcogenide crystals, their computational demands become prohibitive when dealing with disordered systems comprising a large number of atoms. A simpler model is then used to be able to tackle larger systems. One of the commonly used, and the one used in this thesis, is the tight-binding approximation. From a computational standpoint, tight-binding models exhibit high scalability, rendering them well-suited for the analysis of large structures, both ordered and disordered. Moreover, the tight-binding model finds application not only in single-layer MoS<sub>2</sub> but also in similar transition metal dichalcogenides.

In recent years, several tight-binding models have been put forth for MoS<sub>2</sub> monolayers [24,25,26,27,28]. We chose one that is a good compromise in the choice of the number of parameters between accuracy and lightness of calculation. We use the tight-binding model shown in ref [27,28] to replicate the band structures of MoS<sub>2</sub> and WS<sub>2</sub> layers obtained by DFT. Then we expand the TB parameters and use a local Coulomb interaction to systematically study the electronic and magnetic properties of MoS<sub>2</sub> zigzag nanoribbons. Our calculations reproduce qualitatively the band structure of nanoribbons obtained by DFT. We show the necessity to take into account the different environment of the edge atoms to reproduce the DFT calculations. Both DFT and Hubbard (TB+U) methods reveal that one band crossing the Fermi level is more strongly influenced by spin polarization than any other bands. The dispersion of this band, originating from states localized on the sulfur edge of the nanoribbon, closely resembles the one of the energy branch obtained in a linear chain of atoms with first-neighbour interaction. We propose a toy model to study the energetics of different spin configurations of the nanoribbon edge.

The development of a concise and efficient representation of band structures, combined with a simplified model facilitating the analysis of energetics in various spin configurations of nanoribbons, sets the stage for advanced calculations. These calculations can incorporate external factors like mechanical stresses and defects. The observed alteration of spin texture induced by a Gaussian perturbation can replicate effects produced by an STM tip, suggest-

ing potential applications in spintronics, among other fields. The promising results obtained for sulfur vacancies indicate a positive outlook for exploring other defects or adatoms. Furthermore, recent advancements in machine learning have opened the door to an enhanced parametrization of TB, offering the possibility of even more accurate quantitative reproduction of MoS<sub>2</sub> band structures [29].

This thesis is structured as follow:

Chapter 2 describes the crystal and the physical properties of transition metal dichalcogenides (TMDs). A description of the structures of the studied materials as well as a review of the main electronic, magnetic and optical properties is presented.

Chapter 3 presents the computational methods used in this work : DFT, TB theory and Hubbard model. The description is developed in the case of TMDs. For TB, we review the models found in literature and motivate our choice. The DFT band structure calculations shown in this work have been performed by Péter Vancsó from the Institute of Technical Physics and Materials Science in Budapest.

Chapter 4 presents the tight-binding parametrization used for sheets of MoS<sub>2</sub> and WS<sub>2</sub> as well as for zigzag MoS<sub>2</sub> nanoribbons with sulfur dimer passivation of the Mo edge. The band structures obtained from these parametrization are shown and discussed as well as the impact of spin polarization.

Chapter 5 discusses the impact of defects and disorder on MoS<sub>2</sub>. More precisely, we predict the domain wall in nanoribbons, compare it with graphene nanoribbons and study the effect of edge disorder on the magnetic properties. An ongoing work about atomic vacancies in nanosheets is also shown.

Chapter 6 contains a one-dimensional atomic chain model for the magnetic order in MoS<sub>2</sub> nanoribbons. Indeed, the band strongly affected by spin-polarization crossing the Fermi level has a dispersion close to the one from a linear chain of atoms. The magnetic configurations and energetics of the atomic chain is studied. We computed the formation energy of a Bloch wall and focused on smaller Bloch domains (that can appear as the consequence of a local perturbations of the on-site energies) to estimate the excitation energies of different arrangements of the magnetic moments.

# Chapter 2

## Physical properties of TMD-based 2D materials

### 2.1 Introduction

For over a decade, graphene has been the most coveted two-dimensional material due to its notable features including high charge mobility and unique properties (such as the presence of a linear energy dispersion relation with respect to the momentum at the Dirac points, similar to photons) [30,31]. However, a major drawback for several applications of graphene on nanoelectronics is its lack of a band gap for a monolayer. It is therefore challenging to introduce one in a doped monolayer or in a multilayer system without impacting the electron mobility [32]. Nevertheless, graphene nanoribbons show a band gap, a discovery that has fuelled research into this type of structure.

On the other hand, transition metal dichalcogenides (TMDs) have a band gap, making them a significant focus of research efforts for semiconductor and optical applications. Group-VI TMDs exhibit a direct bandgap in monolayers and an indirect, relatively smaller bandgap in multilayers [31]. Consequently, numerous laboratories have been exploring TMDs for various applications, including the development of transistors [4]. It is essential to have a material with a band gap of at least 0.4 eV, enabling the production of field-effect transistors with an ON and OFF current ratio of between  $10^4$  and  $10^7$  [5,23]. Furthermore, TMDs in nanoribbon form have other very interesting properties (such as being a metallic material in the case of zigzag MoS<sub>2</sub> nanoribbons), making it a material that can be used in spintronics or in the advancement of battery technology for example.

In this section, we will conduct a comprehensive review of the current state of the art,

aiming to understand the interest in these two-dimensional materials, particularly focusing on MoS<sub>2</sub>.

## 2.2 TMDs

### 2.2.1 Planar structures

Molybdenum disulfide (MoS<sub>2</sub>) is a semiconducting, diamagnetic crystal. It crystallizes naturally in two polytypes: 2H (H for hexagonal), from  $P6_3/mmc$  group space, and 3R (R for rhombohedral), from  $R3m$  group space.

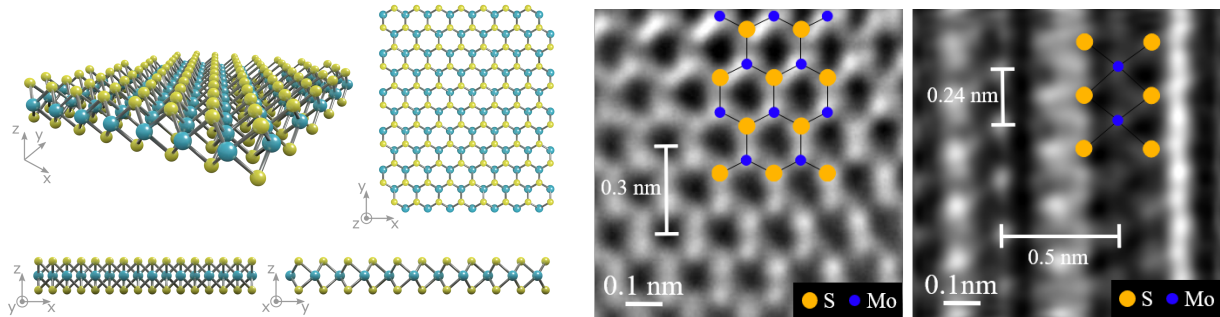


Figure 2.1: Crystal structure of a monolayer of MoS<sub>2</sub> [33] and STM pictures of MoS<sub>2</sub>, courtesy of Mr. Colomer

In its most stable 2H structure, MoS<sub>2</sub> is hexagonal as shown in figure 2.2. A monolayer of MoS<sub>2</sub> is essentially a remarkably thin layer comprising three atoms in height. This structure consists of a molybdenum atom plane enclosed between two sulfur atom planes, as depicted in figure 2.1. In the 2H configuration, the initial monolayer is overlaid by a second layer within the same unit cell. This subsequent layer has the same structure and is offset so that molybdenum atoms of the first layer are aligned with the sulfur atoms of the second. The layers are bound together by weak Van der Waals forces.

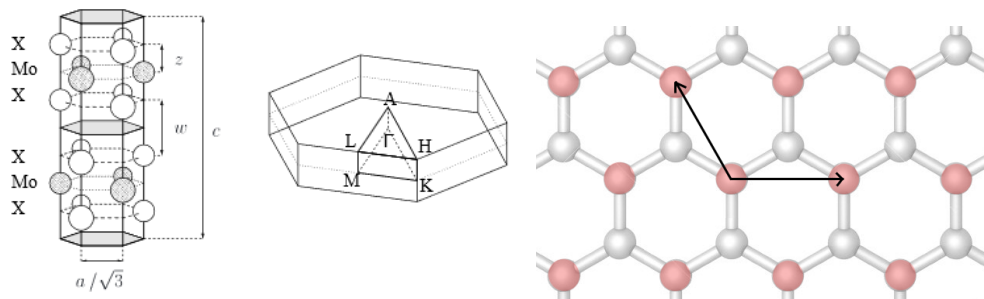


Figure 2.2: Crystal structure of MoS<sub>2</sub> 2H and first Brillouin zone [34]

For the 3R structure, the unit cell contains three main layers, all with the same structure as the main layers of the 2H polytype. The difference lies in the way they are arranged : each main layer is translated by  $1.82 \text{ \AA}$  in the plane of the layers, as shown in figure 2.3.

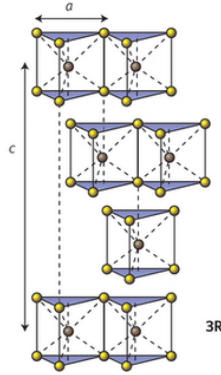


Figure 2.3: Crystal structure of MoS<sub>2</sub> 3R [35]

The distances separating the atoms are as follows [27,28]:

S-S or Mo-Mo first neighbors	$a = 3.16 \text{ \AA}$
Mo-S first neighbors	$b = 2.41 \text{ \AA}$
between Mo plane and S plane	$z = 1.586 \text{ \AA}$
between S planes of different nearest layers	$w = 2.968 \text{ \AA}$
between Mo planes of different layers	$c' = 6.14 \text{ \AA}$
2H unit cell height	$c = 12.28 \text{ \AA}$
3R unit cell height	$c = 18.42 \text{ \AA}$

The unit cell for a monolayer is thus defined with the directional vectors  $\vec{a}_1$  and  $\vec{a}_2$  as well as with the atomic position shown in table 2.1. The 2H and 3R configurations of MoS<sub>2</sub> can be effectively described by incorporating one or two additional layers of MoS<sub>2</sub>, each layer being offset at specific atomic positions to achieve the desired configuration.

	x (Å)	y (Å)	z (Å)
$\vec{a}_1$	a/2	$a\sqrt{3}/2$	0.0
$\vec{a}_2$	a	0.0	0.0
Mo/W	0.0	-1.82	3.07
S	0.0	0.0	1.50
S	0.0	0.0	4.64

Table 2.1: Definition of directional vectors for an hexagonal lattice and atomic positions for a monolayer MoS<sub>2</sub> or WS<sub>2</sub> unit cell

WS<sub>2</sub> will only be studied in its 2H structure as the 3R structure is unstable and far less common [36]. The only difference with MoS<sub>2</sub>, apart from the fact that the molybdenum atoms are replaced by tungsten atoms, is in the distances between the atoms. In this case, we find the following distances [28]:

S-S or W-W first neighbors	a = 3.153 Å
W-S first neighbors	b = 2.408 Å
between W plane and S plane	z = 1.571 Å
between S planes of different nearest layers	w = 2.990 Å
between W planes of different layers	c' = 6.162 Å
2H unit cell height	c = 12.32 Å

The path taken in the reciprocal space to draw the band structures of planar structures is the  $\Gamma$ MK $\Gamma$  path as defined in figure 2.2. For three-dimensional crystals, dispersion relations have also been drawn in a direction perpendicular to the  $\Gamma$ MK $\Gamma$  path, called  $\Delta$  and visible on the figure as the straight line passing from  $\Gamma$  to A.

## 2.2.2 Electronic properties

Single-layer transition metal dichalcogenides (TMDs) are semiconductors with a direct bandgap at the K point of the Brillouin zone. The main orbital contribution characterizing the top of the valence band is a combination of the  $d_{x^2-y^2}$  and  $d_{xy}$  orbitals of metal M (in our case molybdenum or tungsten), hybridize with the  $p_x$  and  $p_y$  orbitals of chalcogen X (in our case sulfur). The bottom of the conduction band is mainly formed by the  $d_{3z^2-r^2}$  orbital of M

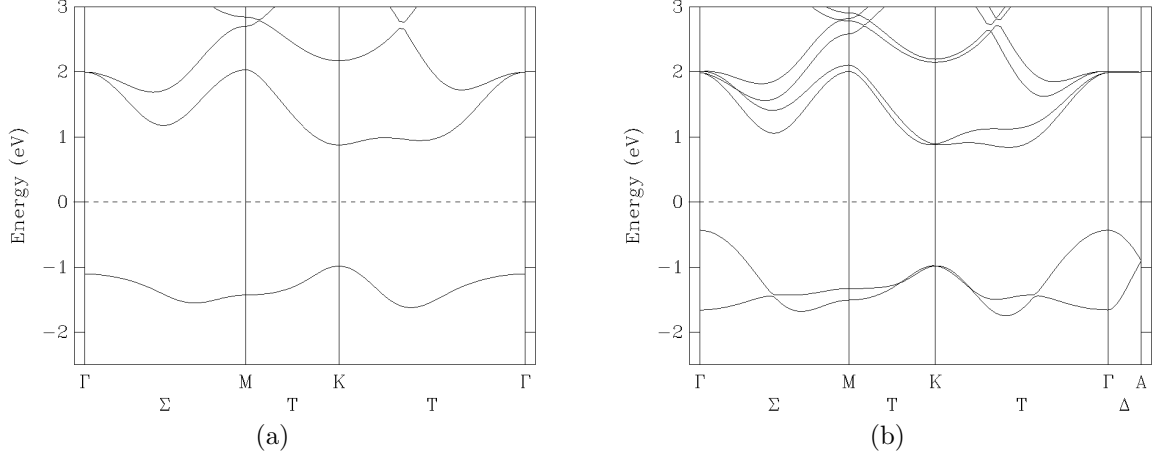


Figure 2.4: TB band structures for MoS<sub>2</sub> 2H (a) monolayer and (b) bulk.

and a smaller contribution from the  $p_x$  and  $p_y$  orbitals of X. In the case of MoS<sub>2</sub>, the orbitals involved are the  $d_{xy}$ ,  $d_{yz}$ ,  $d_{zx}$ ,  $d_{x^2-y^2}$ ,  $d_{3z^2-r^2}$  orbitals for Mo- $4d^5$  and the  $p_x$ ,  $p_y$ ,  $p_z$  orbitals for S- $3p^4$  which sum up to the 93% of the total weight of the four conduction bands and seven valence bands [27].

Band structures of monolayer MoS<sub>2</sub> are very sensitive to external mechanical stress (and to the type of stress applied), much more so than graphene. The TB band structure for monolayer MoS<sub>2</sub> 2H is shown in figure 2.4a for illustration. Mechanical stress will shift the bandgap from direct to indirect [19,37], and can even confer metallic properties on the monolayer, predicted for a tensile strain of about 8% or a compressive strain of about 15% [38].

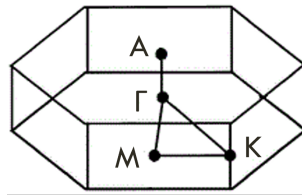


Figure 2.5: First Brillouin zone used for layered MoS<sub>2</sub> and WS<sub>2</sub>. [27]

In the case of multilayers, TMDs are indirect bandgap semiconductors. The TB band structure for bulk MoS<sub>2</sub> 2H is shown in figure 2.4b for illustration. The top of the valence band is located at the  $\Gamma$  point and is formed mainly by the  $d_{3z^2-r^2}$  orbitals of the M atom and  $p_z$  orbitals of the X atoms. The bottom of the conduction band is located at the Q point in the Brillouin zone visible on figure 2.5. This Q point lies between the  $\Gamma$  point and the K point, but its exact position varies according to the number of layers. The orbitals mainly contributing at the Q point are the  $d_{xy}$ ,  $d_{x^2-y^2}$  and  $d_{3z^2-r^2}$  orbitals of metal M and the  $p_x$ ,

$p_y$  and  $p_z$  orbitals of chalcogen X.

The rich orbital structure of the valence and conduction bands of TMDs complicates the development of a tight-binding model valid throughout the Brillouin zone. Moreover, we must also take into account the strong spin-orbit coupling present in TMDs, which creates a large separation between the last occupied valence bands and the first unoccupied conduction bands at the K point and at the minimum of the Q point. This separation is greater for TMDs containing tungsten than for those containing molybdenum, as the W is heavier. In our work, this coupling is not taken into account.

### 2.2.3 Optical properties

The absorption spectrum of bulk MoS<sub>2</sub> shows two distinct low-energy peaks at 1.88 eV (related to the exciton called A) and 2.03 eV (related to the exciton called B) [39] which have been attributed to direct transitions between the conduction band and a spin-orbit splitting of the valence band at the K point. The MoS<sub>2</sub> monolayer shows two exciton peaks at around 1.9 eV and 2.1 eV [40]. These values are really close to those of the bulk which is consistent with the observation that MoS<sub>2</sub> has a slight red-shift in its exciton peaks as the layer thickness increases.

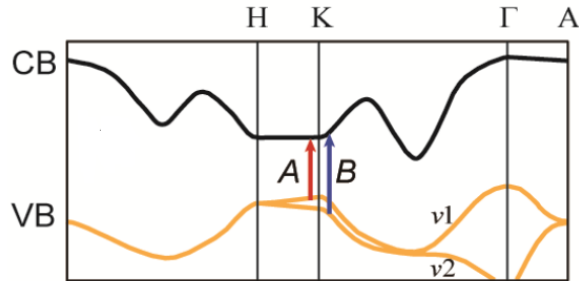


Figure 2.6: Simplified band structure of MoS<sub>2</sub> in bulk. The black band is the lowest conduction band and the two orange bands are the highest valence bands. The two arrows represent direct exciton transitions, A for the red arrow and B for the blue arrow. [41]

The high luminescence of MoS<sub>2</sub> monolayers can be explained by the fact that the high binding energy of exciton A reduces the probability of excited electrons falling into the conduction band before recombination [39]. Indeed, theoretical predictions attribute to MoS<sub>2</sub> monolayers binding energy between 526 meV [42] and 1 eV [43,44]. Experimental data are lower, but still high (220 meV, obtained by STM [45], or 440 meV, obtained by PL spectroscopy [46], sometimes even 570 meV [40]). The value of this binding energy is important for applications. For example, to use MoS<sub>2</sub> as a photodetector or in solar

cells, we need to dissociate excitons (and therefore have a low binding energy) to create a current. On the other hand, a high binding energy value would make it a useful material for applications involving trions (quasiparticles composed of two electrons and one hole), exciton-polariton creation and, more practically, in the field of polariton lasers [44]. The direct bandgap nature of monolayer MoS<sub>2</sub> enhances the likelihood of radiative emission. The optical bandgap, measured by PL spectroscopy, is the exciton energy which determines the onset of vertical interband transitions. The exciton binding energy is the difference between the electronic bandgap value and the optical bandgap.

### 2.2.4 Magnetism and spintronic

In its pristine form, MoS<sub>2</sub> is considered a diamagnetic semiconductor, implying that it lacks a spontaneous magnetic moment. However, its magnetic behavior can be altered significantly by introducing defects, edges, or dopants, resulting in various magnetic phenomena [47,48,49]. Edge states contribute to the emergence of edge magnetism, a phenomenon that has attracted particular interest due to its potential implications for nanoscale magnetic devices and spin-based electronics [50,51,52,53]. Furthermore, through controlled doping or the incorporation of transition metal impurities within the MoS<sub>2</sub> lattice, the material can exhibit modified magnetic behavior [48,54,55]. The introduction of these impurities results in the localization of magnetic moments, leading to the manifestation of ferromagnetic or antiferromagnetic characteristics depending on the specific atomic configuration and distribution [54,56]. Such tunable magnetic properties offer promising opportunities for the development of next-generation spintronic devices, magnetic sensors, and data storage applications. For example, MoS<sub>2</sub> and other TMDs have been studied for their applications as nonlocal spin valves, magnetic tunnel junctions (MTJs, a device that could be used to store a bit information in a nanomagnet), tunnel barriers or spin transistors for example [57].

Following these observations, it seemed appropriate to focus our research on controlled nanoribbon structures as it allowed to study quite easily the influence of different species of edges. Furthermore, these kind of structures could be useful to study the influence of defects or potential manipulations on the edges showing ferromagnetic or antiferromagnetic behavior.

## 2.3 Nanoribbons of TMDs

### 2.3.1 Structure

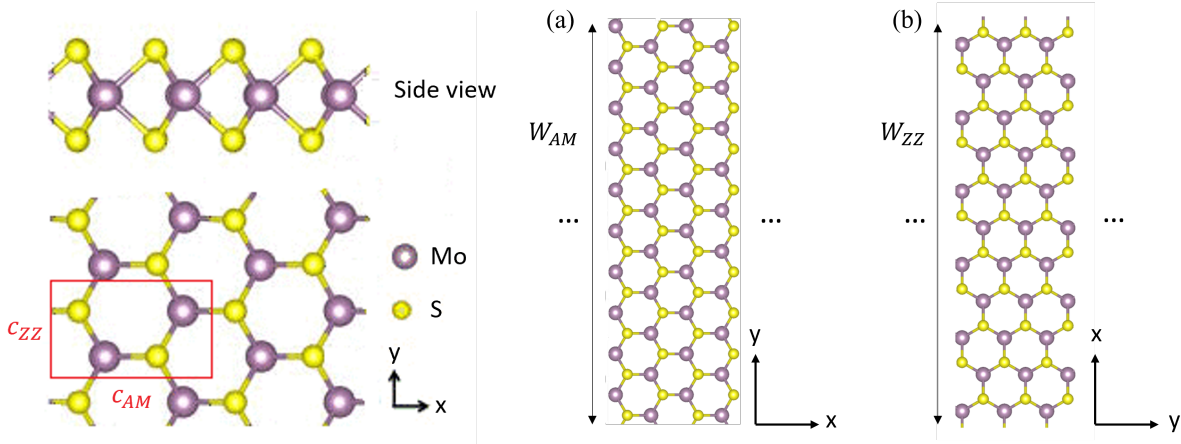


Figure 2.7: Unit cell for a MoS<sub>2</sub> nanoribbon and example of (a) an armchair MoS<sub>2</sub> nanoribbon, (b) a zigzag MoS<sub>2</sub> nanoribbon.

To define nanoribbons, the unit cell used is radically different than for layers. We first define a rectangle as seen in figure 2.7 where  $c_{ZZ} = 3.16 \text{ \AA}$  and  $c_{AM} = 5.46 \text{ \AA}$  are respectively the width and length of the rectangular cell. There are two main types of nanoribbon, distinguished by the shape of the edges : zigzag and armchair. The unit cell of a zigzag nanoribbon is generated by duplicating the rectangular cell a specific number of times horizontally along the x-direction to achieve the desired nanoribbon width. Conversely, for an armchair nanoribbon, the rectangular cell is duplicated a certain number of times vertically along the y-direction to attain the desired width of the nanoribbon and to create the unit cell. Hence, the width of a zigzag ribbon is defined by  $W_{ZZ} = nc_{AM}$  and the width of an armchair ribbon by  $W_{AM} = nc_{ZZ}$ , where  $n$  is an integer or semi-integer. In the case where  $n$  is an integer, we find what we call an asymmetrical nanoribbon (see figure 2.8 (a), (d), (f) and (h)) as the two edges are made of different atoms (one will be a sulfur edge while the other will be a molybdenum edge). In the case of a semi-integer  $n$ , the ribbon is symmetrical (see figure 2.8 (b), (c) and (g)), which will generally make it more stable [50]. A nanoribbon is classified as symmetrical or asymmetrical based on its overall structure here, irrespective of the endings.

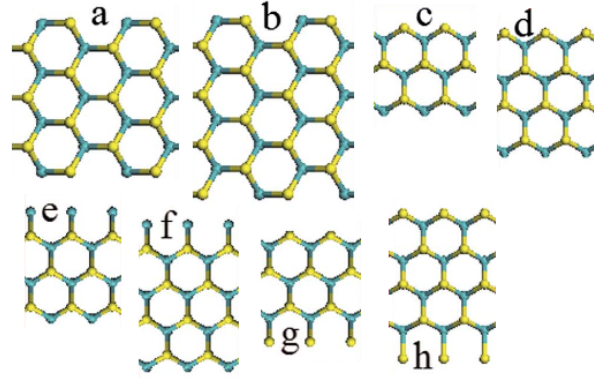


Figure 2.8: The different types of  $\text{MoS}_2$  nanoribbons (the width of the ribbon is vertical in the diagram): (a) asymmetrical armchair nanoribbon, (b) symmetrical armchair nanoribbon, (c) symmetrical zigzag nanoribbon, (d) asymmetrical zigzag nanoribbon, (e) symmetrical zigzag nanoribbon with molybdenum endings, (f) asymmetrical zigzag nanoribbon with molybdenum endings, (g) symmetrical zigzag nanoribbon with sulfur endings, (h) asymmetrical zigzag nanoribbon with sulfur endings. [50]

Numerous studies have demonstrated that  $\text{MoS}_2$  nanoribbons are more stable when passivated with sulfur on the Mo edge [58,59]. In the case of armchair nanoribbons, even greater stability can be achieved with hydrogen terminations [50]. These stability findings are verified whether or not spin polarization is taken into account in the calculations.

Experimental observation using scanning tunneling microscopy (STM) (figure 2.9) of the growth of triangular structure facilitated the discovery of the aforementioned conclusions.

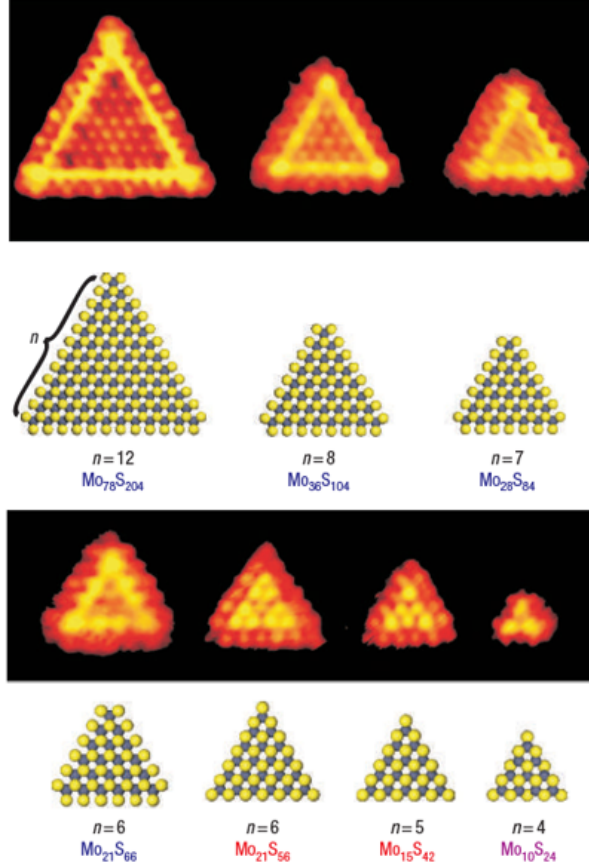


Figure 2.9: STM images and corresponding models of seven triangular  $\text{MoS}_2$  nanoclusters ranging in size from 4 to 12 Mo atoms at the edges. Mo atoms are shown in grey and S atoms in yellow. [58]

STM images of these triangular  $\text{MoS}_2$  nanocrystals show a brighter edge on the line of atoms preceding the edge (for an edge with more than 6 atoms). This is due to the electronic structure of  $\text{MoS}_2$ , which is strongly modified at the edges. DFT calculations indicate that this is due to fully sulfur-dimer passivated Mo edges, presenting two edge states making them metallic [58,60]. In the case of smaller, triangular nanocrystals, S edges are preferred. We could therefore extrapolate that Mo edges passivated by sulfur dimers are the most stable. This conclusion seems correct irrespective of the substrate on which the structure was created as long as there is no strong interaction between the substrate and the nanoclusters [50,60]. Other configurations (such as hydrogen passivation) are theoretically stable. In reality, however, the nanoribbons observed are zigzag nanoribbons passivated with sulfur dimers, even when the growth environment is modified [60], thus characterizing a more stable structure. When hydrogen is abundant, it has a tendency to attach itself to the edges. In this scenario, the most stable configuration is a zigzag nanoribbon with sulfur dimer passivation, accompanied by hydrogen fixation along the edges [59]. Nevertheless, comparing

this new structure with the previous zigzag passivated nanoribbon with the clean S dimer configuration show that the number of metallic bands remains constant and the influence of hydrogen is simply to induce a small shift in energy of the two metallic bands at the Mo edge.

In the following, we decided to focus on a zigzag nanoribbon (for its metallic property, not found in an armchair nanoribbon) passivated with sulfur dimers (i.e. a ribbon similar to the one shown in figure 2.8 (g) or (h)) in order to study a stable, experimentally feasible structure. According to DFT, atomic distances are the same as for the planar MoS<sub>2</sub> except for the sulfur dimers, which are placed slightly further apart and separated in z by 1.9 Å (instead of 3.13 Å for the sulfur atoms present in the nanoribbon and in the planar structures) and for the atoms close to the edges. These modifications were made following data obtained by Péter Vancsó after relaxation of the structure by DFT [61].

In the case of nanoribbons, band structures are drawn following the path  $\Gamma X$  where  $X = \frac{\pi}{c_{ZZ}}$  in the case of zigzag ribbon creation or  $\frac{\pi}{c_{AM}}$  in the case of armchair ribbon. Directional vectors are now perpendicular, thanks to the use of a rectangular mesh in direct space.

### 2.3.2 Properties

One-dimensional nanostructures such as nanotubes, nanosticks, nanowires and nanoribbons have been actively studied for two decades now, thanks to their special electronic and physical properties associated with their small size. Nanoribbons have been predicted to display high electrical and thermal conductivity and high breakdown current density which triggered the interest of scientists [62]. The stability of MoS<sub>2</sub> nanoribbons, combined with the intrinsic properties of the material itself (which is resistant to oxidation<sup>1</sup> and is a good catalyst), suggests possible applications in a wide range of fields, including nanoelectronics, nanotribology (the science that studies the phenomena that can occur between two material systems in contact driven by relative motion, such as wear, friction, etc.) and catalysis. Very quickly, scientists wanted to develop theories to explain the origins of these observed electrical, optical, mechanical and magnetic properties, and to guide the development of new devices incorporating these nanostructures.

A typical example of such nanostructures is the graphene nanoribbon. It has been shown by calculations that graphene nanoribbons with a hydrogen edge in the armchair configuration are metallic if the width parameter is equal to  $3n-1$  (where  $n$  is an integer)

---

<sup>1</sup>To a certain extent, as it is a material that still oxidize within a few months. Oxidation can be avoided to a certain extent by encapsulating the layer or nanoribbon for example with a polymer layer [63,64].

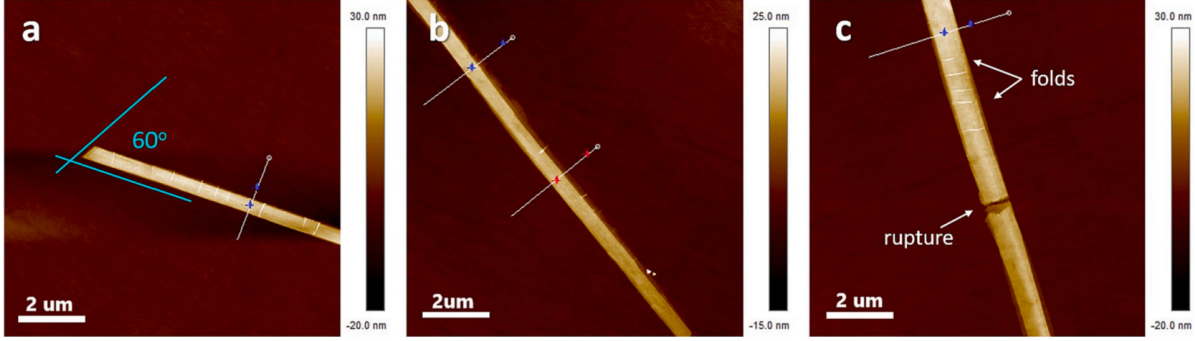


Figure 2.10: AFM images of MoS<sub>2</sub> nanoribbons produced by CVD [78]

and are otherwise semiconducting [50,65,66]. On the other hand, graphene nanoribbons in zigzag configuration have been predicted metallic and independent of their width parameter. Further studies have shown that, in reality, both types of nanoribbon exhibit a bandgap, and that increasing the ribbon width decreases the energy of this bandgap [67]. The half-metallicity under a high transverse electric field of graphene nanoribbons has opened up new opportunities in the field of spintronics [68,69]. By using TB parameters and local Coulomb interaction (the so-called Hubbard U) the magnetic properties of graphene nanoribbons have been studied in large scale systems. It was found that the magnetism of the edge states is robust against disorder and potential fluctuations [70,71,72,73].

These discoveries also led scientists to investigate the electronic and magnetic properties of MoS<sub>2</sub> nanoribbons. For example, MoS<sub>2</sub> armchair nanoribbons have a non-magnetic ground state (with or without hydrogen saturation), whereas MoS<sub>2</sub> zigzag nanoribbons have a ferromagnetic ground state, regardless of edge configuration (the reasoning behind the justification of the ferromagnetic character differs, but the conclusion remains the same) [74,75,76]. It is also possible to stabilize the magnetic states of MoS<sub>2</sub> zigzag nanoribbons by applying mechanical stress to the structure. This has the effect of increasing the energy difference between the magnetic and non-magnetic states [39]. In addition, magnetic measurements on large scale epitaxial growth of zigzag MoS<sub>2</sub> nanoribbons show prominent ferromagnetic behavior [77]. The ferromagnetic nature of zigzag MoS<sub>2</sub> nanoribbons makes them more interesting for spintronics applications than fully ferromagnetic graphene nanoribbons, as the latter can only be obtained by applying an external electromagnetic field.

MoS<sub>2</sub> nanoribbons can be obtained experimentally from several technique. The choice of method depends on factors like scalability, purity, control over dimensions, and the specific application requirements. Researchers often choose a combination of the following techniques to achieve the desired properties in MoS<sub>2</sub> nanoribbons.

- Chemical Vapor Deposition (CVD) is a widely used method consisting on growing MoS<sub>2</sub>

nanoribbons on substrate by introducing molybdenum precursor and sulfur precursor in a reaction chamber where they react and deposit on a substrate in a controlled manner. By choosing the growth conditions (temperature, pressure, concentration etc) influences the dimensions and properties of nanoribbons. In usual CVD conditions, the Mo edge of the nanoribbon is passivated by sulfur dimers, but it is difficult to have clean and long edges. Using additional chemical etching gives better results [79,78].

- Lithography and etching techniques are another technique allowing to produce MoS<sub>2</sub> nanoribbons by using an electron beam lithography or photolithography for example to pattern MoS<sub>2</sub> films followed by an etching process to remove the unwanted material. Some really cleaned long zigzag edge nanoribbons have been produced by laser-induced unzipping of nanotubes or by milling with a focus ion beam [80].
- MoS<sub>2</sub> nanoribbons can also be produced by liquid phase exfoliation of bulk MoS<sub>2</sub>. The latest is dispersed in a solvent and nanoribbons are obtained by inducing exfoliation by sonication or other mechanical means.
- Hydrothermal or solvothermal synthesis is also used by dissolving precursors in a solvent. The reaction takes place under elevated temperature and pressure, leading to the formation of nanoribbons.
- By using a template, such as porous membrane or nanotubes, it is possible to grow MoS<sub>2</sub> nanoribbons using these guides. The template is coated with MoS<sub>2</sub> precursors and then removed after the growing process, leaving nanoribbons.
- Top-Down Mechanical Exfoliation is, as its name suggest, a mechanical exfoliation method used to obtain MoS<sub>2</sub> nanoribbons from bulk crystals. This is one of the oldest method, as it is also with this method than graphene nanoribbons have been isolated for the first time. By mechanically cleaving a bulk crystal, it is possible to produce thin layers and further processing is done to obtain nanoribbons.

Due to the recent experimental results [81,82,83], theoretical understanding of the edge magnetism in MoS<sub>2</sub> nanoribbons is important, especially in larger, realistic systems including disorder.

The energy difference between spin-polarized and non-spin-polarized states, as well as the total magnetic moment, increases with increasing ribbon length. The MoS<sub>2</sub> zigzag nanoribbons all appear to be metallic, irrespective of their width, whereas the MoS<sub>2</sub> armchair nanoribbons are semiconducting. For example, the 10-atom-wide MoS<sub>2</sub> armchair nanoribbon

has a direct bandgap of 0.52 eV [51]. The width of the bandgap depends little on the width of the nanoribbon, and converges rapidly to the value of 0.56 eV (particularly from a width of around 15 atoms). This value is significantly smaller than that of monolayer MoS<sub>2</sub> (which was 1.69 eV), as the atoms at the edges of the nanoribbons induce new flat energy levels above the valence band and below the conduction band, which reduce the size of the band gap. In general, zigzag MoS<sub>2</sub> nanoribbons are more stable than armchairs, and both are more stable than experimentally created MoS<sub>2</sub> nanoclusters.

DFT-based calculations can predict these properties very accurately and provide guidance for the creation of updated technology, and have indeed been widely used, but they can be quite time-consuming and cumbersome. In order to study systems involving a large number of atoms, the tight-binding (TB) approach is a more suitable alternative, which can also provide a simple starting point for the further inclusion of many-body electron-electron effects.

# Chapter 3

## Computational methods

Throughout this study, we consistently compare our tight-binding findings against density functional theory (DFT) results. Indeed, since we are using a Slater-Koster approach of tight-binding, hopping terms and on-site energies are parameters that have to be set by comparison with another method. Similarly, this applies to the determination of interaction terms within the Hubbard model, which serves to study the magnetic properties of nanoribbons. This chapter is dedicated to detail the computational methods employed in our investigation.

### 3.1 Density Functional Theory

To correctly set the tight-binding parameters and crystal structures as well as ensure correct orbital dependency, we compared the band structures obtained by tight-binding with the ones derived from density functional theory (DFT) calculations.

DFT is a quantum mechanical framework widely employed in condensed matter physics and quantum chemistry. By using functionals of the spatially dependent electron density, it allows to study the properties of a many-electron system from first-principles. Built upon the Hohenberg-Kohn theorems, DFT asserts that the electron density is the crucial determinant for the external potential throughout a system. It introduces a universal functional of the electron density, such that minimizing the energy provides the ground-state energy of the system. The practical implementation involves the Kohn-Sham equations, treating electrons as if they were independent and submitted to an effective potential. This potential includes the unknown exchange-correlation functional, which captures the intricate interactions between electrons that are difficult to model. Since, instead of the many-body wave function, the one-body density is used as the fundamental variable, DFT has to tackle a function of

only three spatial coordinates rather than the 3N coordinates of the wave function. Computational costs are then relatively low when compared to wavefunction quantum chemistry methods, such as exchange only Hartree–Fock theory and its descendants that include many-body electron correlation but it is still a computational costly method to study big structures [84]. A more detailed presentation of DFT can be found in Ref. [85,86,87,88].

The DFT calculations presented in this work have been performed by Péter Vancsó. They are computed in the Vienna ab initio simulation package (VASP) [89] using the projector augmented wave (PAW) method [90]. The exchange-correlation functional chosen is the Perdew-Burke-Ernzerhof generalized gradient approximation (GGA-PBE) [91]. Band structure calculations utilize a plane wave cutoff set at 500 eV and the Brillouin zone is sampled on a  $(12 \times 2 \times 1)$  Monkhorst-Pack mesh of  $k$  points [92]. The convergence criterion for forces is set to 0.01 eV/Å during geometry optimization.

## 3.2 Tight-binding theory

The computational framework used for the calculation of MoS<sub>2</sub> band structures, additionally to DFT, is based upon the utilisation of the tight-binding (TB) formalism. This method is similar to the LCAO (linear combination of atomic orbitals) frequently used in quantum chemistry.

In essence, the tight-binding model is the opposite of the "almost free" electron approach as electrons are considered tightly bound (as the name suggests) to the atom to which they belong. The main assumption of this model is that the orbitals  $u_{k\lambda}(\vec{r} - \vec{R}_k)$  are rapidly decreasing function of the distance  $|\vec{r} - \vec{R}_k|$  (where  $k$  is the index of an atomic site positioned at  $\vec{R}_k$  and  $\lambda$  designates the orbital). As a result, orbitals at different atomic sites show minimal or null spatial overlap.

The Schrödinger's equation has to be solved :

$$H\psi(\vec{r}) = E\psi(\vec{r}), \quad (3.1)$$

where the Hamiltonian is one of an electron in an independent electron approach and is written as

$$H = \frac{p^2}{2m} + V(\vec{r}),$$

where  $V(\vec{r})$  include the ionic potentials and the self-consistent electrostatic interaction due to the other valence electrons. It is assumed that the potential  $V(\vec{r})$  can be written as the

sum on localized atomic potential

$$V(\vec{r}) = \sum_k \phi_k(\vec{r} - \vec{R}_k). \quad (3.2)$$

The wave function is developed using LCAO

$$\psi(\vec{r}) = \sum_{j,\mu} c_{j\mu} u_{j\mu}(\vec{r} - \vec{R}_j),$$

where  $u_{j\mu}$  are angular dependant and are the wave functions solution of the atomic Schrödinger equation

$$\left[ \frac{p^2}{2m} + \phi_j(\vec{r} - \vec{R}_j) \right] u_{j\mu}(\vec{r} - \vec{R}_j) = \epsilon_{j\mu} u_{j\mu}(\vec{r} - \vec{R}_j). \quad (3.3)$$

The eigenenergies  $\epsilon_i^{\lambda\mu}$  are named on-site energy and  $\mu$  stands for quantum numbers of the atomic wavefunctions  $\{n,l,m\}$  when  $\phi_j$  is a potential of spherical symmetry. Thanks to the assumption that the orbitals of different atomic sites do not overlap, we can write an orthogonality rule

$$\int u_{i\lambda}^*(\vec{r} - \vec{R}_i) u_{j\mu}(\vec{r} - \vec{R}_j) d^3r = \delta_{ij} \delta_{\lambda\mu}.$$

Following these developments, we can project the initial Schrödinger equation onto the  $u_{i\lambda}$  orbital

$$\sum_{j\mu} \int u_{i\lambda}^*(\vec{r} - \vec{R}_i) \left[ \frac{p^2}{2m} + V(\vec{r}) \right] u_{j\mu}(\vec{r} - \vec{R}_j) d^3r c_{j\mu} = E \sum_{j\mu} c_{j\mu} \delta_{ij} \delta_{\lambda\mu}.$$

The Kronecker deltas in the right hand side result from the orthogonality relation. Using the expression of  $V(\vec{r})$  from (3.2) and separating the cases  $k = j$  and  $k \neq j$ , we obtain

$$\epsilon_{i\lambda} c_{i\lambda} + \sum_{j\mu} \int u_{i\lambda}^*(\vec{r} - \vec{R}_i) \sum_{k \neq j} \phi_k(\vec{r} - \vec{R}_k) u_{j\mu}(\vec{r} - \vec{R}_j) d^3r c_{j\mu} = E c_{i\lambda},$$

which can be rewritten by separating the case  $j = i$  from the case  $j \neq i$  as

$$\epsilon_{i\lambda} c_{i\lambda} + \sum_{\mu} \alpha_i^{\lambda\mu} c_{i\mu} + \sum_{j \neq i} \sum_{\mu} \beta_{ij}^{\lambda\mu} c_{j\mu} = E c_{i\lambda},$$

where

$$\begin{aligned}
\alpha_i^{\lambda\mu} &= \int u_{i\lambda}^*(\vec{r} - \vec{R}_i) \sum_{k \neq i} \phi_k(\vec{r} - \vec{R}_k) u_{i\mu}(\vec{r} - \vec{R}_i) d^3r \\
&= \int u_{i\lambda}^*(\vec{r}) \sum_{k \neq i} \phi_k[\vec{r} - (\vec{R}_k - \vec{R}_i)] u_{i\mu}(\vec{r}) d^3r \\
\beta_{ij}^{\lambda\mu} &= \int u_{i\lambda}^*(\vec{r} - \vec{R}_i) \sum_{k \neq j} \phi_k(\vec{r} - \vec{R}_k) u_{j\mu}(\vec{r} - \vec{R}_j) d^3r, \quad j \neq i
\end{aligned} \tag{3.4}$$

$\alpha_i^{\lambda\mu}$  is called the crystal field integral and  $\beta_{ij}^{\lambda\mu}$  the hopping integral. It is generally assumed that three-center integrals like those which occur for  $k \neq i$  and  $k \neq j$  for the  $\beta_{ij}^{\lambda\mu}$  equation are small with respect to the two-center integral corresponding to  $k = i \neq j$ .  $\beta_{ij}^{\lambda\mu}$  is then written as

$$\begin{aligned}
\beta_{ij}^{\lambda\mu} &= \int u_{i\lambda}^*(\vec{r} - \vec{R}_i) \phi_i(\vec{r} - \vec{R}_i) u_{j\mu}(\vec{r} - \vec{R}_j) d^3r \\
&= \int u_{i\lambda}^*(\vec{r}) \phi_i(\vec{r}) u_{j\mu}[\vec{r} - (\vec{R}_k - \vec{R}_i)] d^3r, \quad j \neq i.
\end{aligned} \tag{3.5}$$

The energies solution of the Schrödinger equation (3.1) are then the eigenvalues of the matrix whose elements are

$$H_{i\lambda,j\mu} = (\epsilon_{i\lambda}\delta_{\lambda\mu} + \alpha_i^{\lambda\mu})\delta_{ij} + \beta_{ij}^{\lambda\mu}.$$

Due to the unknown nature of the orbitals, the tight-binding parameters are also unknown. This study is based on the Slater and Koster approach, treating the tight-binding model parameters as adjustable variables to achieve accurate band structures. This method is applicable in cases where Bloch's theorem is not valid, as DFT, and computationally efficient.

We can go a step further by looking at the atomic potential  $\phi_k$ . This potential is made up of two parts: the ionic potential (denoted  $\phi_k^0$ ) and electron-electron interactions. Intra-atomic electron Coulombic repulsions are assumed to be the main contributor to Coulombic electron-electron interactions (consistent with the assumption that orbitals from different atomic sites have limited overlap). Thanks to this assumption, the  $u_{k\lambda}$  orbitals can be calculated using the Hartree-Fock approximation where the electron exchange is accounted for

$$\begin{aligned}
\left[ \frac{p^2}{2m} + \phi_k^0(\vec{r}) \right] \psi_{k\lambda\sigma}(\xi) + \sum_{\mu,\sigma'} n_{k\mu\sigma'} \int u_{k\mu}^*(\vec{r}') u_{k\mu}(\vec{r}') \frac{e^2}{|\vec{r} - \vec{r}'|} d^3r' \psi_{k\lambda\sigma}(\xi) \\
- \sum_{\mu} n_{k\mu\sigma} \int u_{k\mu}^*(\vec{r}') u_{k\lambda}(\vec{r}') \frac{e^2}{|\vec{r} - \vec{r}'|} d^3r' \psi_{k\mu\sigma}(\xi) = \epsilon_{k\lambda} \psi_{k\lambda\sigma}(\xi), \tag{3.6}
\end{aligned}$$

where  $\sigma$  is the spin projection quantum number,  $\xi$  is for  $\{\vec{r}, s\}$  where  $s = \pm 1/2$  is the spin projection variable,  $n_{k\mu\sigma}$  is the average value of the spin-orbit occupancy number and  $\psi_{k\lambda\sigma}(\xi)$  is a spin-orbital defined by

$$\psi_{k\lambda\sigma}(\xi) = u_{k\lambda}(\vec{r})\delta_{\sigma s}.$$

We have set  $\frac{1}{4\pi\epsilon_0} = 1$  to simplify the expression. Assuming a paramagnetic state (i.e.  $n_{k\mu\sigma} = n_{k\mu-\sigma}$ ), the equation (3.6) can be rewritten as follows

$$\begin{aligned} & \left[ \frac{p^2}{2m} + \phi_k^0(\vec{r}) \right] u_{k\lambda}(\vec{r}) + \sum_{\mu} n_{k\mu\sigma} \left[ 2 \int u_{k\mu}^*(\vec{r}') u_{k\mu}(\vec{r}') \frac{e^2}{|\vec{r} - \vec{r}'|} d^3r' u_{k\lambda}(\vec{r}) \right. \\ & \quad \left. - \int u_{k\mu}^*(\vec{r}') u_{k\lambda}(\vec{r}') \frac{e^2}{|\vec{r} - \vec{r}'|} d^3r' u_{k\mu}(\vec{r}) \right] = \epsilon_{k\lambda} u_{k\lambda}(\vec{r}). \end{aligned} \quad (3.7)$$

We assume  $u_{k\lambda}^0(\vec{r})$  as the solution of the Schrödinger equation with the electron correlation neglected

$$\left[ \frac{p^2}{2m} + \phi_k^0(\vec{r}) \right] u_{k\lambda}^0(\vec{r}) = \epsilon_{k\lambda}^0 u_{k\lambda}^0(\vec{r}).$$

We can then use a first-order perturbation for the Coulomb and exchange terms to rewrite (3.7) as

$$\begin{aligned} \epsilon_{k\lambda} = \epsilon_{k\lambda}^0 + \sum_{\mu} & \left[ 2 \int \int |u_{k\mu}^0(\vec{r}')|^2 \frac{e^2}{|\vec{r} - \vec{r}'|} |u_{k\lambda}^0(\vec{r})|^2 d^3r' d^3r \right. \\ & \left. - \int \int u_{k\mu}^{0*}(\vec{r}') u_{k\lambda}^0(\vec{r}') \frac{e^2}{|\vec{r} - \vec{r}'|} u_{k\mu}^{0*}(\vec{r}) u_{k\mu}^0(\vec{r}) d^3r' d^3r \right] n_{k\mu\sigma}. \end{aligned} \quad (3.8)$$

Subsequent to this, a sequence of simplifications can be implemented. In the case of transition metals, we restrict the orbitals to the 3d, 4d and 5d orbitals. It is also assumed that the intra-atomic coulombic interaction and exchange integrals are independent of the indices  $\lambda$  and  $\mu$  (which specify a particular d-orbital). Finally, we assume that the occupancy number  $n_{k\mu\sigma}$  does not vary between different spin-orbitals. We can then simplify (3.8) by

$$\epsilon_{k\lambda} = \epsilon_{k\lambda}^0 + (9 U_k - 4 J_k) \frac{N_k}{10} = \epsilon_{k\lambda}^0 + U_k^{eff} N_k.$$

$U_k$  is the average of the coulombic interactions and  $J_k$  is the average of the exchange interactions at atomic site  $k$ .  $N_k$  is the total number of occupancies of the 10 spin-orbitals of site  $k$  ( $N_k = \sum_{\mu,\sigma} n_{k\mu\sigma}$ ). This form of the Hamiltonian, known as "Hubbard-Tight-binding", is important for magnetic ribbons only. In order to further develop the integrals, we choose an

expression for the five d orbitals located at atomic site  $i$

$$u_{i\lambda}(\vec{r}) = f_i(r)Y_\lambda^d(\theta, \phi),$$

where  $f_i(r)$  is a radial function and  $Y_\lambda^d(\theta, \phi)$  denotes a real spherical harmonics corresponding to  $l = 2$ . The real spherical harmonics are linear combination of the usual spherical harmonics  $Y_{lm}(\theta, \phi)$  (see Appendix A for more details). Here,  $\lambda$  ranges from 1 to 5, the  $Y_\lambda^d$  representing the angular variation of functions behaving respectively as  $xy$ ,  $yz$ ,  $zx$ ,  $x^2 - y^2$  and  $3z^2 - r^2$ . For convenience, the origin of the coordinates has been shifted on the site  $i$ . We can rewrite the  $\alpha_i^{\lambda\mu}$  of (3.4) as the sum over  $k$  of integrals

$$\begin{aligned} A_{ik}^{\lambda\mu} &= \int u_{i\lambda}^*(\vec{r}) u_{i\mu}(\vec{r}) \phi_k(\vec{r} - \vec{R}_k) d^3r \\ &= \int |f_i(r)|^2 \phi_k(|\vec{r} - \vec{R}_k|) Y_\lambda^d(\theta, \phi) Y_\mu^d(\theta, \phi) d^3r, \end{aligned}$$

where  $\vec{R}_k$  is the vector stretching from the atomic site  $i$  to the atomic site  $k$ . The transition from one equality to the other is possible by considering  $\phi_k$  as a spherical potential. We then rotate the coordinate axes from Oxyz to OXYZ, in which OZ is aligned with the vector  $\vec{R}$ . Defining  $\Theta$  and  $\Phi$  as the polar angles formed by the vector  $\vec{r}$  with the new coordinate system, we can write

$$Y_\lambda^l(\theta, \phi) = \sum_{m=-l}^{+l} Q_{\lambda m}^l Y_{lm}(\Theta, \Phi).$$

In this equation,  $Y_{lm}(\Theta, \Phi)$  are the usual spherical harmonics with respect to the axes OXYZ and  $Q_{\lambda m}^l$  is a matrix  $(2l+1) \times (2l+1)$  that depends on the direction cosine of  $\vec{R}$  (see Appendix A for the expressions of  $Q_{\lambda m}^l$ ). Thanks to these developments, we can rewrite  $A_{ik}^{\lambda\mu}$  for the d orbitals as

$$A_{ik}^{\lambda\mu} = Q_{\lambda 0}^d Q_{\mu 0}^d (dd\sigma)' - (Q_{\lambda 1}^d Q_{\mu, -1}^d + Q_{\lambda, -1}^d Q_{\mu 1}^d) (dd\pi)' + (Q_{\lambda 2}^d Q_{\mu, -2}^d + Q_{\lambda, -2}^d Q_{\mu 2}^d) (dd\delta)',$$

where

$$\begin{aligned} (dd\sigma)' &= \frac{2l+1}{2} \int_0^\infty dr r^2 |f_i(r)|^2 \int_{-1}^{+1} dU \phi_k(\sqrt{r^2 - 2rR \cos \Theta + R^2}) [P_l^0(\cos \Theta)]^2 \\ (dd\pi)' &= -\frac{2l+1}{2} \frac{(l-1)!}{(l+1)!} \times \int_0^\infty dr r^2 |f_i(r)|^2 \int_{-1}^{+1} dU \phi_k(\sqrt{r^2 - 2rR \cos \Theta + R^2}) [P_l^1(\cos \Theta)]^2 \\ (dd\delta)' &= \frac{2l+1}{2} \frac{(l-2)!}{(l+2)!} \times \int_0^\infty dr r^2 |f_i(r)|^2 \int_{-1}^{+1} dU \phi_k(\sqrt{r^2 - 2rR \cos \Theta + R^2}) [P_l^2(\cos \Theta)]^2 \end{aligned} \quad (3.9)$$

where  $l$  must be set to 2.  $\sigma, \pi$  et  $\delta$  correspond in fact to  $|m| = 0, 1$  and 2 of the angular momentum.

The calculation of hopping integrals  $\beta_{ij}^{\lambda\mu}$  is similar. We can rewrite the equation (3.5) with three hopping parameters  $(dd\sigma), (dd\pi)$  and  $(dd\delta)$ . We also find the director cosines of the  $\vec{R}_j - \vec{R}_i$  vector oriented along the OZ direction. The  $\lambda, \mu$  elements of the hopping integrals are listed in tables[93,94]. Finally,  $\beta_{ij}^{\lambda\mu}$  can be written as

$$\beta_{ij}^{\lambda\mu} = \begin{pmatrix} (dd\delta) & & & & \\ & (dd\pi) & & & \\ & & (dd\pi) & & \\ & & & (dd\delta) & \\ & & & & (dd\sigma) \end{pmatrix}$$

when OZ coincides with Oz. The same treatment applies to the s and p orbitals, where the parameters are  $ss\sigma, pp\sigma$  and  $pp\pi$ . Similarly,  $s - d$  and  $p - d$  interactions involve hopping parameters noted  $sd\sigma, pd\sigma$  and  $pd\pi$ .

### 3.3 Tight-binding models for TMDs

In the last years, a number of tight binding models have been proposed to reproduce DFT band structure calculations of TMDs [27,24,26,25].

An all orbital model can be used, including non-orthogonal  $sp^3d^5$  orbitals [24]. When using a non-orthogonal tight-binding, basis functions are not constrained to be orthogonal and the overlap between them can be nonzero. This model considers only nearest-neighbor hopping matrix elements, and includes spin orbit coupling. Featuring 96 fitting parameters, the model shows good agreement with DFT band structures (shown in figure 3.1a) but it has a high computational cost and its complexity makes it impractical for studying ribbons (due to the presence of edges), disorder and realistic large system.

An alternative model is a three-orbitals model [25]. In contrast to the all orbital model, the three-orbital model considers only a superposition of  $d_{z^2}, d_{xy}$  and  $d_{x^2-y^2}$  orbitals as an orthogonal basis. The motivation behind this choice is to accurately capture the behavior near the K point, where the direct bandgap is located. While this three-orbital model exhibits good agreement with DFT (visible on figure 3.1b) in the vicinity of the K point, it falls short of accurately representing features such as the local band minimum at the Q point. The

model’s accuracy can be enhanced by increasing the number of fitting parameters from 8 to 19, which includes up to the third-nearest neighbor hoppings. However, the computational cost increases with the complexity of the model. Additionally, the orbital composition of the bands is restricted to Mo orbitals, limiting the model’s capability to correctly describe phenomena like S vacancies and reproduce the orbital composition around the  $\Gamma$  point.

Rostami *et al.*[26] introduced an intermediate model: a seven-orbitals tight-binding model. This model employs a non-orthogonal basis and neglects the  $s$  and  $p_z$  orbitals of the S atoms as well as the  $s$ ,  $d_{yz}$  and  $d_{xz}$  orbitals of the Mo atom. Similar to the three-orbitals model, the seven-orbitals model successfully reproduces the essential features around the K points but falls short of reproducing the minimum at the Q point. The band structure is visible on figure 3.1c. The main downside of this model for our specific investigation is that this model decouples the  $p_z$  orbital of S atom from other orbitals. In MoS<sub>2</sub> however, the  $p_z$  orbital of the S atom is not decoupled and plays a significant role in the transition from a direct to an indirect bandgap.

Lastly, Cappelluti *et al.*[27] described an eleven-orbitals model, combining the relatively lightness of the three-orbitals and seven-orbitals model but taking into account the  $p_z$  orbital of the S atom. The band structure is visible on figure 3.1d. This model reproduces the DFT calculation for all k-points and is less computational costly than the all-orbital model. This is the model we decided to base our work upon. For MoS<sub>2</sub>, the model considers an orthogonal basis made of all the  $4d$  Mo orbitals ( $4d_{xy}$ ,  $4d_{yz}$ ,  $4d_{xz}$ ,  $4d_{x^2-y^2}$  and  $4d_{3z^2-r^2}$ ) and the  $3p$  S orbitals ( $3p_x$ ,  $3p_y$  and  $3p_z$ ). The omission of the  $5s$  orbitals of Mo can be considered a robust approximation, given that the primary contributors to the composition of the four conduction bands and seven valence bands near the Fermi level are predominantly the five  $4d$  orbitals of Mo and the six  $3p$  orbitals of S. Together, these orbitals make up approximately 93% of the total orbital weight of these bands. It is important to note that the Cappelluti model doesn’t reproduce correctly the orbital composition of some bands and fail to describe accurately the band structure of a nanoribbon as the edges are not taken into account. Both these problems are going to be addressed in this work.

### 3.4 Hubbard model

Given our intention to investigate the magnetic properties of MoS<sub>2</sub> zigzag nanoribbons later in this study, we use a Hubbard-TB (Hubbard tight-binding) approach within the grand-canonical ensemble. The Hubbard tight-binding model is a theoretical framework used to study the behavior of electrons in strongly correlated materials. It assumes that electrons

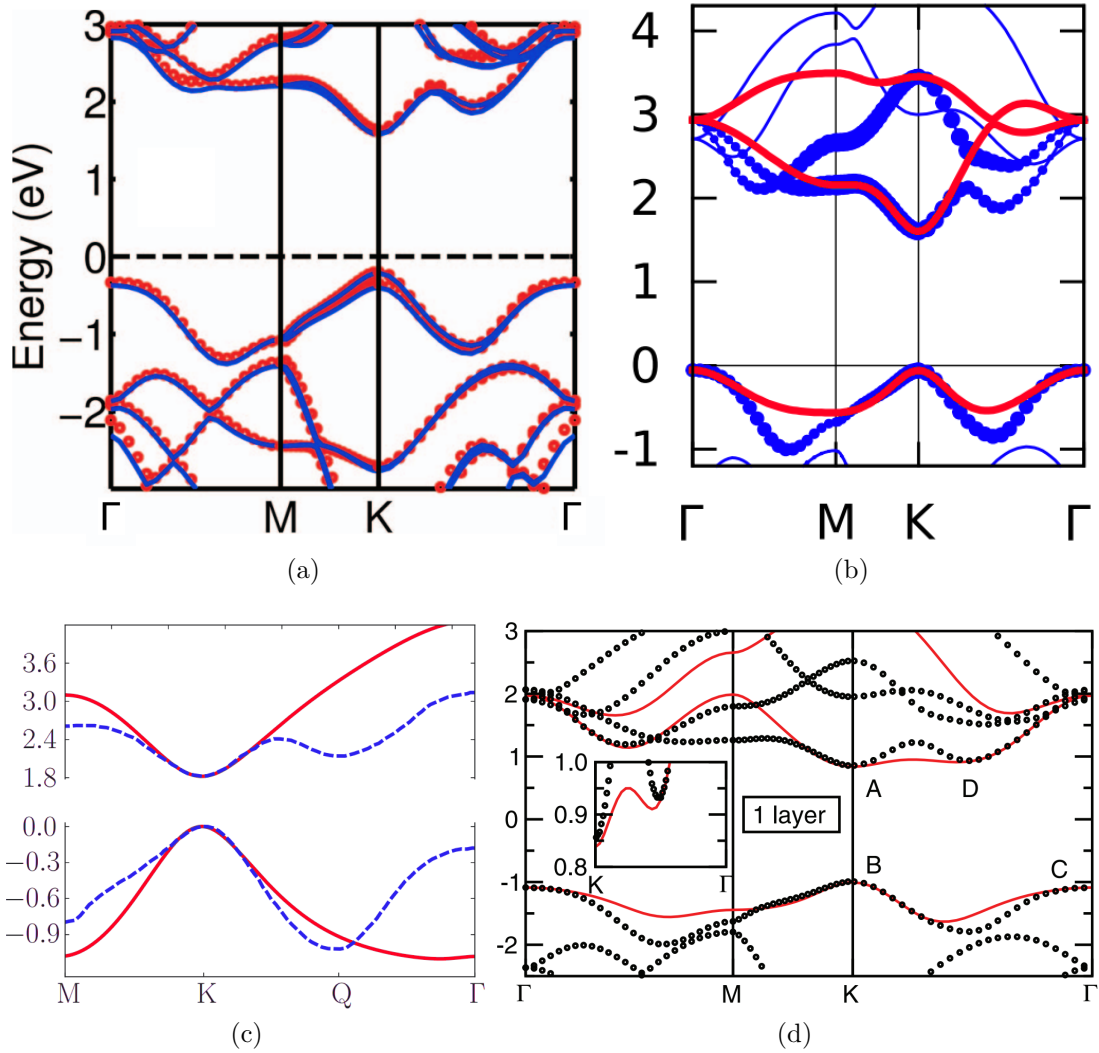


Figure 3.1: Band structures for monolayer MoS<sub>2</sub> (a) from Zahid *et al.*[24], (b) from Liu *et al.*[25], (c) from Rostami *et al.*[26] and (d) from Cappelluti *et al.*[27]. TB is in red and DFT is in blue or black.

are localized on specific sites in a lattice and incorporates the strong Coulomb repulsion between electrons on the same site, known as the on-site Coulomb interaction. The model is described by the Hubbard Hamiltonian, which includes terms for the hopping of electrons, on-site Coulomb interactions, and on-site energies. The Hamiltonian can be written in second quantization formalism in the case of MoS<sub>2</sub> with the interaction terms  $U_{Mo}$  and  $U_S$  corresponding to the five Mo and three S orbitals :

$$\mathcal{H} = \sum_{\langle ij \rangle \sigma} t_{ij} \hat{c}_{i\sigma}^\dagger \hat{c}_{j\sigma} + U_{Mo} \sum_{i \in Mo} \hat{n}_{i\uparrow} \hat{n}_{i\downarrow} + U_S \sum_{i \in S} \hat{n}_{i\uparrow} \hat{n}_{i\downarrow} + \sum_{i\sigma} (\epsilon_i - \mu) \hat{n}_{i\sigma} \quad (3.10)$$

where  $t_{ij}$  is the hopping parameters,  $c_{i\sigma}$  annihilates a fermion at site  $i$  with spin  $\sigma$  (and  $c_{i\sigma}^\dagger$  creates one),  $\epsilon_i$  is the on-site energy parameters,  $n_{i\sigma}$  the particle-number operator and  $\mu$  the chemical potential. The orbital index is ignored here for simplicity although the calculations were executed considering five orbitals for each Mo atom and three orbitals for S atoms. Given our focus on extensive systems, specifically nanoribbons, in this study, we implement the conventional mean-field decoupling of the Hubbard terms  $\hat{n}_{i\uparrow} \hat{n}_{i\downarrow} \approx n_{i\uparrow} \hat{n}_{i\downarrow} + n_{i\downarrow} \hat{n}_{i\uparrow} - n_{i\uparrow} n_{i\downarrow}$ , which yields an effective single-particle Hamiltonian that can be diagonalized either in k- or real space. For a comprehensive exploration of the mean-field approximation, refer to the in-depth discussion in Ref. [95]. The average occupation number  $n_{i,s} = \langle \hat{n}_{i,s} \rangle$  have to be adjusted self-consistently. In summary, we operate as follows: an initial value is assigned to the average occupation numbers, and subsequently, the mean-field version of the Hamiltonian 3.10 is diagonalized. The local densities of states  $\rho_{i,s}(E)$  are then computed for both spins across all atoms and orbitals. The total density of states follows by  $\rho(E) = \sum_{i,s} \rho_{i,s}(E)$  with the sum over  $i$  encompassing all orbitals of all atoms. The Fermi energy  $\epsilon_F$  and the occupation numbers are then calculated by the equations

$$N_e = \int_{-\infty}^{\epsilon_F} \rho(E) dE, \quad (3.11a)$$

$$n_{i,s} = \int_{-\infty}^{\epsilon_F} \rho_{i,s}(E) dE \quad (3.11b)$$

where  $N_e$  is the total number of electrons in the system. Once  $\epsilon_F$  has been set through 3.11b, new values are obtained for the  $n_{i,s}$  set from 3.11a. The initial values are corrected and the process is repeated until the  $n_{i,s}$  values differ from the ones of the previous iteration by less than a given tolerance.

The Coulomb interactions associated with S and Mo atoms in 3.10 were tuned to optimally match the spin-polarized DFT band structure of the nanoribbon with a thickness of six unit cells. The resulting Hubbard parameters are determined to be  $U_S = 1.7$  eV and

$$U_{Mo} = 0.6 \text{ eV.}$$

The TB+U approach offers a significant computational advantage compared to the DFT method due to its substantially lower computational burden. The Hamiltonian matrix size is 11 times the number of MoS<sub>2</sub> units. In contrast to DFT, the diagonalization of the Hamiltonian for nanoribbons comprising several hundred MoS<sub>2</sub> units can be accomplished within a reasonable computational timeframe, even considering the self-consistent iteration over the occupation numbers on the S and Mo orbitals.



# Chapter 4

## Tight-binding parametrization from DFT calculations

In this chapter, we begin by reproducing, with TB, the DFT band structures of MoS<sub>2</sub> 2H, MoS<sub>2</sub> 3R, and WS<sub>2</sub> 2H in monolayer, bilayer, trilayer, and bulk configurations. Once we establish well-defined parameters, our focus shifts to detailing zigzag MoS<sub>2</sub> nanoribbons with sulfur dimer passivation at the Mo edge. We chose this structure as it is the most stable experimentally. As we discuss in this section, describing the details of the nanoribbon band structure required us to create a new set of parameters to make sure we describe it accurately.

### 4.1 Sheets of MoS<sub>2</sub> and WS<sub>2</sub>

When using the hopping parameters and on-site energies for tight-binding determined by Cappelluti *et al.* in [27] and [28] for Mo-4 $d^5$  orbitals ( $d_{xy}, d_{yz}, d_{zx}, d_{x^2-y^2}, d_{3z^2-r^2}$ ) and S-3 $p^4$  orbitals ( $p_x, p_y, p_z$ ), as outlined in Tables 4.1 and 4.2, we successfully reproduce the DFT band structures of MoS<sub>2</sub> monolayer, bilayer and bulk forms in its 2H and 3R phases as well as those of WS<sub>2</sub> in its 2H phase as illustrated on Table 4.3.

The band structures show the same bandgap values as those obtained by Cappelluti *et al.* [27,28]. We also find the expected trend that by decreasing the number of layers, the bandgap size increases, as visible in the Table 4.4.

The bandgap values obtained from our simulations for MoS<sub>2</sub> 2H, as presented in Table 4.4, demonstrate excellent agreement with corresponding experimental optical bandgap values found in the literature (Table 4.5). The accuracy of these bandgap values is a result of fortuitous error cancellation during the fitting process. Unfortunately, the limited

availability of data for MoS<sub>2</sub> 3R hinders a more comprehensive validation of our results beyond the consistency with other numerical findings as DFT [96]. Regarding WS<sub>2</sub> 2H, our computed bandgap values appear to slightly underestimate the experimental gap by approximately 0.1-0.2 eV. This discrepancy arises from distinct physical characteristics, for example the stronger spin-orbit coupling in WS<sub>2</sub> results in less effective error cancellation compared to MoS<sub>2</sub>, leading to a more pronounced difference compared to the optical bandgap values. Despite this minor deviation, the observed difference remains within an acceptable range for the scope of our study. Importantly, this minor deviation does not alter the transition from a direct gap to an indirect gap, the position of the gap or the stacking-induced effects.

Mo	$\epsilon_{xy} = -3.025$	$\epsilon_{yz} = 0.419$	$\epsilon_{zx} = 0.419$	$\epsilon_{x^2-y^2} = -3.025$	$\epsilon_{3z^2-r^2} = -1.512$
W	$\epsilon_{xy} = -3.090$	$\epsilon_{yz} = 0.851$	$\epsilon_{zx} = 0.851$	$\epsilon_{x^2-y^2} = -3.090$	$\epsilon_{3z^2-r^2} = -1.550$
S (for MoS <sub>2</sub> )	$\epsilon_x = -1.276$	$\epsilon_y = -1.276$	$\epsilon_z = -8.236$		
S (for WS <sub>2</sub> )	$\epsilon_x = -1.176$	$\epsilon_y = -1.176$	$\epsilon_z = -7.836$		

Table 4.1: On-site energies (eV) computed by Cappelluti *et al* in [27] and [28]

S - Mo	$V_{pd\sigma} = -2.619$
	$V_{pd\pi} = -1.396$
Mo - Mo	$V_{dd\sigma} = -0.933$
	$V_{dd\pi} = -0.478$
	$V_{dd\delta} = -0.442$
S - S	$V_{pp\sigma} = 0.696$ (intralayer); $-0.774$ (interlayer)
	$V_{pp\pi} = 0.278$ (intralayer); $0.123$ (interlayer)

Table 4.2: Hopping parameters (eV) computed by Cappelluti *et al* in [27] and [28]

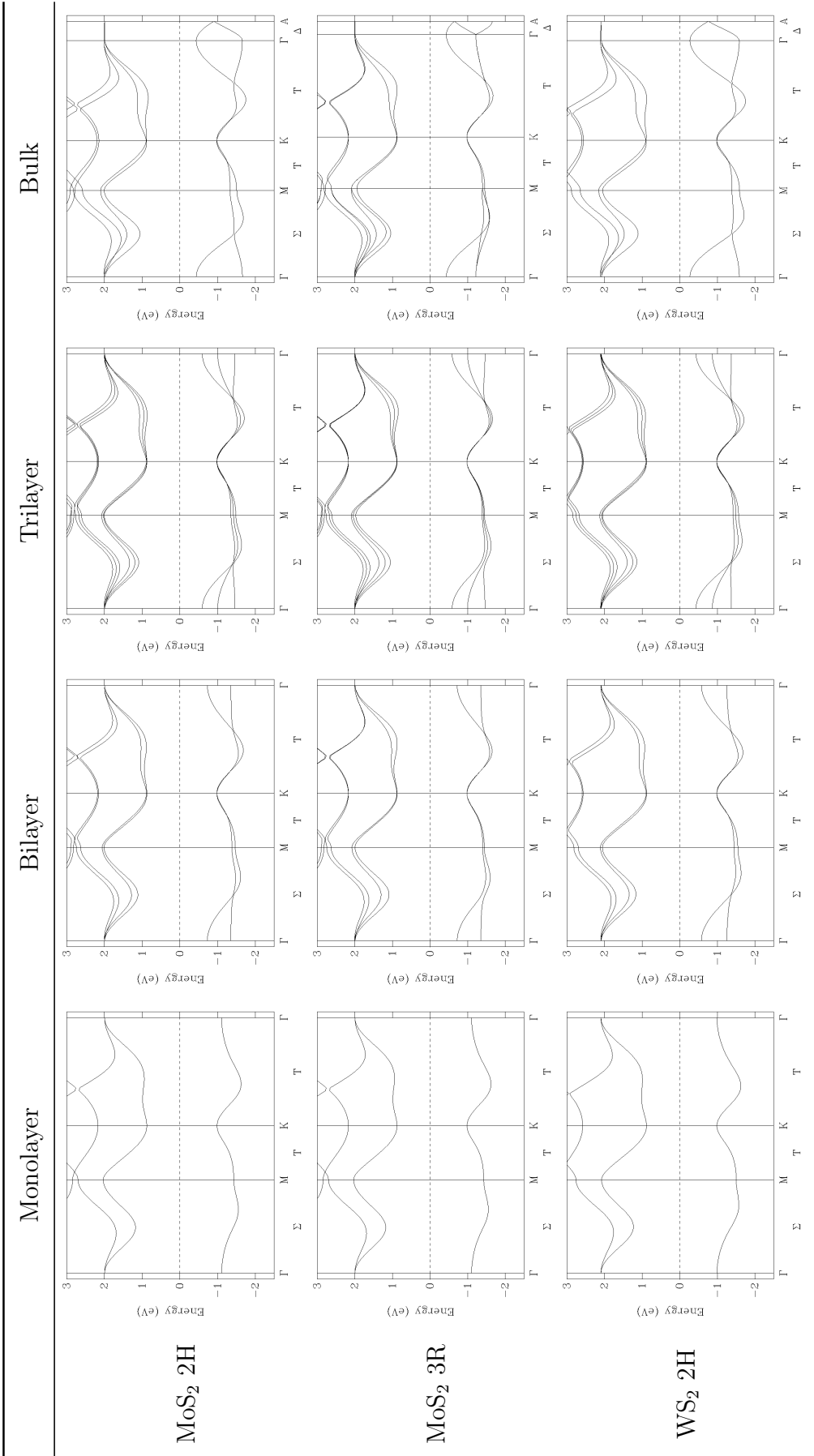


Table 4.3: TB-band structures

	Monolayer	Bilayer	Trilayer	Bulk
MoS <sub>2</sub> 2H	1.859 eV	1.605 eV	1.460 eV	1.271 eV
MoS <sub>2</sub> 3R	1.859 eV	1.594 eV	1.431 eV	1.307 eV
WS <sub>2</sub> 2H	1.871 eV	1.463 eV	1.320 eV	1.152 eV

Table 4.4: Bandgap values measured on the band structures obtained by TB

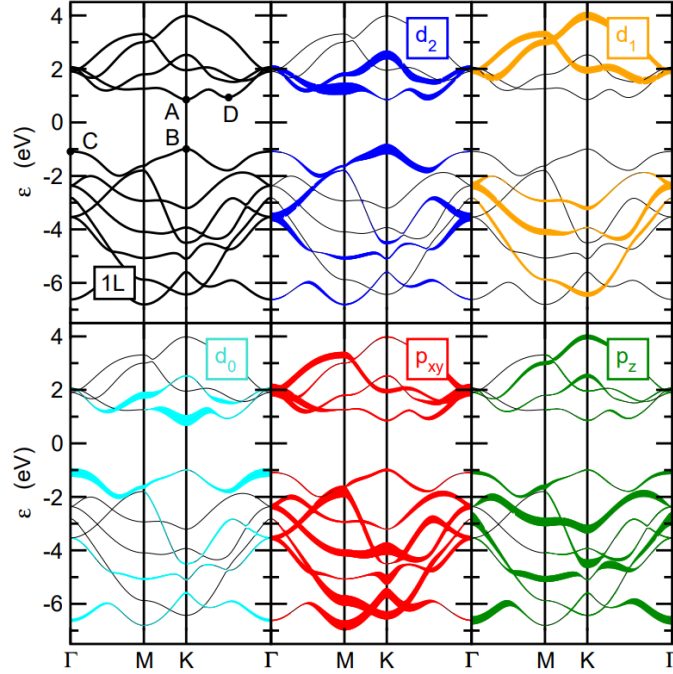
	Monolayer	Bilayer	Trilayer	Bulk
MoS <sub>2</sub> 2H	1.8-1.9 eV [11]	1.6 eV [97]	/	1.29 eV [11]
MoS <sub>2</sub> 3R	1.8-1.9 eV [11]	/	/	/
WS <sub>2</sub> 2H	2.0 eV [98]	/	/	1.3 eV [99]

Table 4.5: Optical bandgap values obtained experimentally from PL measurements

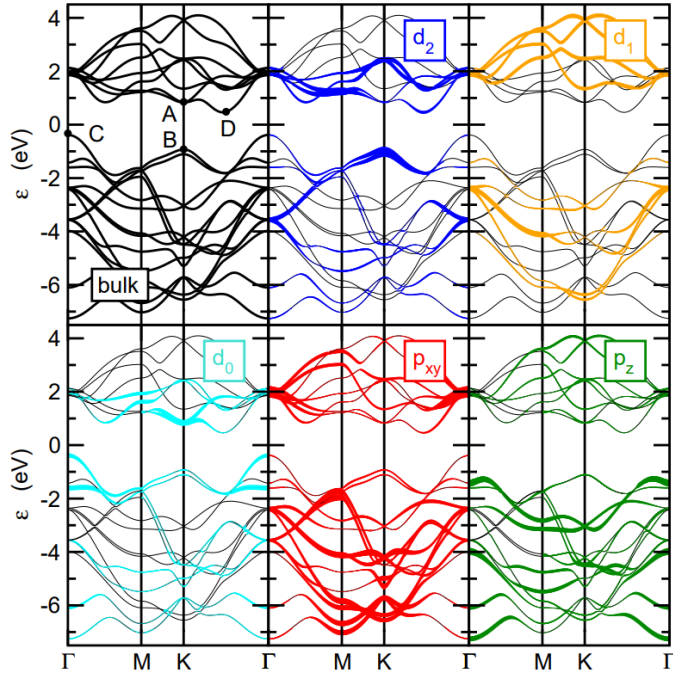
Material	Layer(s)	Conduction band minimum ( $\text{\AA}^{-1}$ )	Valence band maximum ( $\text{\AA}^{-1}$ )	Direct or indirect
MoS <sub>2</sub> 2H	monolayer	K (0.663;1.148;0.0)	K (0.663;1.148;0.0)	Direct
	bilayer	Q (0.672;1.132;0.0)	$\Gamma$ (0.0;0.0;0.0)	Indirect
	trilayer	Q (0.376;0.652;0.0)	$\Gamma$ (0.0;0.0;0.0)	Indirect
	bulk	Q (0.376;0.652;0.0)	$\Gamma$ (0.0;0.0;0.0)	Indirect
MoS <sub>2</sub> 3R	monolayer	K (0.663;1.148;0.0)	K (0.663;1.148;0.0)	Direct
	bilayer	Q (0.358;0.621;0.0)	$\Gamma$ (0.0;0.0;0.0)	Indirect
	trilayer	Q (0.358;0.621;0.0)	$\Gamma$ (0.0;0.0;0.0)	Indirect
	bulk	Q (0.358;0.621;0.0)	$\Gamma$ (0.0;0.0;0.0)	Indirect
WS <sub>2</sub> 2H	monolayer	(0.664;1.151;0.0)	(0.664;1.151;0.0)	Direct
	bilayer	Q (0.673;1.135;0.0)	$\Gamma$ (0.0;0.0;0.0)	Indirect
	trilayer	Q (0.664;1.151;0.0)	$\Gamma$ (0.0;0.0;0.0)	Indirect
	bulk	Q (1.395;0.684;0.0)	$\Gamma$ (0.0;0.0;0.0)	Indirect

Table 4.6: Positions of conduction band minimum and valence band maximum for MoS<sub>2</sub> and WS<sub>2</sub> in different layer configurations.

For all three TMDs, we notice a change from a direct bandgap at K point in monolayers to an indirect  $\Gamma$ Q one in bilayers and beyond, as visible in Table 4.6. The bandgap consistently maintains a high value, exceeding 0.4 eV which is the usual threshold for envisioning transistor applications. In the literature, a MoS<sub>2</sub> monolayer transistor exhibits an ON and OFF current ratio of  $10^8$  at room temperature, coupled with minimal leakage current [39,100]. This shift from a direct bandgap in monolayers to an indirect one in the bulk is well described by Cappelluti *et al.* [28]. They attribute this transition to the separation of energy levels in sulfur's  $p_z-p_z$  orbitals, responsible for interlayer coupling. It is noteworthy that the  $p_{x/y}-p_{x/y}$  and  $p_z - p_{x/y}$  orbitals exert marginal influence on this separation. Therefore, at point C and D in figure 4.1 the interlayer interactions have a strong effect (splitting the bands and thus pushing down the D minimum and lifting the C maximum) while it is insignificant at points A and B. This discrepancy causes the shift from a direct A-B bandgap to an indirect C-D bandgap. The stacking of layers eliminates degeneracy at the  $\Gamma$  point and along the K $\Gamma$  line, resulting in a consistent shift and reduction in the bandgap. This distinctive characteristic holds significant potential for a wide range of electronic applications.



(a)



(b)

Figure 4.1: DFT band structure and orbital character of (a) single-layer MoS<sub>2</sub> and (b) bulk MoS<sub>2</sub>. For each system, the top left panel shows the full band structure while, in the other panels, the thickness of the bands represents the orbital weight, where the  $d$ -character ( $d_2 = d_{x^2-y^2}$ ,  $d_{xy}$ ,  $d_1 = d_{xz}$ ,  $d_{yz}$ ,  $d_0 = d_{3z^2-r^2}$ ) refers to the Mo atom  $4d$  orbitals, while the  $p$ -character ( $p_{xy} = p_x$ ,  $p_y$ ) refers to  $2p$  orbitals of sulfur [27]

## 4.2 Zigzag MoS<sub>2</sub> nanoribbons with sulfur dimer passivation of the Mo edge

Since the parameters we used (from [27,28]) were deduced to describe infinite slabs of MoS<sub>2</sub>, they fail to describe accurately the band structure of a nanoribbon as the edges are not taken into account. The comparison between the DFT band structure and the TB band structure with those parameters can be found on figure 4.2 (figure a) and c) respectively). Thus, the first step was to modify the on-site energy parameters of the edge atoms in order to quantitatively reproduce the DFT band structure calculations. The adjustment of on-site energies involved a meticulous trial-and-error process, with a strong emphasis on maintaining the accurate orbital dependencies.

As the goal was to be as close as possible to what could be found experimentally, we focused on MoS<sub>2</sub> nanoribbons with zigzag edges as it is more stable than armchair. One edge is S-terminated and the other one is Mo-terminated passivated with S dimers since it is the most stable configuration according to both theoretical predictions and experimental observations (see chapter two for more details).

To reproduce the shape of the band structure and the mid-gap states calculated by DFT, it was necessary to describe individually the atoms on the edges as well as the S dimer (outlined on figure 4.3) using the fine-tuned parameters shown in Table 4.7. For our parametrization, we set the nanoribbon width (measured by the count of zigzag lines across it) to a value of 6 which corresponds to 30.97 Å. This choice is the minimal value effectively preventing electronic interaction between the two edges, therefore our parametrization is valid to describe wider nanoribbons. From the DFT calculations, we can say that the mid-gap states shown in blue (◇) and green (□) colors on figure 4.2 correspond to the S edge while red (△) and yellow (○) colors correspond to the Mo edge as represented on figure 4.3. Three of them cross the Fermi level, implying the existence of metallic states in agreement with previous results [59,101]. From the charge density plot from DFT around the Fermi level visible on figure 4.4, the S dimers in the Mo-edge have  $p_x$  orbital character in contrast to the S-edge where the  $p_z$  orbitals of the S atoms dominate, forming one-dimensional metallic states strongly localised along the edges. With our parametrization, the orbital dependency of each mid-gap states is correctly reproduced. The three mid-gap states crossing the Fermi level have a shape that is similar to the DFT predicted ones whereas the last one has a lower dispersion. This discrepancy is not of prime importance as it concerns a band that does not cross the Fermi level and is thus not responsible of the metallic behaviour.

This first step done, we now take into account the magnetic properties of the zigzag

-	Mo atom	S atom	S dimer
Mo edge	-2.03, 1.42, 1.42, -4.03, 0.51	0.28, -8.28, -12.24	-0.55, -5.28, -8.24
S edge	-2.03, 4.30, -0.80, -12.03, -2.60	-1.90, 0.18, -6.50	-

Table 4.7: Modified tight-binding on-site energy parameters for the edge atoms in units of eV. Values corresponds to the five orbitals ( $4d_{xy}, 4d_{yz}, 4d_{xz}, 4d_{x^2-y^2}, 4d_{3z^2-r^2}$ ) for Mo atoms and three orbitals ( $3p_x, 3p_y, 3p_z$ ) for S atoms.

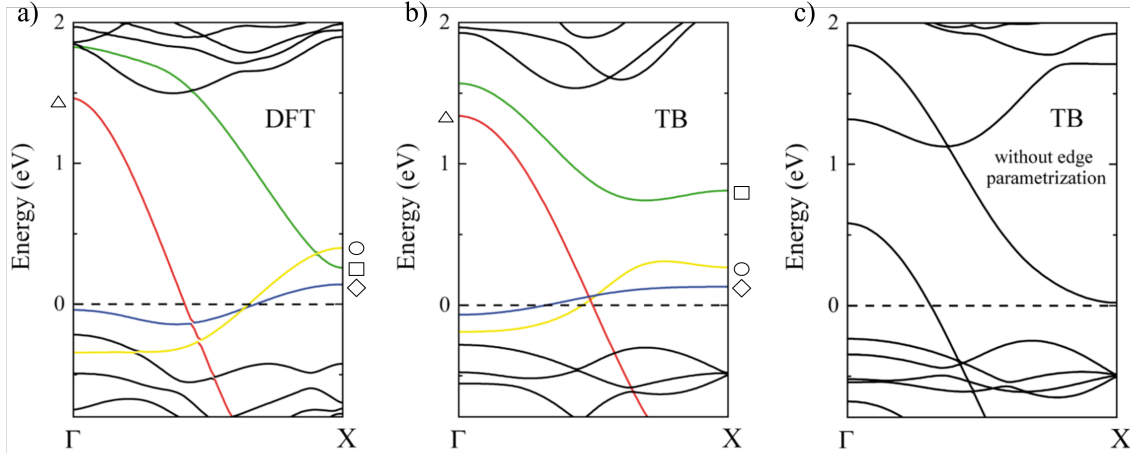


Figure 4.2: Non spin-polarized band structure calculations of the zigzag MoS<sub>2</sub> nanoribbon with sulfur dimer passivation ( $n = 6$ ). (a) DFT calculation, (b) TB calculation using the modified TB parameters (Table 4.7) for the edge atoms, (c) TB calculation without the edge parametrization. Midgap states originated from the edge atoms are marked by different colors according to figure 4.3. States with blue ( $\diamond$ ) and green ( $\square$ ) colors correspond to the S edge, while red ( $\Delta$ ) and yellow ( $\circ$ ) colors correspond to the Mo edge.

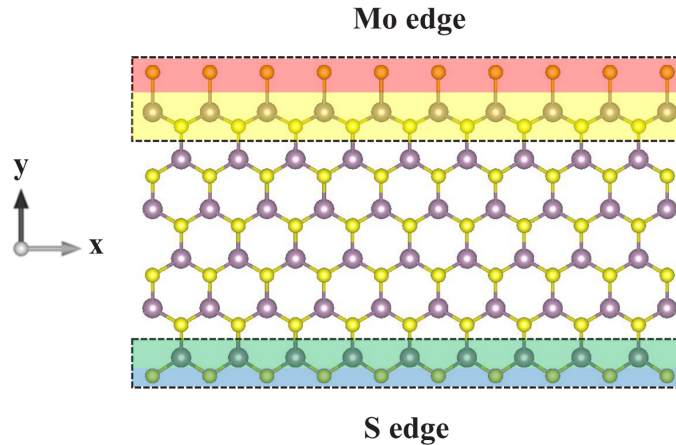


Figure 4.3: Top-view of a zigzag MoS<sub>2</sub> nanoribbon with sulfur dimer passivation. Purple and yellow spheres represent molybdenum and sulfur atoms. Coloured rectangles represent atoms that needed other on-site energies parameters (see Table 4.7) than MoS<sub>2</sub> layers.

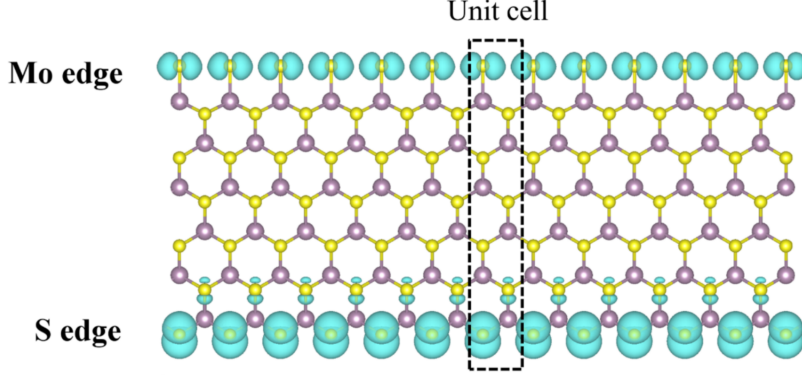


Figure 4.4: Charge density plot around the Fermi level calculated by DFT. The isovalue was set to be  $2 \times 10^{-3} e/\text{\AA}^3$

nanoribbon. In order to do this, we switched to a Hubbard-TB approach using a grand-canonical ensemble and interaction terms  $U_{Mo}$  and  $U_S$  corresponding to the five Mo and three S orbitals. The average occupation numbers  $n_{i,s} = \langle \hat{n}_{i,s} \rangle$  have to be adjusted self-consistently as described in Chapter 3. The Hubbard interactions terms related to the S and Mo atoms were adjusted so as to best fit the spin-polarized DFT band structure of the nanoribbon. The obtained values of the Hubbard parameters are  $U_S = 1.7$  eV and  $U_{Mo} = 0.6$  eV.

As depicted in figure 4.5, the impact of spin-polarization is mainly noticeable on the band originating from the S atoms at the S edge, depicted in blue in Figure 4.2 and referred to as the "magnetic band" here below. The partially filled spin-up band undergoes a slight upward shift to higher energy levels, resulting in decreased occupancy. Meanwhile, the spin-down band descends significantly below the Fermi level, leading to complete filling of this band. Notably, there is almost no magnetic moment on the Mo edge due to the dimer passivation of the Mo atoms. Following the notation in [102], the magnetic ground state corresponds to the  $F_M$  phase, indicating ferromagnetic ordering of the spins on the S edge of the nanoribbon.

The exclusion of spin-orbit coupling (SOC) from our work is justified for the following reason. In monolayer TMDs, the absence of inversion symmetry leads to SOC lifting the spin degeneracy of electronic bands [103]. The extent of spin splitting depends on the dominant orbitals characterizing the bands. It is important where the  $d_{xy}$  and  $d_{x^2-y^2}$  orbitals of the transition metal dominate the character of a band. By contrast, the splitting is very small for the bands that involve mainly the  $d_{3z^2-r^2}$  orbital of the transition metal and/or the  $p_z$  orbital of the chalcogenides [104]. To investigate the impact of SOC, we conducted spin-polarized

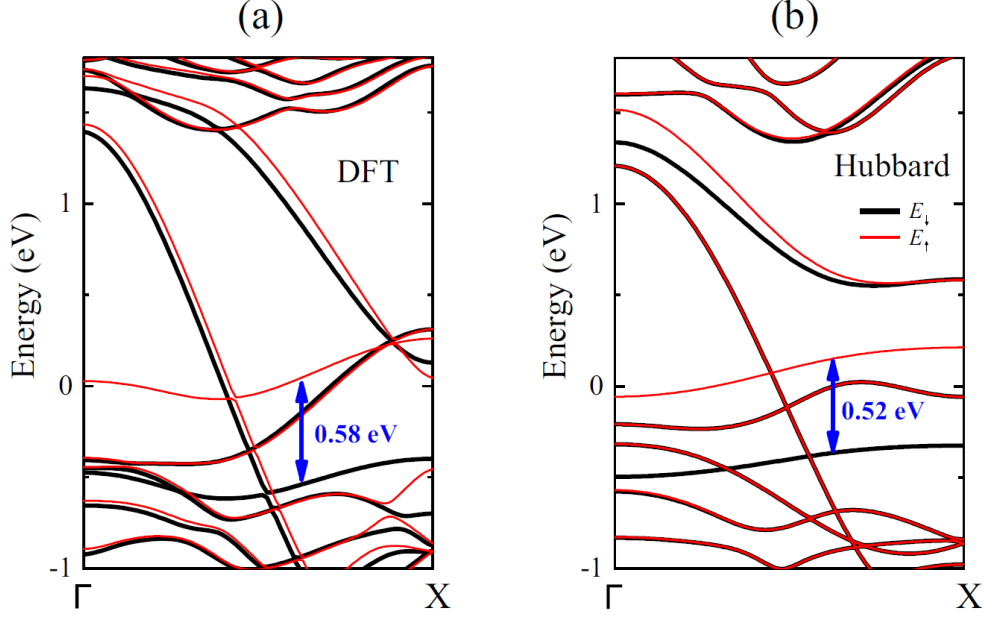


Figure 4.5: Spin-polarized band structure calculations of the ( $n = 6$ ) zigzag  $\text{MoS}_2$  nanoribbon (a) by using DFT and (b) derived from a Hubbard model with  $U_S = 1.7$  eV and  $U_{Mo} = 0.6$  eV parameters. Red and black curves correspond to the up and down spins respectively.

DFT calculations for a  $\text{MoS}_2$  nanoribbon<sup>1</sup>, visible on figure 4.5. The results indicate that SOC has a negligible effect on the magnetic band discussed here above, given its dominant  $3p_z$  character. Along the  $\Gamma X$  line in the ribbon’s band structure, the splitting remains consistent, with or without SOC, exhibiting variations within 5 meV. This observation underscores that the magnetic band’s splitting is attributed to electron-electron interactions rather than spin-orbit coupling. In essence, SOC does not alter the spin polarization plot. This is advantageous as integrating SOC into a TB+U Hamiltonian would introduce new empirical parameters in the form of SOC constants [105], necessitating validation for the nanoribbon geometry.

The dispersion of the magnetic band has a cosine-like function shape similar to what is obtained in calculating the band structure of a linear chain of atoms containing a single orbital on every site. Thus, this band seems to be suitable for a one-dimensional chain model which will allow us to have a interesting toy model to study, in a more systematic way, the effect of spin reversal across different scales and sites. While this approach simplifies the problem, we believe that it captures an essential aspect of the physics involved. The reason is that the magnetic band (blue curve in figure 4.2) we focus all our attention on is weakly interacting with neighboring bands. Indeed, the black curves are bulk states having little weight at the edge atoms. The green branch originates from the same S edge as the blue one but remains unoccupied, thereby not influencing the system’s properties at 0 K. Additionally,

<sup>1</sup>P. Vancsó, work in progress (2023)

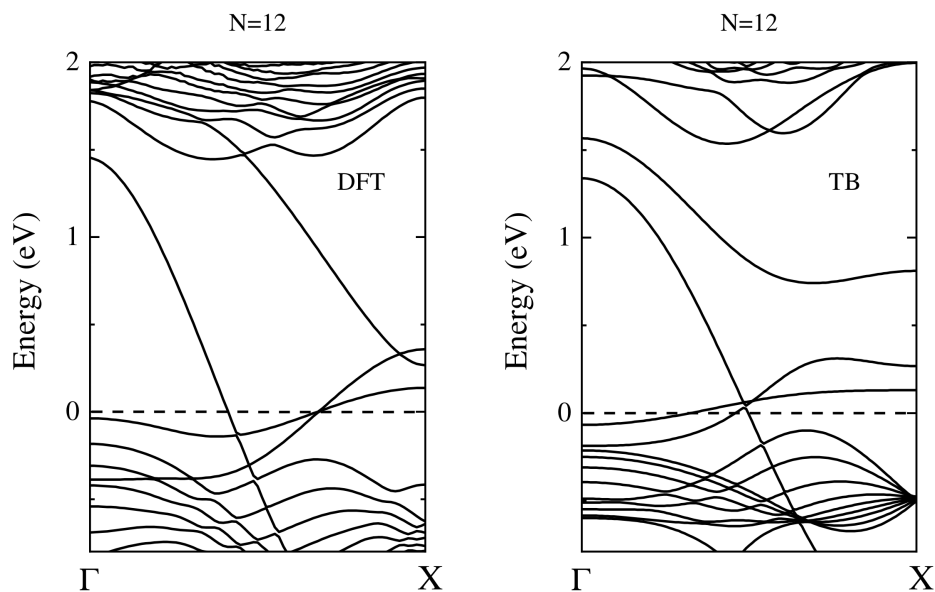


Figure 4.6: Non spin-polarized band structure calculations of the zigzag  $\text{MoS}_2$  nanoribbon with sulfur dimer passivation ( $n = 12$ ). (a) DFT calculation, (b) TB calculation using the modified TB parameters (Table 4.7) for the edge atoms

the red and yellow branches arise from electronic states localized on the opposite edges of the nanoribbon. When the width of the nanoribbon is doubled, nothing changes in the relative position and shape of the mid-gap bands as visible on figure 4.6 [61]. This implies that even with a thickness of only six units cells, the edges of a zigzag nanoribbon operate independently. Consequently, it is a reasonable approximation to treat the magnetic band as decoupled from the other bands.

# Chapter 5

## Defects and disorder

As illustrated in the previous section, using a suitable tight-binding (TB) parametrization at the edges enables the derivation of both electronic and magnetic characteristics of a zigzag nanoribbon. In this section, we discuss the domain wall in MoS<sub>2</sub> nanoribbons and investigate the impact of local perturbations on these nanoribbons. Furthermore, we initiate a discussion on preliminary findings regarding sulfur vacancies in nanosheets.

### 5.1 Domain wall in nanoribbons

Using the parameters of the unit-cell calculations, we scale up the system size to scrutinize the magnetic properties of a 40-unit-cell-long (using periodic boundary conditions in the  $x$  direction and  $L_x = 12.8$  nm) nanoribbon within the framework of the Hubbard model.

First, we investigate collinear domain walls at the S edge by rotating manually half of the spins in the supercell geometry and then letting the system relax. Figure 5.1 provides a visual representation of the spin density distribution for both the ferromagnetic ground state (figure 5.1a) and the excited state featuring collinear domain walls (figure 5.1b). The spin densities of the S atoms at the S edge, encompassing both the upper and bottom layers, reveal the effective localization of the domain wall within just one unit cell (equivalent to 0.3 nm). Additionally, the magnetization exhibits weak oscillations around the transition zone (figure 5.1c).

Remarkably, we make the surprising observation that the energy required for creating a collinear domain wall is merely  $E_{dw} = +6.5$  meV, calculated from TB+U. This value is more than one order of magnitude lower compared to the case of zigzag graphene nanoribbons, where  $E_{dw} = +114$  meV according to DFT [106].

The pronounced localization and the low energy associated with the domain wall collectively suggest a weak magnetic coupling along the S edge. To estimate this magnetic coupling, we assess the quadratic energy-wave vector dispersion relation

$$E(q) = Dq^2 \quad (5.1)$$

where  $D$  represents the spin wave exchange stiffness constant. Indeed, the quadratic energy-vector dispersion provides a theoretical foundation for describing the behavior of magnetic moments of materials and is commonly used in similar system, making it an useful tool to compare with other structures. Those calculations were computed by P. Vancsó and I. Hagymási. From the different  $q$  vector calculations, we determine the spin stiffness constant to be  $D = 161 \text{ meV } \text{Å}^2$ , which is approximately half the value observed in zigzag graphene nanoribbons ( $D = 320 \text{ meV } \text{Å}^2$ ) [106].

The observed weaker coupling in our system, compared to zigzag graphene nanoribbons, can be attributed to the different geometries and electronic properties of the two materials. Regarding geometry, the distance between zigzag S edge atoms is  $3.18 \text{ Å}$ , larger than the distance between C atoms in graphene nanoribbons ( $2.46 \text{ Å}$ ). This larger separation in  $\text{MoS}_2$  can diminish the interaction between the edge atoms. Additionally, the nearest-neighbor atoms that can mediate magnetic coupling between the edge atoms differ between the two materials (C atoms in graphene and Mo atoms in  $\text{MoS}_2$ ). The magnetic coupling through the middle-layer Mo atom may differ from the coupling through the in-plane C atom in graphene.

In addition to disparities in edge geometries, notable distinctions exist in electronic properties. Unlike  $\text{MoS}_2$ , where the S atom bands exhibit a small yet finite energy dispersion (figure 4.2), the edge states in zigzag graphene nanoribbons manifest almost flat bands. The nearly flat bands in graphene nanoribbons contribute to a higher density of states, potentially intensifying electron-electron interaction effects and, consequently, enhancing magnetic coupling.

We corroborated the observed weak coupling by conducting DFT calculations in a double unit-cell geometry of a zigzag  $\text{MoS}_2$  nanoribbon. The states featuring ferromagnetic ( $\uparrow\uparrow$ ) and antiferromagnetic ( $\uparrow\downarrow$ ) spin ordering at the edges display a mere 14 meV difference in energy according to DFT which is indeed a one-order difference compared to the 114 meV predicted by DFT for graphene. Notably, similar small energy differences between ferromagnetic and antiferromagnetic states were reported in zigzag  $\text{WS}_2$  nanoribbons [107], emphasizing parallel magnetic mechanisms in layered structures of  $\text{MoS}_2$  and  $\text{WS}_2$ .

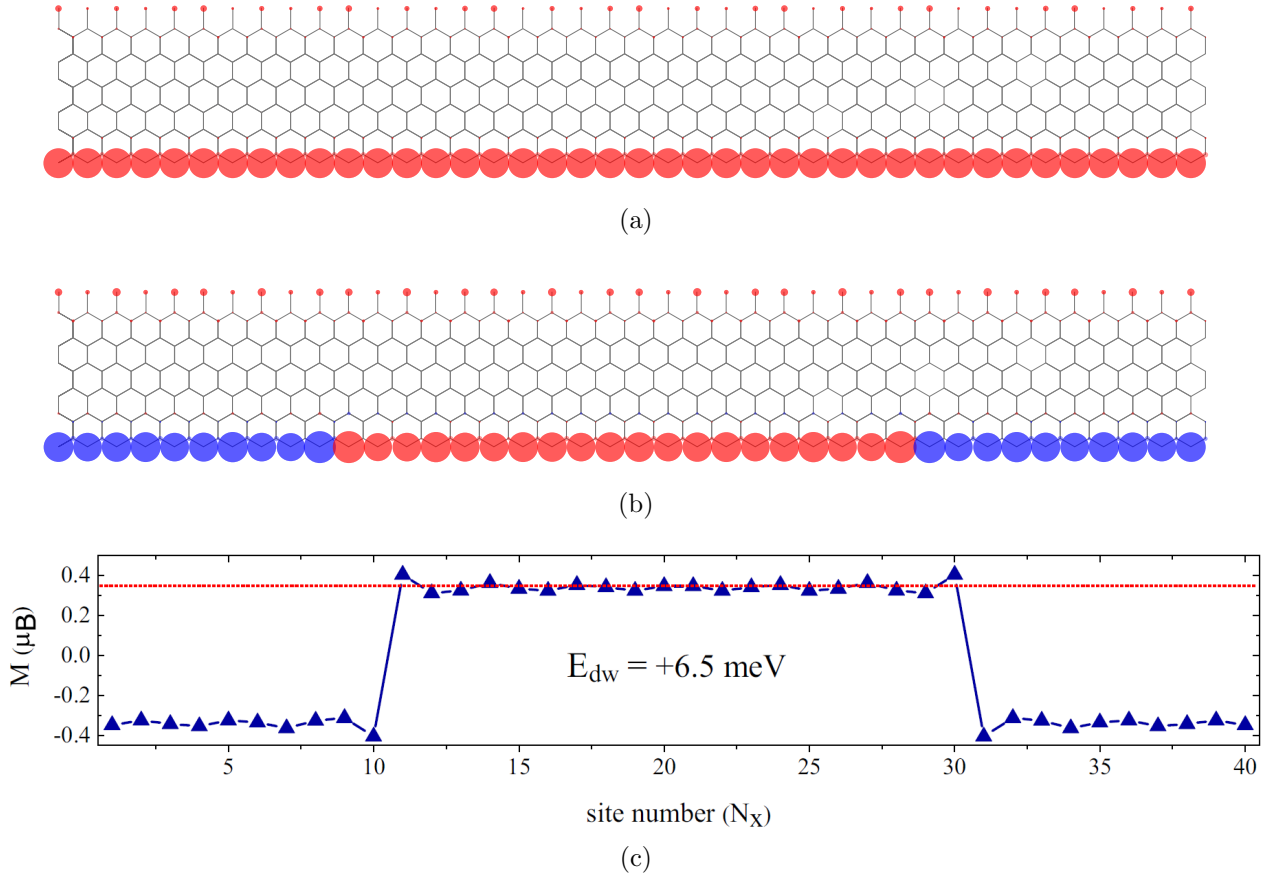


Figure 5.1: Spin density plots of the zigzag  $\text{MoS}_2$  nanoribbon. (a) Top view of the ferromagnetic ground state and (b) the collinear domain-wall excitation at the S edge. Blue and red circles correspond to spin-up and spin-down electrons, respectively. (c) Magnetic moments at the edge on the S atoms in the presence of the domain wall. For comparison the red dashed line shows the ground-state magnetic values.

## 5.2 Local perturbations in nanoribbons

Defects and disorder can significantly modify the intrinsic properties of the materials. In the context of zigzag  $\text{MoS}_2$  nanoribbons, transport calculations have revealed a significant suppression of conductance when confronted with edge disorder [108,109,110].

Motivated by the noted weak magnetic coupling at the S edge, we investigate the robustness of the magnetization against both short- and long-range disorder. To simulate disorder within the system, we incorporate the superposition of  $N$  Gaussian potentials to to the on-site energy parameter in the Hamiltonian (equation 3.10):

$$V_i = \sum_{k=1}^N V_0 e^{-|\vec{r}_i - \vec{r}_k|^2 / 2\sigma^2} \quad (5.2)$$

where  $\vec{r}_k$  is the position of the  $k$ th Gaussian center,  $\vec{r}_i$  is the position of the atomic site  $i$ , and  $V_0$  and  $\sigma$  are Gaussian parameters corresponding to the strength and the range of the disorder, respectively. In the case of specific defects, like vacancies or adatoms, are present, modifications to the on-site and hopping parameters of the TB model become necessary to accurately characterize the defect properties. However, in our case, by using the combination of our edge parametrization and Gaussian potentials, we can investigate both short- and long-range disorder in the system without the need for additional modifications to the TB parameters. This disorder potential can also be regarded as an inhomogeneous charge distribution across the substrate [111].

For our analysis, we use eight randomly distributed Gaussian potentials in the system ( $N = 8$ ), including disorder along the edges as well as the inner part of the nanoribbon. These Gaussian potentials are indicated by the centers of the black circles in figure 5.2. We consider both repulsive and attractive potentials with  $V_0$  values of  $\pm 100$  meV, along with  $\sigma$  values of 1, 3, and 5 in angstroms, corresponding to disorder localized from one atom to extended defects exceeding nanometer dimensions.

Figure 5.2 illustrates the calculated magnetic ground states of the system in the case of a positive disorder potential ( $V_0 = +100$  meV). In figure 5.2a, we can recognize the ferromagnetic ground state at the S edge for strongly localized perturbation potentials ( $\sigma = 1$  Å). We observed that disorder localized in the middle of the nanoribbon does not impact its magnetic properties. However, disorder introduced on the S atoms at the S edge causes a slight increase in magnetic moments, shifting from the defect-free value of  $M = 0.35 \mu_B$  to  $M = 0.41 \mu_B$ . The enhanced magnetic moments of the S atoms, where the potentials are centered, can be explained by examining figure 5.2b, where  $\sigma = 3$  Å. The positive potential induces a positive energy shift in the mid-gap bands, leading to a decrease in occupancy of the partially filled spin-up band of the S atoms at the edge (see figure 5.3 for a graphical representation). Meanwhile, the spin-down band remains significantly below the Fermi level, maintaining full occupancy in the presence of the potential. Consequently, this results in higher magnetic moments for the S atoms.

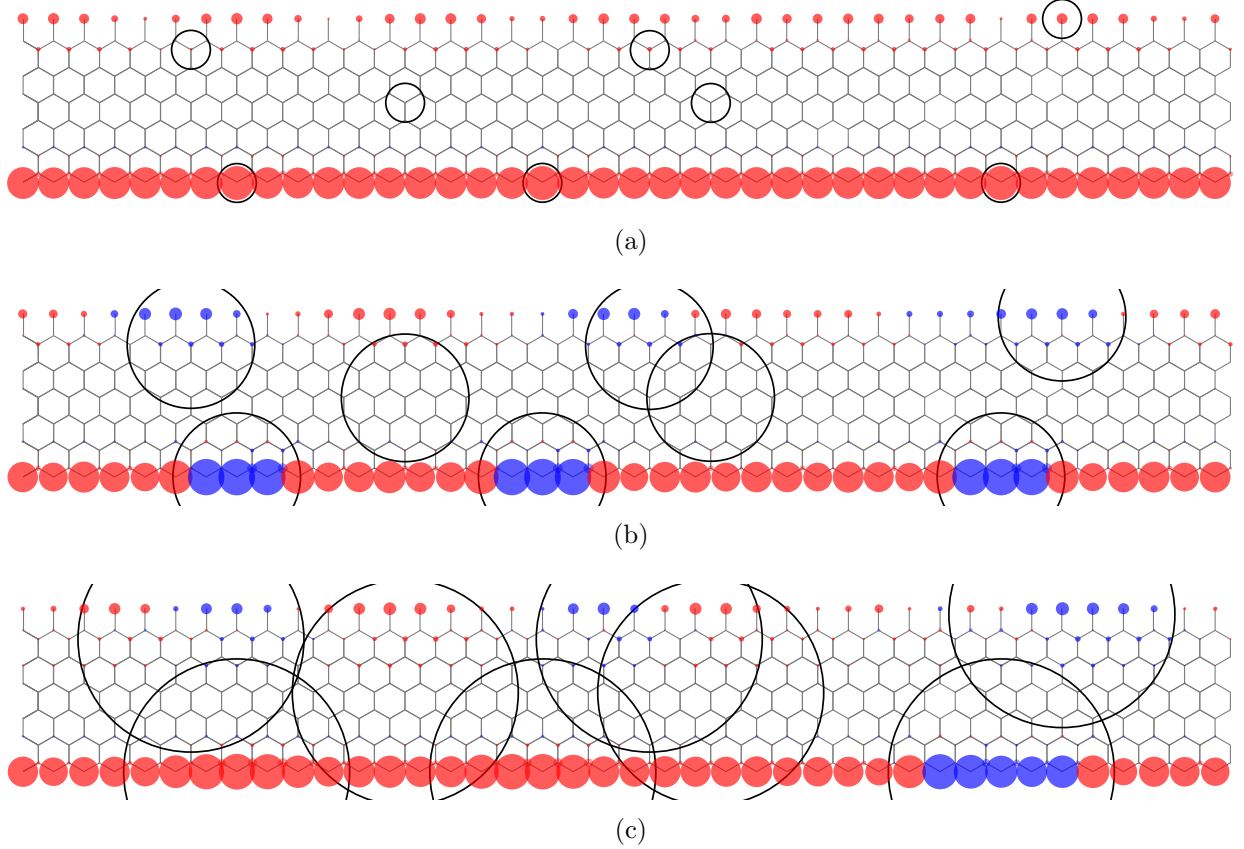


Figure 5.2: Spin density plots in the presence of disorder. (a)–(c) Top view of the magnetic ground states of the zigzag nanoribbons by using Gaussian potentials with  $V_0 = +100$  meV and different width parameters  $\sigma = 1, 3,$  and  $5$  in angstroms. Black circles denote the positions of the randomly distributed potentials. The radii of the circles correspond to the sizes of the potentials. Blue and red circles correspond to spin-up and spin-down electrons, respectively.

In contrast to the previous result with  $\sigma = 1$  Å potentials with the  $\sigma = 3$  Å parameter, extending over three-atom distances, induce substantial changes in the magnetic ground state (visible on figure 5.2b). Most notably, in regions where the potentials are applied, the orientation of magnetic moments undergoes alteration ( $M = -0.47 \mu_B$ ). The lower energy of the observed state compared to the ferromagnetic state suggests that potentials act in a more intricate manner than in the previous  $\sigma = 1$  Å case. The potentials modify both Mo and S atom bands in the potential region, leading to the formation of domain walls along the edges. Similar changes in magnetic moments are observed at the Mo edge, where the S dimers exhibit significantly smaller magnetic moments ( $M = \pm 0.05 \mu_B$ ).

Further increasing the radius of individual Gaussian potentials ( $\sigma = 5$  Å) results in overlapping regions at the edges (visible on figure 5.2c). Magnetic calculations reveal that in

the case of the overlapping region, the ferromagnetic ground state is restored at the S edge. In contrast, non-overlapping regions at the S edge give rise to domain walls. The correlation between the potential and the magnetic texture is visible on figure 5.4. This outcome suggests that, besides the width, the profile of the potential also plays a crucial role in determining the magnetic ground state of the system.

Due to the absence of electron-hole symmetry in the system, the introduction of a negative disorder potential ( $V_0 = -100$  meV) leads to distinct magnetic properties. The attractive potential induces a negative shift in the energy bands, resulting in reduced magnetic moments for the S atoms at the S edge (see figure 5.3 for a graphical representation). Specifically, for strongly localized potentials ( $\sigma = 1$  Å), the magnetic moments decrease to  $M = 0.23 \mu_B$  on the S atoms where the negative potentials are applied. Consequently, it can be inferred that band shifting of the S atoms with positive potentials leads to increased magnetic moments at the edge whereas with negative potentials, it leads to decreased magnetic moments compared to the defect-free system. Further investigation of the negative potential with extended defects ( $\sigma = 3$  and  $5$  Å) reveals that, in both cases, a ferromagnetic ground state occurs at the S edge, contrary to the positive potential case where the formation of domain walls is predicted.

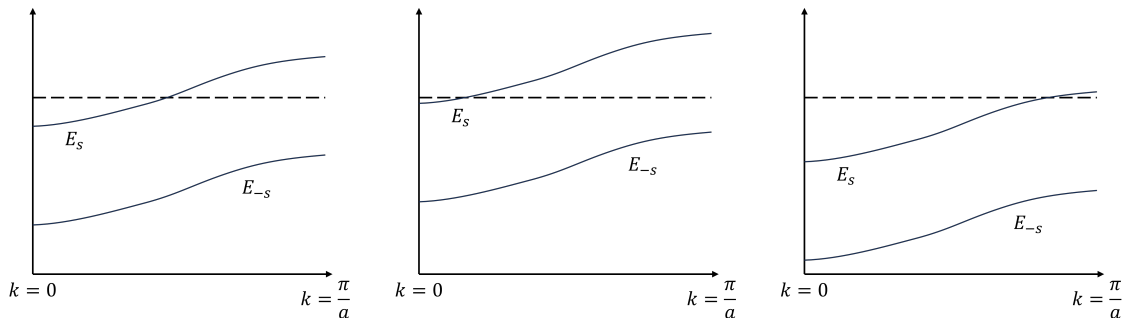


Figure 5.3: Graphical representation of the spin-polarized magnetic band for (a)  $V_0 = 0$  meV, (b)  $V_0 > 0$  and (c)  $V_0 < 0$

Summarizing the magnetic calculations in the presence of disorder, significant alterations in the magnetic ground state are observed in the case of a positive potential, which is relevant to frequently encountered n-doped MoS<sub>2</sub> samples [112,113]. Despite changes in the values of magnetic moments for short-range disorder, the ferromagnetic arrangement is consistently preserved at the S edge.

Expanding the range of disorder not only modifies the values of magnetic moments but also influences their direction, resulting in the formation of spin domain walls, which are also sensitive to the profile of the potential. The energy differences of the ground states and

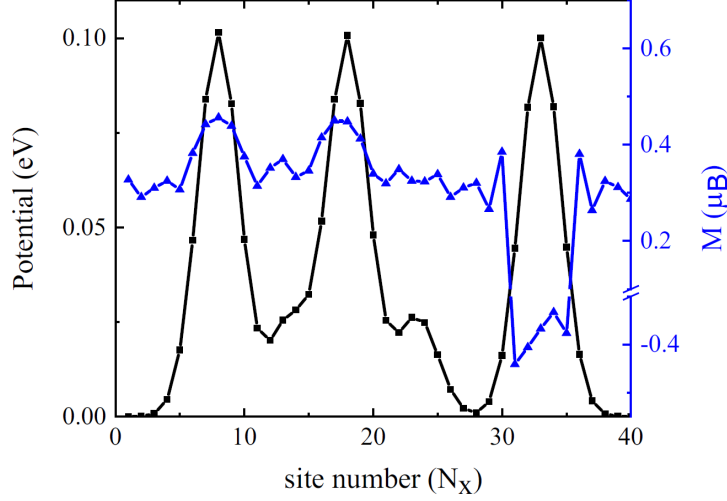


Figure 5.4: Potential profile and magnetic moments along the S edge. Black and blue curves correspond to the potential ( $\sigma = 5\text{\AA}$ ) and magnetic values of the S atoms at the S edge. The magnetic moments are following the potential profile. Ferromagnetic orientation of the spins occurs where the Gaussian potentials have an overlapping region, while domain walls appear in the non-overlapping region.

excited states in the different disorders are on the order of tens of meV in the system. This behavior finds a qualitative analogy when considering the edge magnetic moments within a one-dimensional Ising model, as demonstrated in the case of graphene with zigzag edges [106].

In this context, the effects of disorder parallel the impact of random fields in the Ising model, where the formation of domain walls has been predicted [114,115,116]. In such systems, the creation of domain walls arises from the interplay between the domain wall energy and the properties of the applied field. In our case, the properties of the positive disorder potential seem to play a comparable role. This ability to modify the spin texture through potential disorder holds promise for spintronic applications. By applying periodic or non-periodic potentials at the edge, magnetic moments can be finely tuned, realizing diverse magnetic ground states. Furthermore, dynamic control of the edge magnetic moments can be achieved using local probe techniques (e.g., a conducting AFM tip), where the tip-induced potential flips the edge moments at the tip's location. By moving the tip along the edge, one could manipulate the induced reversed magnetic domain.

### 5.3 Atomic vacancies in nanosheets (ongoing)

Sulfur vacancies in a monolayer of MoS<sub>2</sub> have emerged as a pivotal research focus in the field of two-dimensional materials, garnering significant attention due to their profound influence on the electronic and optical properties of the material [117,118,119]. These vacancies, characterized by the absence of sulfur atoms within the crystalline lattice, introduce localized states within the bandgap, thereby affecting charge carrier mobility and recombination dynamics. Understanding the formation, migration, and passivation of sulfur vacancies is essential for tailoring the optoelectronic characteristics of MoS<sub>2</sub> monolayers, offering potential applications in next-generation transistors, photodetectors, and optoelectronic devices.

Using a tight-binding approach instead of DFT for the band structure calculations represents a crucial methodological choice as one of the main downside of DFT is the limitation on the size and complexity of systems due to computational constraints. On the other side, TB models provide a more computationally efficient means of exploring larger configurations. The TB band structure calculations also unlocks the capacity to explore supercell configurations and allows for realistic emulation of a random distribution of defects, without inter-defect interactions due to the periodicity of the system or excessive computation time.

In order to simulate the presence of a sulfur vacancy, the required adjustments were minimal. Specifically, we removed a sulfur atom by modifying the atomic position file, and we altered the on-site energy ( $\epsilon_{3z^2-r^2}$ ) of the neighboring molybdenum atoms surrounding the vacancy from its original value of  $-1.512$  to  $-0.15$  eV to fit the DFT figure 5.7. With this minor modifications, we obtained the band structures visible on figure 5.5. All the sulfur vacancies presented in this section have been generated in the upper sulfur layer.

The first step for these calculations was to verify which supercell size allowed us to avoid the periodicity effect. The comparison between 3x3, 4x4 and 5x5 supercells shown in figure 5.5 with a single sulfur vacancy shows that there still is some interactions as the mid-gap states induced by the defect changes according to the supercell size. Notably, the difference between the 4x4 and 5x5 configurations was considerably smaller than between 3x3 and 4x4 supercells, suggesting that a slightly larger supercell size would be adequately suited.

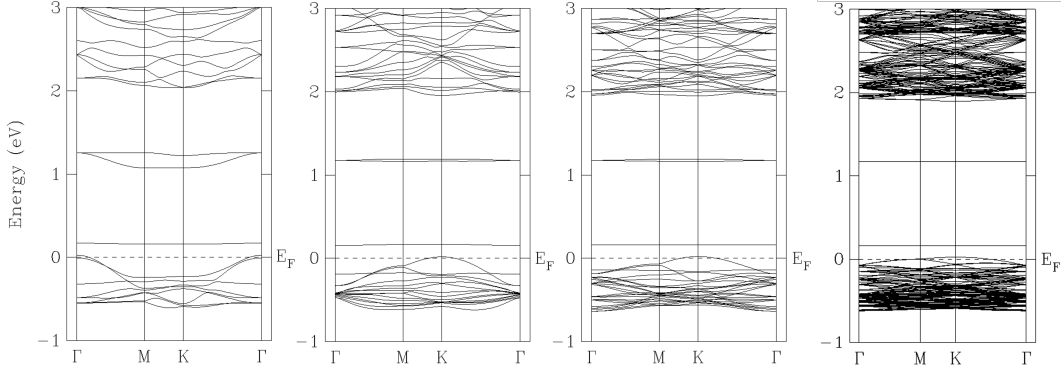


Figure 5.5: Band structure calculations for a single sulfur vacancy for 3x3, 4x4, 5x5 and 10x10 supercell of  $\text{MoS}_2$  monolayer

Considering both computational efficiency and the need for reliability, we decided to use a 10x10 supercell for our upcoming calculations. Several sulfur vacancies concentrations were picked :  $10^{13}/\text{cm}^2$ ,  $5 * 10^{13}/\text{cm}^2$  and  $10^{14}/\text{cm}^2$  as visible on figure 5.6.

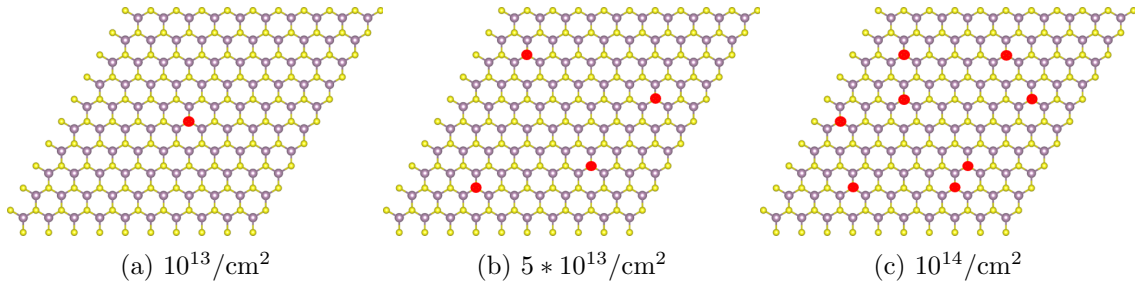


Figure 5.6: Representation of the sulfur vacancies (red dots) for different concentrations of defects on 10x10  $\text{MoS}_2$  supercells.

The band structure for these different concentrations of defaults are visible on figure 5.8. These band structures are in agreement with what can be found in the literature by DFT and experimentally [117,118]. Figure 5.7 shows for example good agreement between the DFT band structure and the TB band structure for a 4x4 supercell of  $\text{MoS}_2$  monolayer. We find the expected defect states appearing in the band gap, increasing with the number of vacancies as visible in figures 5.8a and 5.8b. The distinctive isolated defect states depicted in figure 5.8c originate from the presence of a sulfur di-vacancy induced by our random distribution.

This is corroborated by our simulations, wherein we exclusively introduced a sulfur di-vacancy, as illustrated in figure 5.9. The existence of four states originating from this di-vacancy is supported by DFT calculations (DOS visible on figure 5.10), which also predict

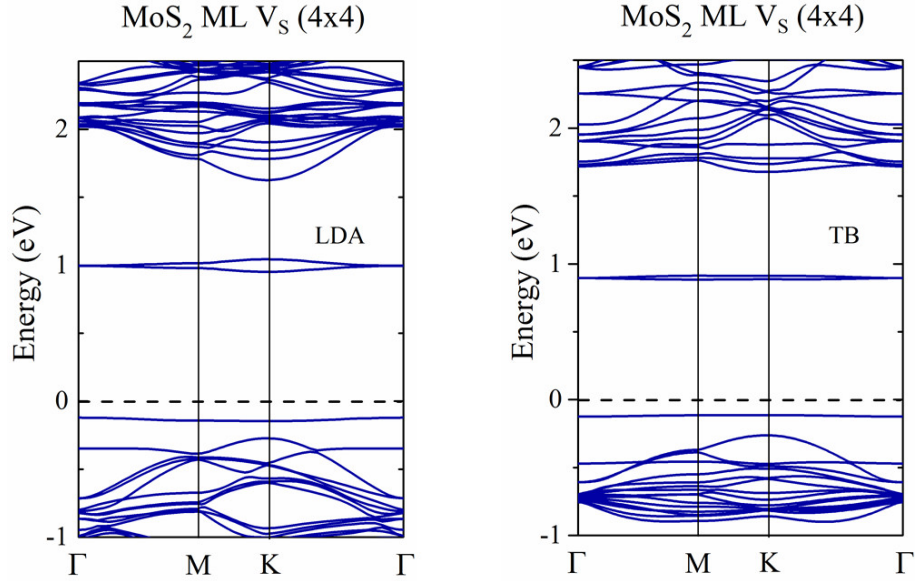


Figure 5.7: Band structures for a 4x4 supercell of monolayer  $\text{MoS}_2$  with a single sulfur vacancy. Left is DFT-LDA, right is tight-binding.

their presence. However, the position of these states in our calculations is not accurate, necessitating further adjustments to the on-site energies to align with DFT calculations.

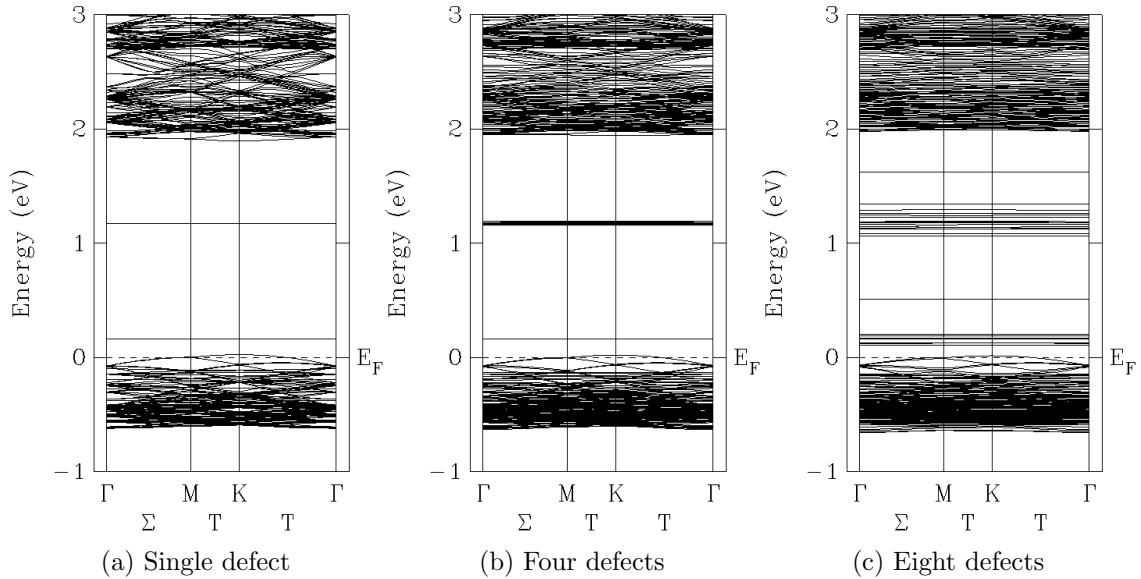


Figure 5.8: Band structures for sulfur vacancies on a monolayer of  $\text{MoS}_2$  for a 10x10 supercell.

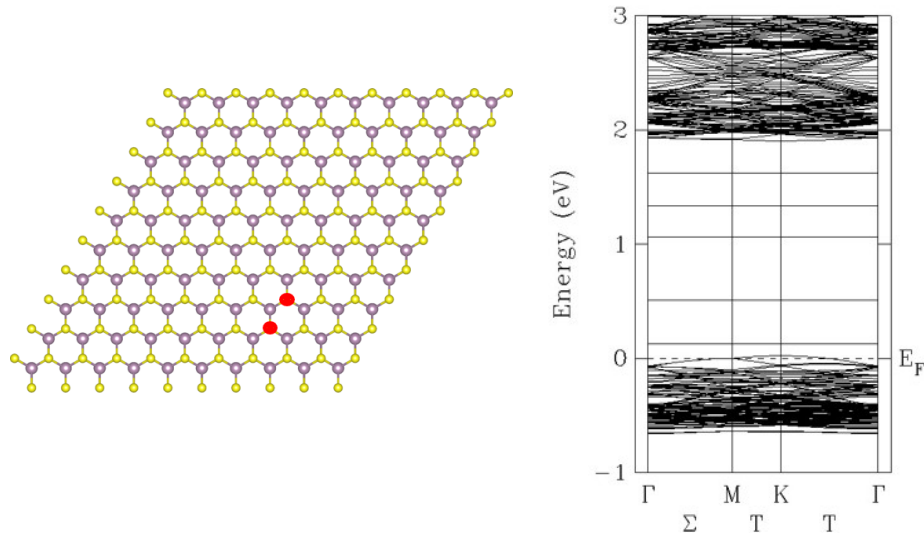


Figure 5.9: Geometry and band structure for a sulfur di-vacancy in a 10x10 MoS<sub>2</sub> supercell.

These results are promising for the use of tight-binding in the study of defects, since all that is needed to obtain correct band structures close to the DFT and experiments is to modify slightly the on-site energies of the atoms near the vacancy. Moreover, using TB allows us to study large supercells (necessary to study 'real' random distributions and different concentrations of defects) in an extremely short computation time compared with DFT.

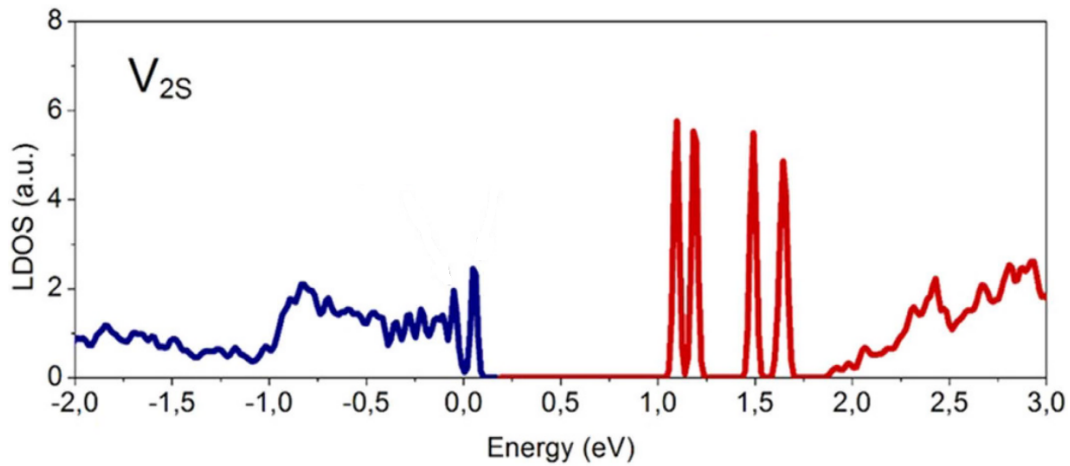


Figure 5.10: Density-of-states for a sulfur di-vacancy, the occupied states are shown by blue and the empty states by red color [120]



# Chapter 6

## Magnetic order in MoS<sub>2</sub> nanoribbons

In the previous chapters, we examined edge magnetism in zigzag nanoribbons of monolayer MoS<sub>2</sub> using both density functional theory and a tight-binding plus Hubbard  $U$  Hamiltonian. Both approaches indicated that a particular band near the Fermi level is significantly affected by spin polarization compared to others. This specific band originates from localized states along the sulfur edge of the nanoribbon and exhibits a dispersion pattern similar to the energy branch found in a linear chain of atoms with first-neighbor interaction. Leveraging this similarity, we have constructed a simplified model to explore the energy variations associated with different spin configurations at the nanoribbon's edge.

### 6.1 One-dimensional atomic chain model

In comparison to unpolarized calculations, spin polarization primarily impacts a single electronic band, denoted as the "magnetic band", within the nanoribbon as visible on figure 4.5. This specific band is associated with states localized along the S edge, crossing the Fermi level with a positive slope. Its dispersion can be succinctly represented by the equation

$$\epsilon(k) = \epsilon + 2\beta \cos(ka), \quad (6.1)$$

where  $a$  denotes the one-dimensional period. This dispersion pattern mirrors what is observed in a one-dimensional atomic chain containing a single orbital on each site. Careful analysis of the DFT nanoribbon wavefunctions reveals that this orbital involves the mixing of the  $3p_y$  and  $3p_z$  orbitals of the two symmetric sulfur atoms of the S edge. The contribution of other orbitals, including those from the Mo atoms, is very small. The mixed  $3p_y - 3p_z$

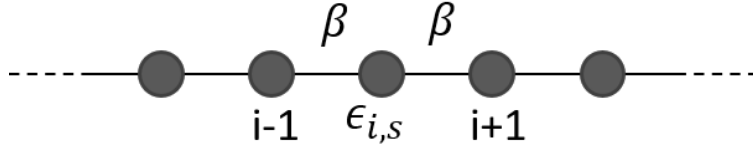


Figure 6.1: Ball-and-stick model of the linear chain described by the Hamiltonian 6.2.  $\beta$  is the hopping parameter and  $\epsilon_{i,\sigma}$  the on-site element for the orbital at the site  $i$  with the spin  $s$ .

orbital ( $\sim 40\%$  -  $\sim 60\%$  in proportion) is perpendicular to the edge direction, denoted as  $x$ . Accordingly, the small dispersion of the magnetic band observed in figure 4.2 can be attributed to a weak  $\pi$  interaction between the mixed  $p$  orbitals on successive sulfur pairs. This  $\pi$  interaction can be modeled by the hopping parameter  $\beta$  indicated in figure 6.1.

The density of states  $\rho(\epsilon_F)$  at the Fermi energy in the nanoribbon is substantial, primarily attributable to the limited dispersion of the magnetic band. Considering the Hubbard interaction  $U_S$ , one could anticipate that the Stoner criterion  $U_S\rho(\epsilon_F) > 1$  holds. As a consequence, the magnetic band is unstable with respect to spin splitting. When examining the spin-polarized band structure, we observe the lifting of spin degeneracy, with the  $\downarrow$  spin band shifting downward while the  $\uparrow$  spin band maintains its crossing with the Fermi level as visible on figure 4.5. Consequently, this illustrates the ferromagnetic nature of the S edge in the MoS<sub>2</sub> nanoribbon.

In this chapter, our attention is directed towards this specific band as we analyze its behavior within the context of the Hubbard model. Our toy model incorporates parameters  $\epsilon$  and  $\beta$  for the dispersion law 6.1, as well as the number of electrons per spin  $n_0$  contained within the band. The parameters, which have been adjusted to match the results of the ab-initio and full TB+U calculations, are outlined in table 6.1. Here,  $\beta$  is one-quarter of the band dispersion between the  $\Gamma$  and  $X$  points of the first Brillouin zone, while  $\epsilon$  corresponds to the average energy of the band. The  $U$  parameter was determined by dividing the 0.52 eV splitting between the spin  $\uparrow$  and spin  $\downarrow$  bands in the full TB+U calculations (visible on figure 4.5) by  $2(1 - n_0) = 0.7$ . Indeed, in a chain model for the ferromagnetic case, the bands are separated by  $U(n_2 - n_1)$  (see figure B.1) and we know from the TB+U calculations that  $n_2 = 1$  and  $n_1 = 0.3$ , giving  $2n_0 = 1.3$ .

The one-dimensional model offers a significant advantage in terms of simplicity. In contrast to the comprehensive TB+U calculations, there is no requirement for a supercell approach with periodic boundary conditions. The calculation of local densities of states in

Table 6.1: TB+U Hamiltonian parameters of the atomic chain that reproduces the dispersion of electronic states localized on the zigzag S edge of MoS<sub>2</sub> nanoribbons. The energy reference is the same as for the on-site energies of table 4.7

$\epsilon$ (eV)	$\beta$ (eV)	$n_0$	$U$ (eV)	$\epsilon_0 = \epsilon - Un_0$ (eV)
-0.8397	-0.04595	0.65	0.7428	-1.3225

a chain with several thousand sites can be carried out efficiently, enabling the exploration of various types of disorder within the magnetic structure.

As in the previous chapter, we have used the mean-field approximation, although the one-dimensional Hubbard model can be solved analytically [121,122,123]. There are three main reasons for keeping with this approximation. Firstly, we aimed to maintain a close alignment with the comprehensive nanoribbon TB+U calculations performed at the Hartree-Fock level. Secondly, predicting the properties of the one-dimensional Hubbard model based on its analytical solution is intricate, involving challenges such as calculating its ground state energy. Thirdly, our primary focus centers on non-periodic magnetic configurations that involve a substantial number of sites, rendering the exact diagonalization of the Hubbard Hamiltonian impossible. Indeed, the complexity of the Hubbard problem increases exponentially with the number of sites in the chain, when it is finite, or with the number of sites contained in a supercell when it is reproduced periodically. Various levels of approximation exist to tackle this issue, with the mean-field approximation being the simplest [124]. At this level, the problem becomes more manageable, especially in cases of perfect ferromagnetic or antiferromagnetic order. A more unique aspect of our study involves the examination of disordered magnetic configurations within the infinite chain, constituting the primary contribution of this chapter.

## 6.2 Magnetic configurations and energetics of the atomic chain

The on-site components of the TB+U Hamiltonian, considering one orbital per site, can be expressed as

$$\epsilon_{i,s} = \epsilon_i + Un_{i,-s},$$

where  $s$  represents spin  $\uparrow$  or  $\downarrow$ , and  $-s$  denotes the opposite spin direction. Here,  $\epsilon_i$  can be further decomposed as  $\epsilon_i = \epsilon_0 + V_i$ , where  $\epsilon_0$  originates from the individual atoms, and  $V_i$  encompasses the crystal field contribution along with any potential local perturbations in the on-site elements induced by an external probe.

In the latter case, the spatial inhomogeneity of the one-dimensional Hubbard chain introduces an additional layer of complexity [125]. In this notation, the Hamiltonian is expressed as

$$H = \sum_{i,s} \left( \epsilon_{i,s} |i, s\rangle \langle i, s| + \beta |i, s\rangle \langle i+1, s| - \frac{1}{2} U n_{i,s} n_{i,-s} \right) \quad (6.2)$$

In equation 6.2,  $n_{i,s}$  corresponds to the occupation of the local density of states (DOS)  $\rho_{i,s}(E)$  on site  $i$  by an electron of spin  $s$ . The cohesive energy is determined as the difference between the total energy of the condensed phase and the total energy of the same number of isolated atoms. Its expression is as follows:

$$E_c = \sum_i \left( \int_{-\infty}^{\epsilon_F} [\rho_{i,\downarrow}(E)(E - \epsilon_{i,\downarrow}) + \rho_{i,\uparrow}(E)(E - \epsilon_{i,\uparrow})] dE + V_i(n_{i,\downarrow} + n_{i,\uparrow}) \right) + U \sum_i (n_{i,\downarrow} n_{i,\uparrow} - n_0^2) + V_r. \quad (6.3)$$

Here,  $n_0$  represents the number of electrons per spin in the isolated atoms, and  $V_r$  signifies the overall contribution from the repulsive potential between pairs of atoms within the condensed phase. The specific form of the expression for  $V_r$  is not critical, as long as we are comparing the energies of the same structure with different magnetic configurations. Similarly, the term involving  $V_i$  vanishes when subtracting the energies of two condensed phases that involve the same set of elements  $V_i$ .

Equation 6.3 holds true with the implicit assumption that each site, on average, contributes  $n_0$  electrons per spin. This condition determines the Fermi energy  $\epsilon_F$  and requires that  $V_i$  remains a constant crystal field term, uniform across all the considered condensed phases. We adopted the following postulate: if a local perturbation is introduced to the on-site energy, or if there is local disorder, such as the presence of a Bloch wall or a small domain with a reversed magnetic moment, the Fermi level  $\epsilon_F$  remains unchanged from that of the unperturbed system. In such cases, the number of electrons is not conserved (which means electrons can come from other bands), and the energy modification is calculated within the grand canonical framework:

$$\Delta\mathcal{E} = \Delta E_c + (\epsilon_0 - \epsilon_F)\Delta N \quad (6.4)$$

where  $\Delta N$  represents the change in the total number of electrons. This change can arise from an external perturbation, if present, or it can be compensated by the other bands that intersect the Fermi level within the actual MoS<sub>2</sub> nanoribbon. The term  $\epsilon_0\Delta N$  in equation 6.4 reflects the alteration in the number of electrons compared to the collection of individual atoms.

With the parameters detailed in table 6.1, the Stoner criterion for magnetic instability,  $U\rho(\epsilon_F) > 1$  as established by Stoner [126], is satisfied. This signifies that the paramagnetic chain (a chain without a spontaneous magnetic order) is unstable when compared to the magnetic chain (a chain with a spontaneous magnetic order). Here,  $\rho(\epsilon_F) = 2/[\pi W \sin(\pi n_0)]$  represents the density of states per atom and per spin at the Fermi energy of the non-magnetic chain, assuming  $n_0$  electrons per spin per atom<sup>1</sup>. In this context,  $W$  denotes the bandwidth and equals  $4|\beta|$ . We have considered both ferromagnetic and antiferromagnetic structures by flipping manually the adequate spins, and self-consistent calculations have been conducted for the occupation numbers of the spin-polarized densities of states within the one-dimensional Hubbard model under the mean-field approximation. The outcomes are visualised in figure 6.2, and the energy gain per atom has been computed for both structures utilising equation 6.3, with the results compiled in table 6.2. Among the three structures studied, the ferromagnetic configuration is found to be the most stable. These calculations have been conducted for a band occupation of  $n_0 = 0.65$ , which corresponds to the value obtained from the full electronic band structure of the MoS<sub>2</sub> nanoribbon. The antiferromagnetic structure is 10 meV higher in energy, in full agreement with the comprehensive TB+U calculations (see chapter 5).

In the antiferromagnetic chain, it's worth noting that the width of both the spin  $\uparrow$  and spin  $\downarrow$  bands is relatively narrow compared with the bandwidth  $4\beta = 0.18$  eV of the non-magnetic chain. The narrowest bandwidth occurs when  $n_0 = 0.5$ , approaching approximately  $4\beta^2/U = 0.011$  eV. If the system is half-filled, the antiferromagnetic structure is the most stable configuration, resulting in  $\Delta E_c = -0.138$  eV per atom, provided that all other parameters remain constant. This is in accordance with the typical behavior of the Hubbard model for systems with half-filled bands, where the chain would be an antiferromagnetic insulator [102].

---

<sup>1</sup>The development linked to this relation can be found in Appendix B

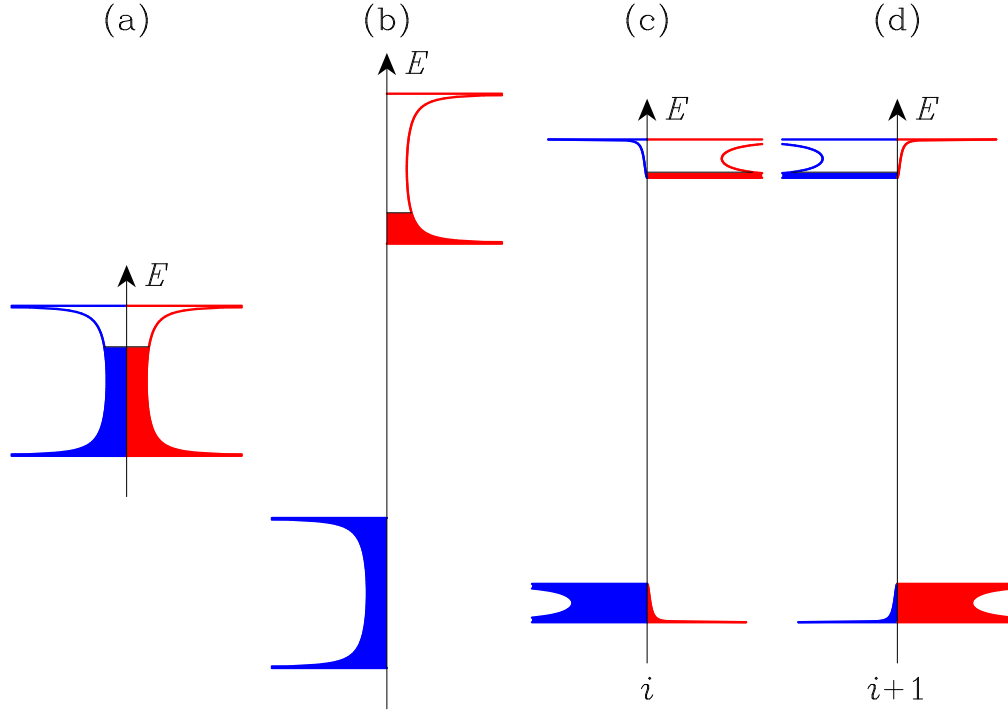


Figure 6.2: Density of states per atom and per spin of the atomic chain for three periodic structures: (a) non magnetic, (b) ferromagnetic, (c) and (d) antiferromagnetic. Spin  $\downarrow$  and spin  $\uparrow$  are represented on the left and right sides of the energy axis, respectively. In the antiferromagnetic case, (c) and (d) display the local DOS on two successive sites  $i$  and  $i+1$  along the chain. For clarity, the width of the spin  $\uparrow$  and spin  $\downarrow$  bands for the antiferromagnetic ordering has been enlarged by a factor of 3.

Table 6.2: Stabilisation energy for ferromagnetic and antiferromagnetic structures of the linear chain compared to the non-magnetic case. The Hamiltonian parameters are those of table 6.1

Structure	non-magnetic	ferromagnetic	antiferromagnetic
$\Delta E_c$ (meV/atom)	0	-62	-47
$n_{\downarrow} - n_{\uparrow}$	0.00	0.70	$\pm 0.67$
$\epsilon_F$ (eV)	-0.7980	-0.6337	-0.5874

### 6.3 Bloch wall and small Bloch domains

The formation energy of a Bloch wall was computed by reversing the spin orientations in half of the atomic chain. Specifically, the occupation numbers  $n_{i,\downarrow}$  and  $n_{i,\uparrow}$  were set to 1 and 0.3, respectively, in one half, and to 0.3 and 1, respectively, in the other half. The occupation numbers of 20 sites on both sides of the Bloch wall were treated as variables. Starting from the initial values of 0.3 and 1, the occupation numbers were adjusted self-consistently based on the local integrated densities of states calculated using equation 3.11b on these sites. The Fermi energy was held constant at the value corresponding to the ferromagnetic order. Upon convergence of the self-consistent loop described earlier, the formation energy of the Bloch wall was computed according to equation 6.4. The summation over  $i$  in Equation 6.3 runs over 60 sites, with 30 on both sides of the interface. This encompassed the  $2 \times 20$  sites surrounding the interface, whose occupation numbers were self-consistently adjusted, along with 10 more-distant sites with fixed bulk occupancies. The result is  $\Delta\mathcal{E} = 5.8$  meV, demonstrating good agreement with calculations performed for the complete MoS<sub>2</sub> nanoribbon where we obtained a domain wall of 6.5 meV (see figure 5.1) [61].

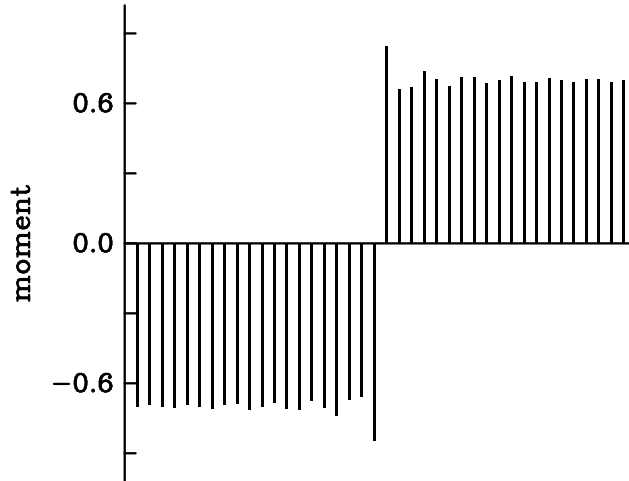


Figure 6.3: Variation of the local magnetic moment calculated along the atomic chain when reversed spins are imposed on both terminal ends of the chain

Figure 6.3 illustrates the fluctuation in the local magnetic moment, calculated as the difference  $n_{i,\downarrow} - n_{i,\uparrow}$ . The bulk value is 0.7. Small damped oscillations are observable in both domains. The maximum moment occurs at the interface, reaching 0.84, while the minimum value follows immediately after, measuring 0.66. There is a slight deficit of electrons,  $\Delta N = -0.21$ , compared to the perfect crystal.

The Bloch domain wall being correctly reproduced and the ground state of the one-dimensional model being ferromagnetic as predicted by the full TB+U calculations, we are focusing on smaller Bloch domains to estimate the excitation energies of different arrangements of the magnetic moments, such as reversed-spin domains of various sizes that are not accessible to full calculations. Small magnetic domains with opposite moments were generated in a manner akin to the Bloch wall. Throughout the chain, the occupation numbers  $n_{i,\downarrow}$  and  $n_{i,\uparrow}$  were set to 1 and 0.3, respectively, except for a chosen set of adjacent sites where their values were interchanged. The occupation numbers for 20 sites on both sides of the domain center were self-consistently calculated, maintaining the Fermi energy at its bulk value. The total energy cost of the defects was computed according to equation 6.4. The results, detailed in table 6.3, show that depending on the domain size, the formation energy ranges between 7.5 and 14.9 meV. For domains with four or more sites,  $\Delta\mathcal{E}$  is close to, but not exactly equal to, two times the energy of a single Bloch wall, indicating a residual interaction between the walls. Figure 6.4 illustrates the local variations in the magnetic moment for both a single spin flip and a domain with four reversed spins. On either side of the domain, oscillations similar to those in figure 6.3 occur. The highest moment values are realized at the two walls, primarily because the site occupation for spin  $\uparrow$  is reduced there compared to the bulk value of 0.3, while the occupation of the majority spin remains close to one. The moment at the single-site domain is -0.98.

A defect in a one-dimensional chain gives rise to localized states above or below the electron band. This is exemplified in the case of small magnetic domains. Appendix C contains a qualitative description of the electronic structure of a single spin flip in the ferromagnetic system. Our premise assumes that the ferromagnetic order results in the formation of two distinct bands. The first band is completely filled, hosting  $n_{b1} = 1$  ( $b$  denoting bulk) electron with a spin  $\downarrow$  per site. Meanwhile, the second band extends up to the Fermi energy  $\epsilon_F$  and contains  $n_{b2} = 0.3$  electrons with a spin  $\uparrow$  per site. We suppose that it is possible to reverse the spin on a single site  $d$  ( $d$  like defect) for instance by applying a local external perturbation  $V$  that shifts the on-site energy on this site. We simplify the problem by considering that the electron occupancies on the neighboring sites of the defect all keep their bulk values. For the lowest band (spin  $\downarrow$ ),  $\epsilon_b = \epsilon_0 + Un_{b2}$  and  $\epsilon_d = V + \epsilon_0 + U_n d2$ . The parameter  $\epsilon_0$  is defined in table 6.1. Given the assumptions made earlier,  $\epsilon_d > \epsilon_b$ , even in the case of a zero or slightly negative perturbation  $V$ . Consequently, the spin defect pushes a localized state above the bulk band, as illustrated in figure C.1. The local density of states on site  $d$  becomes  $\rho_d(E) = A\delta(E - \epsilon_u)$  where  $E = \epsilon_u$  corresponds to the pole of the right-hand side of equation C.3. The localized state shifts up and its weight  $A$  increases when the difference  $\epsilon_d - \epsilon_b$  increases, as for instance by increasing  $V$ . When  $\epsilon_u$  crosses the Fermi energy, the occupation

Table 6.3: Total energy cost from equation 6.4 and total charge variation for small domains with reversed magnetic moment in the ferromagnetic chain. The size is the number of sites in the domain

size	1	2	3	4	5	6
$\Delta\mathcal{E}$ (meV)	7.5	14.9	11.6	9.8	11.9	12.9
$\Delta N$	-0.46	-0.75	-0.09	-0.42	-0.72	-0.01

$n_{d1}$  of the local DOS  $\rho_d(E)$  for spin  $\downarrow$  abruptly falls from 1 down to  $1 - A$ . Similarly, for spin  $\uparrow$  the spin defect induces the downward shifting of a localized state below the upper band (see figure C.1) at the energy  $E = \epsilon_l$  corresponding to the pole of the right-hand side of equation C.1. Here,  $\epsilon_b - \epsilon_d = U(n_{b1} - n_{d1}) - V$ . When  $V$  is not too large, the localized state  $\epsilon_l$  can host a significant fraction of the spin  $\uparrow$  electron on site  $d$ . Hence,  $n_{d2} \approx 1$  and  $n_{d1} \ll 1$  are achieved under the condition  $\epsilon_u > \epsilon_F$ . Treating  $V$  as a tuning parameter, this last condition demands  $V > -0.06$  eV with the parameters of table 6.1. The conditions for a single spin flip are met even in the absence of local perturbation. For  $V = 0$ , the results yield  $n_{d1} = 0.016$  and  $n_{d2} = 0.993$ . By comparison, full self-consistent calculations for a single reversed spin (figure 6.4(a)) give  $n_{d1} = 0.013$  and  $n_{d2} = 0.993$ . It's important to note that this doesn't imply spontaneous spin flip, as the formation of this defect for  $V = 0$  comes with an energy cost outlined in table 6.3 for size 1. Nevertheless, calculations indicate that applying a positive  $V$  on one site will facilitate the formation of the defect.

The local density of states on the site where the spin is reversed is predominantly composed of two peaks, each corresponding to a distinct spin state, accounting for 99% of the distribution. The remaining 1% is dispersed within the continuous bands. The lower-energy peak, drawn down from the upper band, is occupied by an electron with the minority spin, while the other peak remains unoccupied. In the scenario where the domain consists of two sites, four localized states emerge. The lowest (effectively two closely degenerate peaks) can accommodate nearly two electrons with the minority spin.

As discussed in previous chapters, small magnetic domains on the sulfur edge of a MoS<sub>2</sub> nanoribbon appear as the consequence of a local perturbations of the on-site energy. Due to its simplicity, the atomic chain model allows us to investigate this effect in a more systematic way. We applied a Gaussian perturbation of the on-site energy as represented on figure 6.5. The inter-atomic distance was taken as the length unit in such a way that atom  $i$  is located at abscissa  $x_i = i$  along the chain. Then, the Gaussian perturbation of  $\epsilon_i$  is

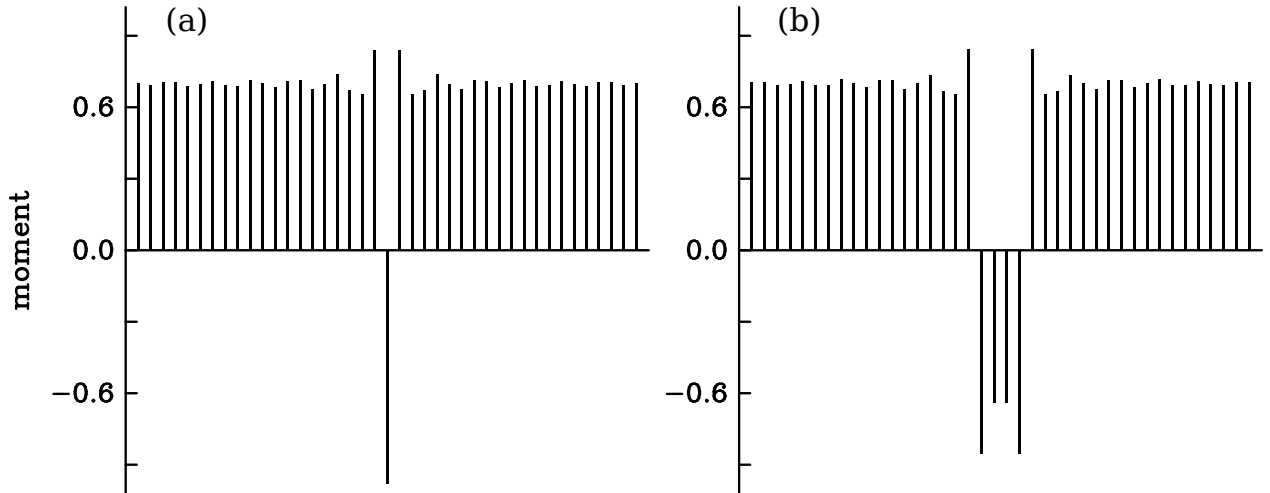


Figure 6.4: Variation in the local magnetic moment calculated along the atomic chain with (a) a single spin flip and (b) a 4-site domain of reversed spin in the ferromagnetic system.

$$V_i = V_0 e^{-(i-i_0)^2/2\sigma^2} \quad (6.5)$$

where  $\sigma$  is a dimensionless parameter. We set  $i_0$  as either an integer number (representing the maximum of the Gaussian on the atomic site  $i_0$ , as illustrated in figure 6.5a) or as a semi-integer number (indicating the maximum of the Gaussian located halfway between two consecutive sites, as depicted in figure 6.5b). The energy of the perturbed chain was first calculated with the perfect ferromagnetic order. Subsequently, the energy was recalculated with the same Gaussian perturbation while reversing the spin on 1, 3, or 5 sites (for integer  $i_0$ ) and 2, 4, or 6 sites (for semi-integer  $i_0$ ). These initial configurations generated a magnetic domain with a reversed moment on 1 to 6 adjacent sites. In all cases, the initial spin configuration maintained symmetry with respect to the maximum of the Gaussian. The energy difference between configurations with a reversed-moment domain and the configuration without the domain was then calculated. The results, influenced significantly by both  $V_0$  and  $\sigma$ , are presented in table 6.4. Even with a small amplitude  $V_0$ , the perturbation stabilizes small domains with reversed moments, underscoring the pronounced impact of both parameters on the domain energetics.

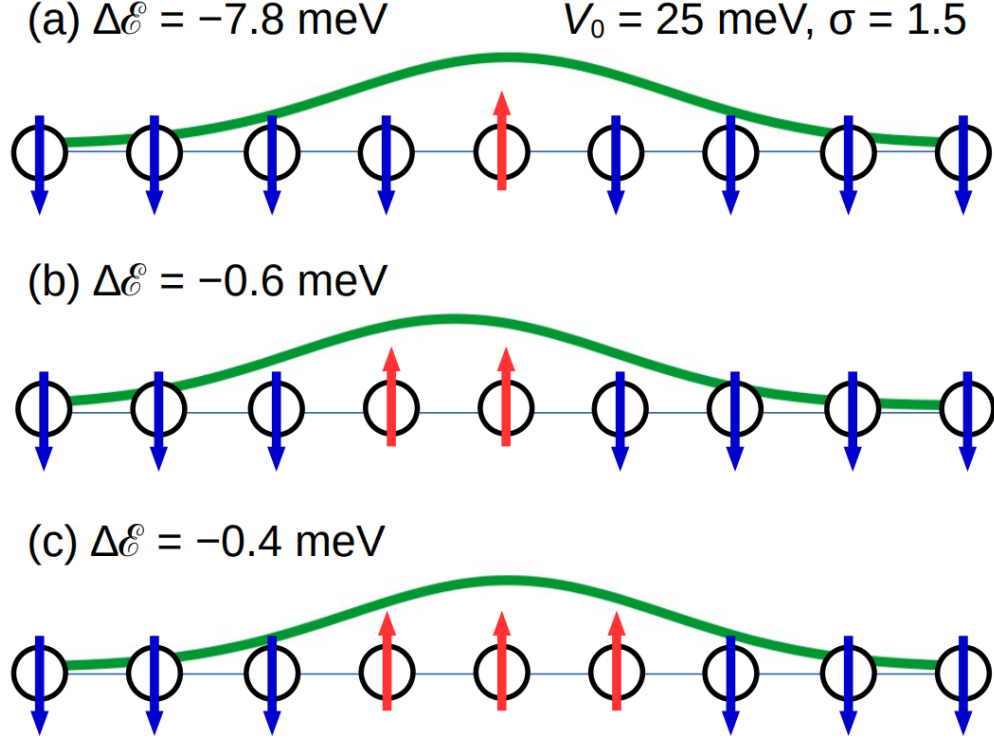


Figure 6.5: Illustration of the results listed in the first row of Table 5. The applied Gaussian perturbation (equation 6.5) is represented by a continuous green line. Its maximum is located either on top of a site (a,c) or at the center of a bond (b). The total energy of domains with reversed moments on (a) 1, (b) 2, and (c) 3 sites is indicated on the left-hand side. Negative values mean more stable configurations than the ferromagnetic chain subjected to the same Gaussian perturbation. Spins down and spins up are represented by blue and red arrows, respectively

By increasing the amplitude  $V_0$  while keeping the width constant ( $\sigma = 1.5$ ), larger domains with reversed spins become energetically favorable compared to the ferromagnetic solution. For instance, at  $V_0 = 0.025 \text{ eV}$ , only domains with reversed spins up to three sites remain stable (with  $\Delta\mathcal{E} = -0.4 \text{ meV}$ ). However, for  $V_0 = 0.075 \text{ eV}$ , the stable domain size extends up to five sites. Similar trends can be observed by increasing the  $\sigma$  parameter at a fixed potential value. Throughout the explored parameter space, the single-site reversed domain consistently appears as the most stable configuration. Nevertheless, the last entry in table 6.4 reveals that domains with two or three reversed moments become competitive when the full width of the perturbation surpasses six bond lengths ( $\sigma > 2.5$ ).

Consistent with our previous calculations, a Gaussian perturbation centered on an atom of the chain (representing an edge site of the MoS<sub>2</sub> nanoribbon) can reverse the spin on that particular atom. In addition to the full TB+U calculations, our systematic study with the one-dimensional model further elucidates the relationship between magnetic domains and

Table 6.4: Formation energy (equation 6.4) in meV for small domains with reversed magnetic moment in the ferromagnetic chain in the presence of a Gaussian perturbation with parameters  $V_0$  and  $\sigma$ . The size is the number of sites in the domain and  $\sigma$  is given in units of the bond length.

	size	1	2	3	4	5	6
$V_0 = 0.025$ meV							
$\sigma = 1.5$	$\Delta\mathcal{E}$ (meV)	-7.8	-0.6	-0.4	+8.8	+12.4	+11.0
$V_0 = 0.05$ meV							
$\sigma = 1.5$	$\Delta\mathcal{E}$ (meV)	-11.1	-8.3	-7.4	-2.4	+1.0	+8.3
$V_0 = 0.075$ meV							
$\sigma = 1.5$	$\Delta\mathcal{E}$ (meV)	-11.3	-10.4	-9.4	-6.5	-3.0	+2.7
$V_0 = 0.05$ meV							
$\sigma = 2.0$	$\Delta\mathcal{E}$ (meV)	-11.3	-9.7	-9.3	-6.4	-4.2	+0.6
$V_0 = 0.05$ meV							
$\sigma = 2.5$	$\Delta\mathcal{E}$ (meV)	-11.4	-10.4	-10.2	-8.4	-7.1	-4.0

the applied perturbation potential in a broader parameter space. If one envisions that the Gaussian perturbation mimics that produced by an STM tip, it becomes conceivable to locally alter the low-temperature magnetic texture of the S edge of the nanoribbon.

# Chapter 7

## Conclusion

In conclusion, this thesis first successfully reproduced the band structures of various TMD crystals using the tight-binding model. Specifically, the band structures of MoS<sub>2</sub> 2H, 3R, and WS<sub>2</sub> 2H in monolayer, bilayer, trilayer, and bulk, along with the one of an asymmetric zigzag MoS<sub>2</sub> nanoribbon passivated with sulfur dimers (considered as the most experimentally stable structure), were accurately reproduced. The accuracy of these band structures was confirmed through comparison with Density Functional Theory (DFT) results, and the observed trends, such as the transition from a direct to an indirect band gap and the variation in the band gap size with the number of layers in planar structures. These outcomes substantiate the reliability of the parameter values presented by Cappelluti *et al.*[27,28] for planar structures, enabling the development of a parameter set suitable for describing the band structure of the nanoribbon on which we have focused, with precise orbital dependencies, particularly concerning the electronic states induced by the ribbon's edges.

Establishing accurate orbital dependencies is crucial for a precise interpretation of the metallic properties exhibited by the nanoribbon. This precision is essential to observe the effects of mechanical stress on the nanoribbon and to understand the associated magnetic phenomena. The successful determination of these dependencies represents a compelling and noteworthy outcome. Leveraging these refined parameters, further calculations on these structures become possible by integrating these values into a Hubbard model. Based on our finely tuned tight-binding (TB) parameters and on Hubbard interaction terms, we investigated a several-nanometer-long ribbon and we calculated the spin domain-wall energy. The observed low domain-wall energy suggests a weak magnetic coupling between the sulfur atoms at the edge, contrasting with zigzag graphene nanoribbons. Additionally, through the introduction of randomly distributed Gaussian potentials, we unveiled the impact of disorder on the magnetic properties. Our findings demonstrate that the magnetic ground states are

highly dependent on potential perturbations, with even slight disorder spanning a few atomic distances altering the orientation of the edge spins. While underscoring the importance of minimizing disorder in MoS<sub>2</sub> nanoribbons, for instance through encapsulation with hexagonal boron nitride, we also highlight the potential for manipulating the spin texture via an applied potential field.

Results from both DFT and TB+U methodologies consistently revealed a significant spin-polarization effect on an electron band crossing the Fermi level, emanating from the S atoms at the edge, compared to other bands. This specific band is recognized as the primary contributor to the magnetic polarization. Remarkably, its dispersion closely mirrors the energy dispersion observed in a linear chain of atoms interconnected through nearest-neighbor interactions. Leveraging this resemblance, we conceptualized a simplified model based on an isolated atomic chain, under the assumption that it captures the primary trends of the physics in the actual system. Through band-structure calculations, we established a one-to-one correspondence between the linear chain of the model and the two-terminal S atoms at the S edge of the nanoribbon. Each pair of S atoms at the edge exhibits a mixing of  $3p_y$  and  $3p_z$  orbitals, imposed by the ribbon geometry and weakly bound by  $\pi$  interactions along the edge.

The linear-chain model was designed to facilitate exploration of the energy landscape for various spin configurations at the nanoribbon edge. With a band occupation of  $2n_0 = 1.3$  electrons in the paramagnetic state, this model validated that the most stable magnetic configuration is indeed the ferromagnetic one, consistent with predictions from comprehensive calculations. Furthermore, the model accurately reproduced the energy required to create a single Bloch wall between two domains with opposite spins, closely aligning with the calculations for the complete MoS<sub>2</sub> nanoribbon (5.8 meV versus 6.5 meV). For smaller domains, we investigated how the formation energy changed with domain size. The simplicity of the atomic chain model enabled a systematic exploration of the effects of local changes in the on-site energy. By introducing Gaussian perturbations and reversing spins in a small segment of the chain centered at the maximum of the Gaussian profile, we calculated and compared energy differences for various configurations. Notably, we observed a reduction in the total energy of the chain perturbed by a Gaussian potential when the spin is reversed in a confined region. The size of the reversed-spin domain and the energy gain were found to be dependent on the Gaussian parameters. This discovery aligns with a similar conclusion drawn from full TB+U calculations, indicating that a local Gaussian perturbation may generate a small domain with reversed spins along the S edge without disrupting the ferromagnetic order over long distances. Anticipating broader applications, we propose that the same one-dimensional model could be employed to examine the magnetic structure of other transition

metal dichalcogenide (TMD) nanoribbons, such as  $\text{WS}_2$ ,  $\text{MoSe}_2$ , and  $\text{MoTe}_2$ .

The depiction of the electronic and magnetic properties of transition metal dichalcogenides, specifically  $\text{MoS}_2$  or  $\text{WS}_2$ , aligns directly with contemporary research. Ongoing investigations explore their potential in micro and nanoelectronics, such as the creation of field-effect transistors [23,39], as well as in spintronics [57], the development of innovative batteries (including hydrogen-based designs) [127,128], and the advancement of photodetectors [129]. A comprehensive understanding of the magnetic and electronic attributes of TMDs is imperative for in-depth material exploration. While studies on TMD layers have been ongoing for years, there is an interest in achieving a precise tight-binding representation of TMD nanoribbons. The proposed one-chain model in this study holds potential significance, particularly in the exploration of spintronic applications as it becomes conceivable to locally alter the low-temperature magnetic texture of the S edge of the nanoribbon.

Therefore, a concise and efficient depiction of band structures is extremely interesting, especially if coupled with a toy model facilitating the examination of the energetics of various spin configurations in nanoribbons. This approach paves the way for advanced calculations that can consider external factors such as mechanical stresses (known to significantly influence  $\text{MoS}_2$  properties), defects, the influence of AFM tips and more. By doing so, we improve the understanding of these unique materials, laying the foundation for the development of devices that harness their remarkable properties. Ultimately, this avenue of research promises not only a deeper understanding of these materials but also the practical realization of devices capitalizing on their exceptional characteristics.



# Appendix A

## Spherical harmonics and matrix elements

For s-, p- and d- orbitals, the real spherical harmonics are defined as :

s-orbital

$$Y_1^s(\theta, \phi) = \sqrt{\frac{1}{4\pi}}$$

p-orbitals

$$Y_1^p(\theta, \phi) = \sqrt{\frac{3}{4\pi}} \sin \theta \cos \phi, \text{ like } x/r$$

$$Y_2^p(\theta, \phi) = \sqrt{\frac{3}{4\pi}} \sin \theta \sin \phi, \text{ like } y/r$$

$$Y_3^p(\theta, \phi) = \sqrt{\frac{3}{4\pi}} \cos \theta, \text{ like } z/r$$

d-orbitals

$$\begin{aligned}
Y_1^d(\theta, \phi) &= \sqrt{\frac{15}{16\pi}} \sin^2 \theta \sin 2\phi, \text{ like } xy/r^2 \\
Y_2^d(\theta, \phi) &= \sqrt{\frac{15}{4\pi}} \sin \theta \cos \theta \sin \phi, \text{ like } yz/r^2 \\
Y_3^d(\theta, \phi) &= \sqrt{\frac{15}{4\pi}} \sin \theta \cos \theta \cos \phi, \text{ like } zx/r^2 \\
Y_4^d(\theta, \phi) &= \sqrt{\frac{15}{16\pi}} \sin^2 \theta \cos 2\phi, \text{ like } (x^2 - y^2)/r^2 \\
Y_5^d(\theta, \phi) &= \sqrt{\frac{15}{16\pi}} (3 \cos^2 \theta - 1), \text{ like } (3z^2 - r^2)/r^2
\end{aligned}$$

When we rotate the coordinates axes from  $oxyz$  to  $OXYZ$ , the spherical harmonics  $Y_{lm}(\theta, \phi)$  transform in a linear combination of the spherical harmonics  $Y_{lm'}(\Theta, \Phi)$  ( $m' = -l, -l+1, \dots, l-1, l$ ) with respect to the new set of axes, where  $\Theta$  and  $\Phi$  denote the polar angles of the vector  $\vec{r}$  in the new coordinates system. From this, it is easy to compute the matrix elements  $Q_{\lambda m}^l$  which connect a real spherical harmonics  $Y_{\lambda}^l(\theta, \phi)$ , with respect to the old set of axes, in terms of the usual spherical harmonics  $Y_{lm}(\Theta, \Phi)$ , with respect to the new set,

$$Y_{\lambda}^l = \sum_{m=-l}^{+l} Q_{\lambda m}^l Y_{lm}(\Theta, \Phi).$$

We assume here that  $OZ$  has a specified direction with respect to  $oxyz$  and we denote by  $l, m$  and  $n$  ( $l^2 + m^2 + n^2 = 1$ ) the direction cosines of the  $OZ$  direction. Furthermore, we choose the  $OY$  direction in the plane ( $xOy$ ); in these conditions the matrix elements  $Q_{\lambda m}^l$  are functions of the direction cosines of the  $OZ$  direction only.

For s-orbital, it is obvious that :  $Q^s = 1$

For p-orbitals, one obtains :

$$Q^p = \begin{bmatrix} \frac{ln-im}{\sqrt{2}(l^2+m^2)^{1/2}} & l & \frac{-ln-im}{\sqrt{2}(l^2+m^2)^{1/2}} \\ \frac{mn+il}{\sqrt{2}(l^2+m^2)^{1/2}} & m & \frac{-mn+il}{\sqrt{2}(l^2+m^2)^{1/2}} \\ \frac{-(l^2+m^2)^{1/2}}{\sqrt{2}} & n & \frac{(l^2+m^2)^{1/2}}{\sqrt{2}} \end{bmatrix}$$

In this last expression, the lines of the matrix are ordered by increasing values of  $\lambda$  and the rows are ordered from  $m = -1$  to  $m = +1$ . Similarly, we have for d-orbitals :

$$Q^d = \begin{bmatrix} \frac{lm(1+n^2)+in(l^2-m^2)}{\sqrt{2}(l^2+m^2)} & \frac{2lmn+i(l^2-m^2)}{\sqrt{2}(l^2+m^2)^{1/2}} & \sqrt{3}lm & \frac{-2lmn+i(l^2-m^2)}{\sqrt{2}(l^2+m^2)^{1/2}} & \frac{lm(1+n^2)-in(l^2-m^2)}{\sqrt{2}(l^2+m^2)} \\ -\frac{mn-il}{\sqrt{2}} & \frac{m(2n^2-1)+in}{\sqrt{2}(l^2+m^2)^{1/2}} & \sqrt{3}mn & \frac{-m(2n^2-1)+in}{\sqrt{2}(l^2+m^2)^{1/2}} & \frac{-mn+il}{\sqrt{2}} \\ -\frac{ln+im}{\sqrt{2}} & \frac{l(2n^2-1)-imn}{\sqrt{2}(l^2+m^2)^{1/2}} & \sqrt{3}nl & \frac{-l(2n^2-1)-imn}{\sqrt{2}(l^2+m^2)^{1/2}} & \frac{-ln-im}{\sqrt{2}} \\ \frac{(l^2-m^2)(1+n^2)-4ilm}{2\sqrt{2}(l^2+m^2)} & \frac{n(l^2-m^2)-2ilm}{\sqrt{2}(l^2+m^2)^{1/2}} & \frac{\sqrt{3}}{2}(l^2-m^2) & \frac{-n(l^2-m^2)-2ilm}{\sqrt{2}(l^2+m^2)^{1/2}} & \frac{(l^2-m^2)(1+n^2)+4ilm}{2\sqrt{2}(l^2+m^2)} \\ \frac{\sqrt{6}}{4}(l^2+m^2) & -\frac{\sqrt{6}}{2}(l^2+m^2)^{1/2}n & \frac{3n^2-1}{2} & \frac{\sqrt{6}}{2}(l^2+m^2)^{1/2}n & \frac{\sqrt{6}}{4}(l^2+m^2) \end{bmatrix}$$



# Appendix B

## Linear chain in mean field approximation

$$H = \sum_{i,s} [(\epsilon_0 + Un_{i,-s}) |i, s\rangle \langle i, s| + \beta |i, s\rangle \langle i+1, s| + \beta |i, s\rangle \langle i-1, s|]$$

where  $i$  denotes the site and  $s$  the spin of the orbital.

$$|\psi_s\rangle = \sum_{j,\sigma} C_{j,\sigma} |j, \sigma\rangle$$

$$\text{where } \langle i, s | j, \sigma \rangle = \delta_{i,j} \delta_{s,\sigma}$$

$$H |\psi_s\rangle = \sum_{i,s} [(\epsilon_0 + Un_{i,-s}) C_{i,s} |i, s\rangle + \beta (C_{i+1,s} + C_{i-1,s}) |i, s\rangle] = E_s |\psi_s\rangle$$

$$(\epsilon_0 + Un_{i,-s}) C_{i,s} + \beta (C_{i+1,s} + C_{i-1,s}) = E_s C_{i,s}$$

1) Non polarised case  $n_{i,s} = n_{i,-s} = n_0$

$$(\epsilon_0 + Un_0) C_{i,s} + \beta (C_{i+1,s} + C_{i-1,s}) = E_s C_{i,s}$$

By Bloch's theorem

$$C_{i+1,s} = C_{i,s} e^{+ika}$$

$$C_{i-1,s} = C_{i,s} e^{-ika}$$

where  $a$  is the periodicity.

$$(\epsilon_0 + Un_0 + 2\beta \cos(ka))C_{i,s} = E_s C_{i,s} \quad \forall i \text{ and } s$$

$$\Rightarrow E_s = \epsilon + 2\beta \cos(ka) \quad \epsilon = \epsilon_0 + Un_0$$

Given  $\rho(E) = \frac{1}{\pi} \int_0^{\pi/a} \delta(E - E(k)) dk = \frac{1}{\pi} \int_{E-E_{min}}^{E+E_{max}} \delta(E - E(k)) \frac{dE(k)}{|E'(k)|} :$

$$\rho(E) = \frac{1}{\pi} \frac{1}{|E'(k)|_{E(k)=E}} = \frac{1}{\pi} \frac{1}{2|\beta|a} \frac{1}{\sin(ka)}$$

Given that the density of states per atom is given by

$$\rho_0(E) = \frac{a}{\pi} \left| \frac{dk}{dE} \right| = \frac{1}{\pi} \frac{1}{2|\beta|} \frac{1}{\sqrt{1 - \left(\frac{E-\epsilon}{2|\beta|}\right)^2}} \quad \epsilon - 2|\beta| < E < \epsilon + 2|\beta|,$$

the Fermi level can be determined by calculating

$$Z_0(E) = \int_{\epsilon_2 - 2|\beta|}^E \rho_0(E) dE = \frac{1}{2} + \frac{1}{\pi} \arcsin \frac{E - \epsilon_2}{2|\beta|}.$$

We can invert the relation to obtain  $E - E(Z_0)$ . We find

$$\frac{E - \epsilon_2}{2|\beta|} = \sin \frac{\pi}{2} (2Z_0 - 1) = -\cos(\pi Z_0),$$

thus  $E = \epsilon_2 - 2|\beta| \cos(\pi Z_0)$ . Replacing  $Z_0$  by  $n_0$ , we obtain

$$E_F = \epsilon_2 - 2|\beta| \cos(\pi n_0)$$

2) Ferromagnetic case  $n_{i,s} = n_1, n_{i,-s} = n_2, n_1 + n_2 = 2n_0$

$$(\epsilon_0 + Un_1)C_{i,s} + \beta(C_{i+1,s} + C_{i-1,s}) = E_s C_{i,s}$$

$$(\epsilon_0 + Un_2)C_{i,-s} + \beta(C_{i+1,-s} + C_{i-1,-s}) = E_{-s} C_{i,-s}$$

Same periodicity, written  $a$ , for both spins.

$$\epsilon_0 + Un_1 + 2\beta \cos(ka) = E_s$$

$$\epsilon_0 + Un_2 + 2\beta \cos(ka) = E_{-s}$$

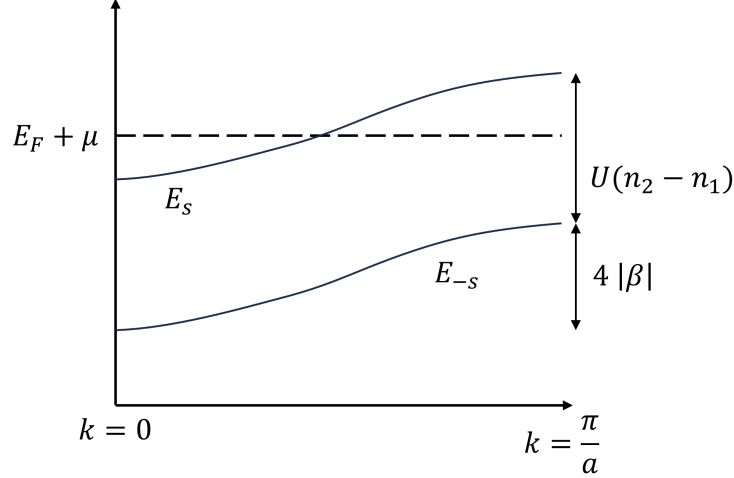


Figure B.1: Representation of the two bands described by a linear chain in mean field approximation for the ferromagnetic case where  $n_{i,s} = n_1$  and  $n_{i,-s} = n_2$ ,  $n_2 > n_1$ .

We find two bands of the same shape, shifted along the E axis as represented on figure B.1.

We can safely presume that  $n_2$  is greater than  $n_1$  without sacrificing generality. Let's take the case  $n_0 > 0.5$ , implying  $n_1 + n_2 > 1$ . In the specific case  $n_2 = 1$  and  $n_1 = 2n_0 - 1$ , the  $E_{-s}$  band is totally filled. The bottom of the  $E_s$  band is higher than the top of the  $E_{-s}$  band. We can then deduce :

$$\epsilon_2 - 2|\beta| > \epsilon_1 + 2|\beta|,$$

where  $\epsilon_1 = \epsilon_0 + Un_1$  and  $\epsilon_2 = \epsilon_0 + Un_2$ , implying

$$U \frac{1 - n_0}{2|\beta|} > 1$$

which is a modified version of the Stoner criterion, a valid expression for the case  $n_0 > 0.5$ .

In these conditions, the Fermi level is given by

$$\begin{aligned} E_F + \mu &= \epsilon_2 - 2\beta \cos(\pi n_1) \\ &= \epsilon_0 + Un_2 - 2|\beta| \cos(\pi n_1) \\ &= \epsilon + U(n_2 - n_0) - 2|\beta| \cos(\pi(2n_0 - 1)) \\ &= \epsilon - U(n_0 - 1) + 2|\beta| \cos(2\pi n_0) \end{aligned}$$

where  $\mu$  is the shift of the Fermi level compared to the non-polarised case :

$$\mu = 2|\beta|[\cos(2\pi n_0) + \cos(\pi n_0)] + U(1 - n_0)$$

3) Anti-ferromagnetic case

$$n_{i,s} = n_1; n_{i+1,s} = n_2 = n_{i-1,s}$$

$$n_{i,-s} = n_2; n_{i+1,-s} = n_1 = n_{i-1,-s}$$

$$\left\{ \begin{array}{l} (\epsilon_0 + Un_2)C_{i,s} + \beta(C_{i+1,s} + C_{i-1,s}) = E_s C_{i,s} \\ (\epsilon_0 + Un_1)C_{i,-s} + \beta(C_{i+1,-s} + C_{i-1,-s}) = E_{-s} C_{i,-s} \\ (\epsilon_0 + Un_1)C_{i+1,s} + \beta(C_{i+2,s} + C_{i,s}) = E_s C_{i+1,s} \\ (\epsilon_0 + Un_2)C_{i+1,-s} + \beta(C_{i+2,-s} + C_{i,-s}) = E_{-s} C_{i+1,-s} \end{array} \right. \begin{array}{l} \text{(B.1a)} \\ \text{(B.1b)} \\ \text{(B.1c)} \\ \text{(B.1d)} \end{array}$$

Thanks to Bloch's theorem, we can take

$$C_{i-1,\pm s} = C_{i+1,\pm s} e^{-2ika}$$

and

$$C_{i+2,\pm s} = C_{i,\pm s} e^{+2ika}$$

The four equations (B.2) then become

$$\left\{ \begin{array}{l} (\epsilon_0 + Un_2)C_{i,s} + \beta(1 + e^{-2ika})C_{i+1,s} = E_s C_{i,s} \\ (\epsilon_0 + Un_1)C_{i,-s} + \beta(1 + e^{-2ika})C_{i+1,-s} = E_{-s} C_{i,-s} \\ (\epsilon_0 + Un_1)C_{i+1,s} + \beta(e^{2ika} + 1)C_{i,s} = E_s C_{i+1,s} \\ (\epsilon_0 + Un_2)C_{i+1,-s} + \beta(e^{2ika} + 1)C_{i,-s} = E_{-s} C_{i+1,-s} \end{array} \right. \begin{array}{l} \text{(B.2a)} \\ \text{(B.2b)} \\ \text{(B.2c)} \\ \text{(B.2d)} \end{array}$$

From (B.2a) and (B.2c) equations

$$\left\{ \begin{array}{l} (\epsilon_0 + Un_2 - E_s)C_{i,s} + \beta(1 + e^{-2ika})C_{i+1,s} = 0 \\ \beta(1 + e^{2ika})C_{i,s} + (\epsilon_0 + Un_1 - E_s)C_{i+1,s} = 0 \end{array} \right.$$

From (B.2b) and (B.2d) equations

$$\left\{ \begin{array}{l} (\epsilon_0 + Un_2 - E_{-s})C_{i+1,-s} + \beta(1 + e^{2ika})C_{i,-s} = 0 \\ \beta(1 + e^{-2ika})C_{i+1,-s} + (\epsilon_0 + Un_1 - E_{-s})C_{i+1,-s} = 0 \end{array} \right.$$

In both cases, we find

$$(\epsilon_0 + Un_1 - E_{\pm s})(\epsilon_0 + Un_1 - E_{\pm s}) = 2\beta^2(1 + \cos(2ka))$$

and, by taking the conjugated complex of these last 2 equations :

$$C_{i,-s}^* = C_{i+1,s}; C_{i+1,-s}^* = C_{i,s}$$

To calculate the coefficient  $C_{i,s}$ ,  $C_{i+1,s}$ , given B.2a, we can deduce

$$C_{i+1,s} = \frac{E - \epsilon_2}{\beta(1 + e^{-2ika})} C_{i,s}.$$

By normalising, we obtain

$$|C_{i,s}|^2 = \frac{E - \epsilon_1}{2(E - \frac{\epsilon_1 + \epsilon_2}{2})}$$

$$|C_{i+1,s}|^2 = \frac{E - \epsilon_2}{2(E - \frac{\epsilon_1 + \epsilon_2}{2})}$$

We have two eigenvalues  $E_{\pm} = \frac{\epsilon_1 + \epsilon_2}{2} \pm \sqrt{(\frac{\epsilon_2 - \epsilon_1}{2})^2 + 4\beta^2 \cos^2(ka)}$ . Knowing that the minimum of  $E_-$  and the maximum of  $E_+$  happen at  $k = 0$  and that the maximum of  $E_-$  and the minimum of  $E_+$  happen at  $k = \frac{\pi}{2a}$ , we can deduce the bandwidth

$$\sqrt{(\frac{\epsilon_2 - \epsilon_1}{2})^2 + 4\beta^2} - \epsilon_1 \quad \text{for } E_-$$

$$\sqrt{(\frac{\epsilon_2 - \epsilon_1}{2})^2 + 4\beta^2} - \epsilon_2 \quad \text{for } E_+$$

The density of states per atom and per spin is given by

$$\rho_s(E) = \frac{1}{\pi} \frac{-|E - \frac{\epsilon_1 + \epsilon_2}{2}|}{\sqrt{-(E - E_1)(E - E_2)(E - \epsilon_1)(E - \epsilon_2)}} \quad \text{for } E_1 < E < \epsilon_1$$

$$\rho_s(E) = \frac{1}{\pi} \frac{|E - \frac{\epsilon_1 + \epsilon_2}{2}|}{\sqrt{-(E - E_1)(E - E_2)(E - \epsilon_1)(E - \epsilon_2)}} \quad \text{for } E_2 < E < \epsilon_2$$

where  $E_1 = \frac{\epsilon_1 + \epsilon_2}{2} - \sqrt{(\frac{\epsilon_2 - \epsilon_1}{2})^2 + 4\beta^2}$  and  $E_2 = \frac{\epsilon_1 + \epsilon_2}{2} + \sqrt{(\frac{\epsilon_2 - \epsilon_1}{2})^2 + 4\beta^2}$ .



# Appendix C

## Spin flip in a ferromagnetic linear chain

We aim to establish a necessary condition for inducing a reversal in the magnetic moment on a single site within an otherwise flawless ferromagnetic linear chain. Our premise assumes that the ferromagnetic order results in the formation of two distinct bands. The first band is completely filled, hosting  $n_{b1} = 1$  ( $b$  denoting bulk) electron with a spin  $\downarrow$  per site. Meanwhile, the second band extends up to the Fermi energy  $\epsilon_F$  and contains  $n_{b2} = 0.3$  electrons with a spin  $\uparrow$  per site. The Hubbard model is used in the mean-field approximation. The first-neighbor interaction parameter is  $\beta$  all along the infinite chain.

We suppose that it is possible to reverse the spin on a single site  $d$  ( $d$  like defect) for instance by applying a local external perturbation  $V$  that shifts the on-site energy on this site. In other words, our objective is to establish conditions such that  $n_{d1} \ll n_{b1}$  and  $n_{d2} \approx 1 > n_{b2}$ . We simplify the problem by considering that the electron occupancies on the neighboring sites of the defect all keep their bulk values. Under these conditions, the local density of states on site  $d$  can be obtained analytically:

$$\rho_d(E) = -\frac{1}{\pi} \text{Im} \frac{1}{\epsilon_b - \epsilon_d - \sqrt{(E + i0 - \epsilon_b)^2 - 4\beta^2}} \quad E < \epsilon_b - 2|\beta|^2 \quad (\text{C.1})$$

$$= \frac{1}{\pi} \frac{\sqrt{4\beta^2 - (E - \epsilon_b)^2}}{(\epsilon_b - \epsilon_d)^2 + 4\beta^2 - (E - \epsilon_b)^2} \quad \epsilon_b - 2\beta < E < \epsilon_b + 2|\beta| \quad (\text{C.2})$$

$$= -\frac{1}{\pi} \text{Im} \frac{1}{\epsilon_b - \epsilon_d + \sqrt{(E + i0 - \epsilon_b)^2 - 4\beta^2}} \quad E > \epsilon_b + 2|\beta| \quad (\text{C.3})$$

Due to the Hubbard term, the on-site energies  $\epsilon_d$  at the defect site and  $\epsilon_b$  at all the other

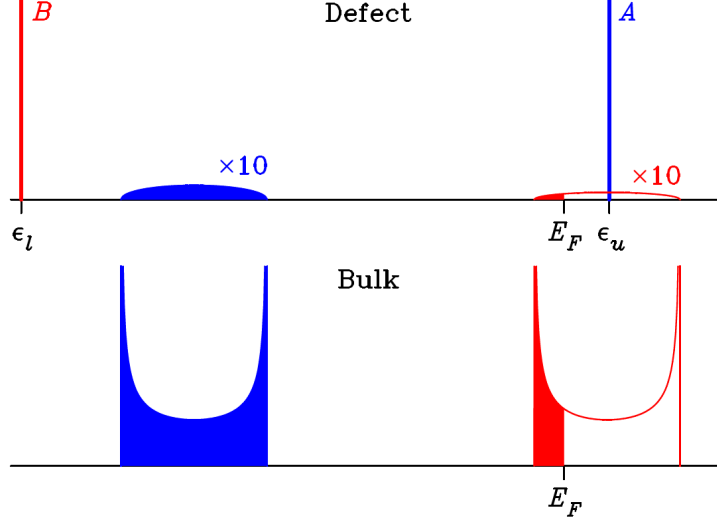


Figure C.1: The local density of states on the spin-flip defect (top part) is compared to the density of states of the ferromagnetic atomic chain far from the defect (bottom part). Blue and red colors correspond to spin  $\downarrow$  and spin  $\uparrow$  states, respectively. A, B correspond to defect states, where the minority spin is occupied (B) and the majority spin is not occupied (A).

sites are spin-dependent. For the lowest band (spin  $\downarrow$ ),  $\epsilon_b = \epsilon_0 + Un_{b2}$  and  $\epsilon_d = V + \epsilon_0 + U_n d2$ . The parameter  $\epsilon_0$  is defined in table 6.1. Given the assumptions made earlier,  $\epsilon_d > \epsilon_b$ , even in the case of a zero or slightly negative perturbation  $V$ . Consequently, the spin defect pushes a localized state above the bulk band, as illustrated in figure C.1. Equation C.3 becomes  $\rho_d(E) = A\delta(E - \epsilon_u)$  where  $E = \epsilon_u$  corresponds to the pole of the right-hand side of equation C.3. The weight (residue) of the localized state is readily obtained as

$$A = \frac{|\epsilon_b - \epsilon_d|}{\sqrt{(\epsilon_b - \epsilon_d)^2 + 4\beta^2}} \quad (\text{C.4})$$

The localized state shifts up and its weight increases when the difference  $\epsilon_d - \epsilon_b$  increases, as for instance by increasing  $V$ . When  $\epsilon_u$  crosses the Fermi energy, the occupation  $n_{d1}$  of the local DOS  $\rho_d(E)$  for spin  $\downarrow$  abruptly falls from 1 down to  $1 - A$ . This value can indeed be small as soon as  $\epsilon_d - \epsilon_b$  exceeds the bandwidth  $4|\beta|$ .

Similarly, for spin  $\uparrow$  the spin defect induces the downward shifting of a localized state below the upper band (see figure C.1) at the energy  $E = \epsilon_l$  corresponding to the pole of the right-hand side of equation C.1. The weight  $B$  of this state is given by the same expression as in equation C.4. Here,  $\epsilon_b - \epsilon_d = U(n_{b1} - n_{d1}) - V$ . When  $V$  is not too large, the localized state  $\epsilon_l$  can host a significant fraction of the spin  $\uparrow$  electron on site  $d$ . Hence,  $n_{d2} \approx 1$  and  $n_{d1} \ll 1$  are achieved under the condition  $\epsilon_u > \epsilon_F$ . Treating  $V$  as a tuning parameter, this last condition demands  $V > -0.06$  eV with the parameters of table 6.1. The conditions for a

single spin flip are met even in the absence of local perturbation. For  $V = 0$ , the results yield  $n_{d1} = 0.016$  and  $n_{d2} = 0.993$ . By comparison, full self-consistent calculations for a single reversed spin (figure 6.4(a)) give  $n_{d1} = 0.013$  and  $n_{d2} = 0.993$ . It's important to note that this doesn't imply spontaneous spin flip, as the formation of this defect for  $V = 0$  comes with an energy cost outlined in table 6.3 for size 1. Additionally, the calculations developed in this Appendix are simplified and, therefore, qualitative. Nevertheless, they indicate that applying a positive  $V$  on one site will facilitate the formation of the defect.

Figure C.1 illustrates the impact of a single-site spin flip on the local density of states. With the parameters relevant for the present study, the majority of states are localized on two distinct peaks: one at  $\epsilon_l$ , fully occupied by spin  $\uparrow$  electrons and the other at  $\epsilon_u$ , totally empty. An electron with spin  $\uparrow$  is trapped below the bulk bands, which reverses the magnetic moment on the defect site. The continuous distributions (equation C.2) contribute for about 1 % of the total spin  $\downarrow$  and spin  $\uparrow$  states. Due to this small but non-zero population, there is a weak probability for an electron at the Fermi energy to tunnel across the defect.



# Bibliography

- [1] K.S. Novoselov et al. “Electric field effect in atomically thin carbon films”. In: *Science* 306 (2004), p. 666. DOI: 10.1126/science.1102896.
- [2] K.S. Novoselov et al. “Two-dimensional atomic crystals”. In: *Proc. Natl. Acad. Sci. USA*. 102 (2004), p. 10451. DOI: 10.1073/pnas.0502848102.
- [3] A.K. Geim and I.V. Grigorieva. “Van der Waals heterostructures”. In: *Nature* 499 (2013), pp. 419–425. DOI: 10.1038/nature12385.
- [4] E.M. Vogel and J.A. Robinson. “Two-dimensional layered transition-metal dichalcogenides for versatile properties and applications”. In: *MRS Bulletin* 40, 7 (2015), pp. 558–563. DOI: 10.1557/mrs.2015.120.
- [5] F. Schwierz. “Graphene transistors”. In: *Nature Nanotechnology* 5 (2010), pp. 5487–496. DOI: 10.1038/nnano.2010.89.
- [6] H. Schmidt et al. “Transport properties of monolayer MoS<sub>2</sub> grown by chemical vapor deposition”. In: *Nano Lett.* 14(4) (2014), p. 1909. DOI: 10.1021/nl4046922.
- [7] J. Basu, J.K. Basu, and T.K. Bhattacharyya. “The evolution of graphene-based electronic devices”. In: *International Journal of Smart and Nano Materials* 3 (2010), pp. 201–223. DOI: 10.1080/19475411.2010.510856.
- [8] Q.H. Wang et al. “Electronics and optoelectronics of two-dimensional transition metal dichalcogenides”. In: *Nat. Nanotechnol.* 7(11) (2012), pp. 699–712. DOI: 10.1038/nnano.2012.193.
- [9] S.Z. Butler et al. “Progress, Challenges, and Opportunities in Two-Dimensional Materials Beyond Graphene”. In: *ACS Nano* 7, 4 (2013), pp. 2898–2926. DOI: 10.1021/nn400280c.
- [10] O.V. Yazyev and A. Kis. “MoS<sub>2</sub> and semiconductors in the flatland”. In: *Materials Today* 18(1) (2015), pp. 20–30. DOI: 10.1016/j.mattod.2014.07.005.
- [11] K.F. Mak et al. “Atomically Thin MoS<sub>2</sub>: A New Direct-Gap Semiconductor”. In: *Phys. Rev. Lett.* 105 (2010), p. 136805. DOI: 10.1103/PhysRevLett.105.136805.

- [12] K.-T. Lam and G. Liang. “Graphene photonics and optoelectronics”. In: *Nature Photonics* 4 (2010), pp. 611–622. DOI: 10.1038/nphoton.2010.186.
- [13] B. Radisavljevic and A. Kis. “Coupled Spin and Valley Physics in Monolayers of MoS<sub>2</sub> and Other Group-VI Dichalcogenides”. In: *Phys. Rev. Lett.* 108 (2012), p. 196802. DOI: 10.1103/PhysRevLett.108.196802.
- [14] M. Liu et al. “A graphene-based broadband optical modulator”. In: *Nature* 474 (2011), p. 7349. DOI: 10.1038/nature10067.
- [15] A.K.M. Newaz et al. “Electrical control of optical properties of monolayer MoS<sub>2</sub>”. In: *Solid State Communications* 155 (2013), pp. 49–52. DOI: 10.1016/j.ssc.2012.11.010.
- [16] D.Y. Qiu, F.H. da Jornada, and S.G. Louie. “Optical Spectrum of MoS<sub>2</sub>: Many-Body Effects and Diversity of Exciton States”. In: *Phys. Rev. Lett.* 111 (2013), p. 216805. DOI: 10.1103/PhysRevLett.111.216805.
- [17] A.P. Nayak et al. “Pressure-induced semiconducting to metallic transition in multilayered molybdenum disulphide”. In: *Nature Comm.* 5 (2014), p. 3731. DOI: 10.1038/ncomms4731.
- [18] Q. Yue et al. “Mechanical and electronic properties of monolayer MoS<sub>2</sub> under elastic strain”. In: *Physics Letters A* 376 (2012), pp. 1166–1170. DOI: 10.1016/j.physleta.2012.02.029.
- [19] H.J. Conley et al. “Bandgap Engineering of Strained Monolayer and Bilayer MoS<sub>2</sub>”. In: *Nano Lett.* 13, 8 (2013), pp. 3626–3630. DOI: 10.1021/nl4014748.
- [20] M. Peña-Álvarez et al. “Single Layer Molybdenum Disulfide under Direct Out-of-Plane Compression: Low-Stress Band-Gap Engineering”. In: *Nano Letters* 15 (2015), pp. 3139–3146. DOI: 10.1021/acs.nanolett.5b00229.
- [21] B. Radisavljevic and A. Kis. “Mobility engineering and a metal–insulator transition in monolayer MoS<sub>2</sub>”. In: *Nature Materials* 12 (2013), pp. 815–820. DOI: 10.1038/nmat3687.
- [22] E.S. Kadantsev and P. Hawrylak. “Electronic structure of a single MoS<sub>2</sub> monolayer”. In: *Solid State Communications* 10 (2012), pp. 909–913. DOI: 10.1016/j.ssc.2012.02.005.
- [23] B. Radisavljevic et al. “Single-layer MoS<sub>2</sub> transistors”. In: *Nature Nanotechnology* 6 (2011), pp. 147–150. DOI: 10.1038/nnano.2010.279.

- [24] F. Zahid et al. “A generic tight-binding model for monolayer, bilayer and bulk MoS<sub>2</sub>”. In: *AIP Advances* 3 (2013), p. 052111. DOI: 10.1063/1.4804936.
- [25] G.-B. Liu et al. “Three-band tight-binding model for monolayers of group-VIB transition metal dichalcogenides”. In: *Phys. Rev. B* 88 (2013), p. 085433. DOI: 10.1103/PhysRevB.88.085433.
- [26] H. Rostami, A.G. Moghaddam, and R. Asgari. “Effective lattice Hamiltonian for monolayer MoS<sub>2</sub>: Tailoring electronic structure with perpendicular electric and magnetic fields”. In: *Phys. Rev. B* 88 (2013), p. 085440. DOI: 10.1103/PhysRevB.88.085440.
- [27] E. Cappelluti et al. “Tight-binding model and direct-gap/indirect-gap transition in single-layer and multilayer MoS<sub>2</sub>”. In: *Phys. Rev. B* 88 (2013), p. 075409. DOI: 10.1103/PhysRevB.88.075409.
- [28] R. Roldán et al. “Momentum dependence of spin-orbit interaction effects in single-layer and multi-layer transition metal dichalcogenides”. In: *2D Mater.* 1 (2014), p. 034003. DOI: 10.1088/2053-1583/1/3/034003.
- [29] Z. Wang et al. “Machine learning method for tight-binding Hamiltonian parametrization from ab-initio band structure”. In: *npj Computational Materials* 7 (2021), p. 11. DOI: 10.1038/s41524-020-00490-5.
- [30] P. Walimbe and M. Chaudhari. “State-of-the-art advancements in studies and applications of graphene: a comprehensive review”. In: *Materials Today Sustainability* 6 (2019), pp. 2589–2347. DOI: 10.1016/j.mtsust.2019.100026.
- [31] Gerardo G. Naumis. “Synthesis, Modeling and Characterization of 2D Materials and Their Heterostructures”. In: *Micro and Nano Technologies, 2020*. Chap. 5 - Electronic properties of two-dimensional materials (77-109). DOI: 10.1016/B978-0-12-818475-2.00005-2.
- [32] X. Ren et al. “Opening of Band Gap of Graphene with High Electronic Mobility by Codoping BN Pairs”. In: *Chem. Res. Chinese Universities* 35 (6) (2019), pp. 1058–1061. DOI: 10.1007/s40242-019-9151-0.
- [33] <https://www.ossila.com/en-eu/pages/molybdenum-disulfide-mos2>. Accessed: 2023-10-26.
- [34] Th. Böker et al. “Band structure of MoS<sub>2</sub>, MoSe<sub>2</sub>, and  $\alpha$ -MoTe<sub>2</sub>: Angle-resolved photoelectron spectroscopy and ab initio calculations”. In: *Physical Review B* 64 (2001), p. 235305. DOI: 10.1103/PhysRevB.64.235305.

- [35] Qing Hua Wang et al. “Electronics and Optoelectronics of two-Dimensional Transition Metal Dichalcogenides”. In: *Nature Nanotechnology* 7(11) (2012), pp. 699–712. DOI: 10.1038/nnano.2012.193.
- [36] W. Zhang et al. “A New Superconducting 3R-WS<sub>2</sub> Phase at High Pressure”. In: *Phys. Chem. Lett.* 12, 13 (2021), pp. 3321–3327. DOI: 10.1021/acs.jpcclett.1c00312.
- [37] S. Deng, L. Li, and M. Li. “Stability of direct band gap under mechanical strains for monolayer MoS<sub>2</sub>, MoSe<sub>2</sub>, WS<sub>2</sub> and WSe<sub>2</sub>”. In: *Physica E: Low-dimensional Systems and Nanostructures* 101 (2018), pp. 44–49. DOI: 10.1016/j.physe.2018.03.016.
- [38] E. Scalise et al. “Strain-Induced Semiconductor to Metal Transition in the Two-Dimensional Honeycomb Structure of MoS<sub>2</sub>”. In: *Nano Res.* 5(1) (2012), pp. 43–48. DOI: 10.1007/s12274-011-0183-0.
- [39] Zhiming M Wang. *MoS<sub>2</sub> : materials, physics, and devices (Lecture notes in nanoscale science and technology, 21)*. Springer, 2014.
- [40] A.R. Klots et al. “Probing excitonic states in ultraclean suspended two-dimensional semiconductors by photocurrent spectroscopy”. In: *Scientific Reports* 4 (2014), p. 6608. DOI: 10.1038/srep06608.
- [41] Sangwan Sim et al. “Exciton dynamics in atomically thin MoS<sub>2</sub>: inter-excitonic interaction and broadening kinetics”. In: *Phys. Rev. B* 88 (2013), p. 075434. DOI: 10.1103/PhysRevB.88.075434.
- [42] I. Kylänpää and H.-P. Komsa. “Binding energies of exciton complexes in transition metal dichalcogenide monolayers and effect of dielectric environment”. In: *Physical Review B* 92 (2015), p. 205418. DOI: 10.1103/PhysRevB.92.205418.
- [43] A. Ramasubramaniam. “Large excitonic effects in monolayers of molybdenum and tungsten dichalcogenides”. In: *Physical Review B* 86 (2012), p. 115409. DOI: 10.1103/PhysRevB.86.115409.
- [44] Nihit Saigal, Vasam Sugunakar, and Sandip Ghosh. “Exciton binding energy in bulk MoS<sub>2</sub>: A reassessment”. In: *Applied Physics Letters* 108 (2016), p. 132105. DOI: 10.1063/1.4945047.
- [45] C. Zhang et al. “Direct Imaging of Band Profile in Single Layer MoS<sub>2</sub> on Graphite: Quasiparticle Energy Gap, Metallic Edge States, and Edge Band Bending”. In: *Nano Lett.* 14(5) (2014), pp. 2443–2447. DOI: 10.1021/nl501133c.
- [46] H.M. Hill et al. “Observation of Excitonic Rydberg States in Monolayer MoS<sub>2</sub> and WS<sub>2</sub> by Photoluminescence Excitation Spectroscopy”. In: *Nano Lett.* 15(5) (2015), pp. 2992–2997. DOI: 10.1021/nl504868p.

- [47] H. Ren and G. Xiang. “Strain-Modulated Magnetism in MoS<sub>2</sub>”. In: *Nanomaterials* 12(11) (2022), p. 1929. DOI: 10.3390/nano12111929.
- [48] K. Kang et al. “The effects of substitutional Fe-doping on magnetism in MoS<sub>2</sub> and WS<sub>2</sub> monolayers”. In: *Nanotechnology* 32 (2020), p. 095708. DOI: 10.1088/1361-6528/abcd61.
- [49] R. Mishra et al. “Long-range ferromagnetic ordering in manganese-doped two-dimensional dichalcogenides”. In: *Physical Review B* 88 (2013), p. 144409. DOI: 10.1103/PhysRevB.88.144409.
- [50] Hui Pan and Yong-Wei Zhang. “Edge-dependent structural, electronic and magnetic properties of MoS<sub>2</sub> nanoribbons”. In: *J. Mater. Chem.* 22 (2012), p. 7280. DOI: 10.1039/C2JM15906F.
- [51] Yafei Li et al. “MoS<sub>2</sub> Nanoribbons: High Stability and Unusual Electronic and Magnetic Properties”. In: *J. Am. Chem. Soc.* 130 (2008), pp. 16739–16744. DOI: 10.1021/ja805545x.
- [52] C. Ataca et al. “Mechanical and Electronic Properties of MoS<sub>2</sub> Nanoribbons and Their Defects”. In: *The Journal of Physical Chemistry C* 115 (10) (2011), pp. 3809–4358. DOI: 10.1021/jp1115146.
- [53] A.R. Botello-Méndez et al. “Metallic and ferromagnetic edges in molybdenum disulfide nanoribbons”. In: *Nanotechnology* 20 (32) (2009), p. 325703. DOI: 10.1088/0957-4484/20/32/325703.
- [54] S. Fu et al. “Enabling room temperature ferromagnetism in monolayer MoS<sub>2</sub> via in situ iron-doping”. In: *Nature Communications* 11 (2020), p. 2034. DOI: 10.1038/s41467-020-15877-7.
- [55] S.-C. Lu and J.-P. Leburton. “Electronic structures of defects and magnetic impurities in MoS<sub>2</sub> monolayers”. In: *Nanoscale Research Letters* 9 (2014), p. 676. DOI: 10.1186/1556-276X-9-676.
- [56] C. Jia et al. “Modulating the magnetic properties of MoS<sub>2</sub> monolayers by group VIII doping and vacancy engineering”. In: *RSC Adv.* 8 (2018), p. 18837. DOI: 10.1039/c8ra01644e.
- [57] E.C. Ahn. “2D materials for spintronic devices”. In: *npj 2D Mater Appl* 4 (2020), p. 17. DOI: 10.1038/s41699-020-0152-0.
- [58] Jeppe V. Lauritsen et al. “Size-dependent structure of MoS<sub>2</sub> nanocrystals”. In: *Nature Nanotechnology* 2 (2007), pp. 53–58. DOI: 10.1038/nnano.2006.171.

- [59] M.V. Bollinger et al. “One-Dimensional Metallic Edge States in MoS<sub>2</sub>”. In: *Phys. Rev. Lett.* 87, 19 (2001), p. 196803. DOI: 10.1103/PhysRevLett.87.196803.
- [60] M. V. Bollinger, K. W. Jacobsen, and J. K. Nørskov. “Atomic and electronic structure of MoS<sub>2</sub> nanoparticles”. In: *Physical Review B* 67 (2003), p. 085410. DOI: 10.1103/PhysRevB.67.085410.
- [61] P. Vancsó et al. “Stability of edge magnetism against disorder in zigzag MoS<sub>2</sub> nanoribbons”. In: *Phys. Rev. Mater.* 3 (2019), pp. 094003.1–8. DOI: 10.1103/PhysRevMaterials.3.094003.
- [62] Y. Hernandez et al. “Graphene and Its Synthesis”. In: *Polymer Science: A Comprehensive Reference* 8 (2012), pp. 415–438. DOI: 10.1016/B978-0-444-53349-4.00216-8.
- [63] N.S. Rajput et al. “Long-term aging of CVD grown 2D-MoS<sub>2</sub> nanosheets in ambient environment”. In: *npj Materials Degradation* 6 (2022), p. 75. DOI: 10.1038/s41529-022-00288-4.
- [64] J. Gao et al. “Aging of Transition Metal Dichalcogenide Monolayers”. In: *ACS Nano* 10(2) (2016), pp. 2628–2635. DOI: 10.1021/acsnano.5b07677.
- [65] D. Soriano et al. “Hydrogenated graphene nanoribbons for spintronics”. In: *Phys. Rev. B* 81 (2010), p. 165409. DOI: 10.1103/PhysRevB.81.165409.
- [66] F. Bonaccorso et al. “An ab initio study on energy gap of bilayer graphene nanoribbons with armchair edges”. In: *Applied Physics Letters* 92(22) (2008), p. 223106. DOI: 10.1063/1.2938058.
- [67] C. Tian et al. “Graphene nanoribbons: Current status and challenges as quasi-one-dimensional nanomaterials”. In: *Reviews in Physics* 10 (2023), p. 100082. DOI: 10.1016/j.revip.2023.100082.
- [68] Daniela ENCIU, George Alexandru NEMNES, and Ioan URSU. “Spintronic devices based on graphene nanoribbons with transition metal impurities. Towards space applications”. In: *INCAS Bulletin* 6, 1 (2014). DOI: 10.13111/2066-8201.2014.6.1.5.
- [69] Y.-L. Lee et al. “Controlling Half-Metallicity of Graphene Nanoribbons by Using a Ferroelectric Polymer”. In: *ACS Nano* 4(3) (2010), pp. 1345–1350. DOI: 10.1021/nn9019064.
- [70] H.U. Özdemir, A. Altıntaş, and A.D. Güçlü. “Magnetic phases of graphene nanoribbons under potential fluctuations”. In: *Phys. Rev. B* 93 (2016), p. 014415. DOI: 10.1103/PhysRevB.93.014415.

- [71] J.P.C. Baldwin and Y. Hancock. “Effect of random edge-vacancy disorder in zigzag graphene nanoribbons”. In: *Phys. Rev. B* 94 (2016), p. 165126. DOI: 10.1103/PhysRevB.94.165126.
- [72] P. Vancsó, I. Hagymási, and L. Tapasztó. “A magnetic phase-transition graphene transistor with tunable spin polarization”. In: *2D Mater.* 4 (2017), p. 024008. DOI: 10.1088/2053-1583/aa5f2d.
- [73] K.E. Çakmak, A. Altıntaş, and A.D. Güçlü. “Effects of random atomic disorder on the magnetic stability of graphene nanoribbons with zigzag edges”. In: *Phys. Rev. B* 98 (2018), p. 115428. DOI: 10.1103/PhysRevB.98.115428.
- [74] K. Bao and J. Zhu. “A brief review of reconstructions and electronic structures of MoS<sub>2</sub> zigzag edges”. In: *J. Appl. Phys.* 132 (2022), p. 080702. DOI: 10.1063/5.0098639.
- [75] A.C. Dias et al. “Band structure of monolayer transition-metal dichalcogenides and topological properties of their nanoribbons: Next-nearest-neighbor hopping”. In: *Phys. Rev. B* 98 (2018), p. 075202. DOI: 10.1103/PhysRevB.98.075202.
- [76] M. DavoodianIdalik, A. Kordbacheh, and F. Velashjerdi. “Structural, electronic and transport properties of an edge terminated armchair MoS<sub>2</sub> nanoribbon with N, O and F atoms”. In: *AIP Advances* 9 (2019), p. 035144. DOI: 10.1063/1.5088551.
- [77] R. Qi et al. “Towards well-defined MoS<sub>2</sub> nanoribbons on a large scale”. In: *Chem. Commun.* 53 (2017), pp. 9757–9760. DOI: 10.1039/C7CC04647B.
- [78] D.I. Miakota et al. “A novel two-step route to unidirectional growth of multilayer MoS<sub>2</sub> nanoribbons”. In: *Applied Surface Science* 619 (2023), p. 156748. DOI: 10.1016/j.apsusc.2023.156748.
- [79] C. Yang et al. “Deriving MoS<sub>2</sub> nanoribbons from their flakes by chemical vapor deposition”. In: *Nanotechnology* 30(25) (2019), p. 255602. DOI: 10.1088/1361-6528/ab0a1d.
- [80] K. Vasu et al. “Clean WS<sub>2</sub> and MoS<sub>2</sub> Nanoribbons Generated by Laser-Induced Unzipping of the Nanotubes”. In: *Small* 11(32) (2015), pp. 3916–3920. DOI: 10.1002/smll.201500350.
- [81] Q. Chen et al. “Atomically Flat Zigzag Edges in Monolayer MoS<sub>2</sub> by Thermal Annealing”. In: *Nano Lett.* 17(9) (2017), pp. 5502–5507. DOI: 10.1021/acs.nanolett.7b02192.
- [82] S.C. Ray S. Sarma. “Magnetic behaviors of single crystal-MoS<sub>2</sub> (MoS<sub>2</sub>-SC) and nanoparticle-MoS<sub>2</sub> (MoS<sub>2</sub>-NP) and bi-layer-MoS<sub>2</sub> thin film”. In: *J. Magn. Magn. Mater.* 546 (2022), p. 168863. DOI: 10.1016/j.jmmm.2021.168863.

- [83] F. Cheng et al. “Controlled growth of 1D MoSe<sub>2</sub> nanoribbons with spatially modulated edge states”. In: *Nano Lett.* 17(2) (2017), pp. 1116–1120. DOI: 10.1021/acs.nanolett.6b04715.
- [84] S. Kurth, M.A.L. Marques, and E.K.U. Gross. “Density-Functional Theory”. In: *Encyclopedia of Condensed Matter Physics* 1 (2005), pp. 395–402. DOI: 10.1016/B0-12-369401-9/00445-9.
- [85] N.M. Harrison. *An Introduction to Density Functional Theory*. Imperial College London, 2001.
- [86] R.G. Parr and W. Yang. *Density-Functional Theory of Atoms and Molecules*. Oxford University Press, 1989. DOI: 10.1002/qua.560470107.
- [87] N.H. March. *Electron Correlation in the Solid State*. World Scientific Press, 1999. DOI: 10.1142/9781860944079.
- [88] J. Callaway and N.H. March. “Density Functional Methods: Theory and Applications”. In: *Solid State Physics* 38 (1984), pp. 135–221. DOI: 10.1016/S0081-1947(08)60313-6.
- [89] G. Kresse and J. Hafner. “Ab initio molecular dynamics for liquid metal”. In: *Phys. Rev. B* 558(R) (1993). DOI: 10.1103/PhysRevB.47.558.
- [90] P.E. Blöchl. “Projector augmented-wave method”. In: *Phys. Rev. B* 50 (1994), p. 17953. DOI: 10.1103/PhysRevB.50.17953.
- [91] J.P. Perdew, K. Burke, and M. Ernzerhof. “Generalized gradient approximation made simple”. In: *Phys. Rev. Lett.* 77 (1997), p. 3865. DOI: 10.1103/PhysRevLett.77.3865.
- [92] H.J. Monkhorst and J.D. Pack. “Special points for Brillouin-zone integrations”. In: *Phys. Rev. B* 13 (1976), p. 5188. DOI: 10.1103/PhysRevB.13.5188.
- [93] J.C. Slater and G.F. Koster. “Simplified LCAO Method for the Periodic Potential Problem”. In: *Phys. Rev.* 94 (1954), p. 1498. DOI: 10.1103/PhysRev.94.1498.
- [94] K. Takegahara, Y. Aoki, and A. Yanase. “Slater-Koster tables for f electrons”. In: *J. Phys. C: Solid State Phys.* 13 (1980), p. 583. DOI: 10.1088/0022-3719/13/4/0168.
- [95] A. Honet L. Henrard and V. Meunier. “Mean-field approximation of the Fermi–Hubbard model expressed in a many-body basis”. In: *AIP Advances* 13 (2023), p. 075210. DOI: 10.1063/5.0153076.
- [96] X. Fan et al. “Modulation of electronic properties from stacking orders and spin-orbit coupling for 3R-type MoS<sub>2</sub>”. In: *Scientific Reports* 6 (2016), p. 24140. DOI: 10.1038/srep24140.

- [97] Tawinan Cheiwchanchamnangij and Walter R. L. Lambrecht. “Quasiparticle band structure calculation of monolayer, bilayer, and bulk MoS<sub>2</sub>”. In: *Phys. Rev. B* 85 (2012), p. 205302. DOI: 10.1103/PhysRevB.85.205302.
- [98] Weijie Zhao et al. “Evolution of Electronic Structure in Atomically Thin Sheets of WS<sub>2</sub> and WSe<sub>2</sub>”. In: *ACS Nano* 7, 1 (2013), pp. 791–797. DOI: 10.1021/nn305275h.
- [99] Daniele Braga et al. “Quantitative Determination of the Band Gap of WS<sub>2</sub> with Ambipolar Ionic Liquid-Gated Transistors”. In: *Nano Lett.* 12 (10) (2012), pp. 5218–5223. DOI: 10.1021/nl302389d.
- [100] H. Kwon et al. “Monolayer MoS<sub>2</sub> field-effect transistors patterned by photolithography for active matrix pixels in organic light-emitting diodes”. In: *npj 2D Materials and Applications* 3 (2019), p. 9. DOI: 10.1038/s41699-019-0091-9.
- [101] K. Andersen, K.W. Jacobsen, and K.S. Thygesen. “Plasmons on the edge of MoS<sub>2</sub> nanostructures”. In: *Phys. Rev. B* 90 (2014), p. 161410. DOI: 10.1103/PhysRevB.90.161410.
- [102] F.M.O Brito et al. “Edge-magnetism in Transition-metal Dichalcogenide Nanoribbons: Mean Field Theory and Determinant Quantum Monte Carlo”. In: *Phys. Rev. B* 105 (2022), p. 195130. DOI: 10.1103/PhysRevB.105.195130.
- [103] D. Szczśniak and S. Kais. “Gap states and valley-spin filtering in transition metal dichalcogenide monolayers”. In: *Phys. Rev. B* 101 (2020), p. 115423. DOI: 10.1103/PhysRevB.101.115423.
- [104] Z.Y. Zhu, Y.C. Cheng, and U. Schwingenschlögl. “Giant spin-orbit-induced spin splitting in two-dimensional transition-metal dichalcogenide semiconductors”. In: *Phys. Rev. B* 84 (2011), p. 153402. DOI: 10.1103/PhysRevB.84.153402.
- [105] E. Ridolfi et al. “A tight-binding model for MoS<sub>2</sub> monolayers”. In: *J. Phys.: Condens. Matter* 27 (2015), p. 365501. DOI: 10.1088/0953-8984/27/36/365501.
- [106] O. Yazyev and M.I. Katsnelson. “Magnetic Correlations at Graphene Edges: Basis for Novel Spintronics Devices”. In: *Phys. Rev. Lett.* 100 (2008), p. 047209. DOI: 10.1103/PhysRevLett.100.047209.
- [107] F. López-Urías et al. “Electronic, magnetic, optical, and edge-reactivity properties of semiconducting and metallic WS<sub>2</sub> nanoribbons”. In: *2D Materials* 2(1) (2015), p. 015002. DOI: 10.1088/2053-1583/2/1/015002.
- [108] F.W.N Silva et al. “Intense conductivity suppression by edge defects in zigzag MoS<sub>2</sub> and WSe<sub>2</sub> nanoribbons: a density functional based tight-binding study”. In: *Nanotechnology* 27 (2016), p. 445202. DOI: 10.1088/0957-4484/27/44/445202.

- [109] E. Ridolfi et al. “Electronic transport in disordered MoS<sub>2</sub> nanoribbons”. In: *Phys. Rev. B* 95 (2017), p. 035430. DOI: 10.1103/PhysRevB.95.035430.
- [110] J. Park et al. “Impact of edge roughness on the electron transport properties of MoS<sub>2</sub> ribbons”. In: *J. Appl. Phys.* 124 (2018), p. 224302. DOI: 10.1063/1.5050383.
- [111] L.R.F. Lima and C.H. Lewenkopf. “Disorder assisted transmission due to charge puddles in monolayer graphene: Transmission enhancement and local currents”. In: *Phys. Rev. B* 93 (2016), p. 045404. DOI: 10.1103/PhysRevB.93.045404.
- [112] A. Bruix et al. “Single-layer MoS<sub>2</sub> on Au(111): Band gap renormalization and substrate interaction”. In: *Phys. Rev. B* 93 (2016), p. 165422. DOI: 10.1103/PhysRevB.93.165422.
- [113] M.-H. Chiu et al. “Determination of band alignment in the single-layer MoS<sub>2</sub>/WSe<sub>2</sub> heterojunction”. In: *Nature Communications* 6 (2015), p. 7666. DOI: 10.1038/ncomms8666.
- [114] Y. Imry and S.-k. Ma. “Random-Field Instability of the Ordered State of Continuous Symmetry”. In: *Phys. Rev. Lett.* 35 (1975), p. 1399. DOI: 10.1103/PhysRevLett.35.1399.
- [115] T. Nattermann. “Spin Glasses and Random Fields”. In: A P Young, 1997. Chap. Theory of the Random Field Ising Model (p.277). DOI: 10.1142/3517.
- [116] F. Igloi and C. Monthus. “Strong disorder RG approach of random systems”. In: *Phys. Rep.* 412(5) (2005), pp. 277–431. DOI: 10.1016/j.physrep.2005.02.006.
- [117] F. Fabbri et al. “Novel near-infrared emission from crystal defects in MoS<sub>2</sub> multilayer flakes”. In: *Nature Communications* 7(1) (2016), p. 13044. DOI: 10.1038/ncomms13044.
- [118] Sai Manoj Gali et al. “Electronic and Transport Properties in Defective MoS<sub>2</sub>: Impact of Sulfur Vacancies”. In: *J. Phys. Chem. C* 124 (2020), pp. 15076–15084. DOI: 10.1021/acs.jpcc.0c04203.
- [119] A. Hötger et al. “Spin-defect characteristics of single sulfur vacancies in monolayer MoS<sub>2</sub>”. In: *npj 2D Materials and Applications* 7 (2023), p. 30. DOI: 10.1038/s41699-023-00392-2.
- [120] P. Vancsó et al. “The intrinsic defect structure of exfoliated MoS<sub>2</sub> single layers revealed by Scanning Tunneling Microscopy”. In: *Scientific Reports* 6 (2016), p. 29726. DOI: 10.1038/srep29726.
- [121] E.H. Lieb and F.Y. Wu. “The one-dimensional Hubbard model: A reminiscence”. In: *Physica A* 321 (2003), pp. 1–27. DOI: 10.1016/S0378-4371(02)01785-5.

- [122] “The Hubbard model at half a century”. In: *Nature Phys* 9 (2013), p. 523. DOI: 10.1038/nphys2759.
- [123] T.A. Kaplan. “Single-band Hubbard model with spin-orbit coupling”. In: *Z. Physik B - Condensed Matter* 49 (1983), pp. 313–317. DOI: 10.1007/BF01301591.
- [124] A. Honet, L. Henrard, and V. Meunier. “Exact and many-body perturbation solutions of the Hubbard model applied to linear chains”. In: *AIP Advances* 12 (2022), p. 035238. DOI: 10.1063/5.0082681.
- [125] V.V. França, D. Vieira, and K. Capelle. “Simple parameterization for the ground-state energy of the infinite Hubbard chain incorporating Mott physics, spin-dependent phenomena and spatial inhomogeneity”. In: *New J. Phys.* 14 (2012), p. 073021. DOI: 10.1088/1367-2630/14/7/073021.
- [126] E.C. Stoner and E.P. Wohlfarth. “A Mechanism of Magnetic Hysteresis in Heterogeneous Alloys”. In: *Philos. Trans. R. Soc. A* 11 (1948), p. 43. DOI: 10.1098/rsta.1948.0007.
- [127] T. Stephenson et al. “Lithium ion battery applications of molybdenum disulfide ( $\text{MoS}_2$ ) nanocomposites”. In: *Energy Environ. Sci.* 7 (2014), pp. 209–231. DOI: 10.1039/C3EE42591F.
- [128] Y. Wang et al. “ $\text{MoS}_2$ -coated vertical graphene nanosheet for high-performance rechargeable lithium-ion batteries and hydrogen production”. In: *NPG Asia Materials* 8 (2016), e268. DOI: 10.1038/am.2016.44.
- [129] H.S. Nalwa. “A review of molybdenum disulfide ( $\text{MoS}_2$ ) based photodetectors: from ultra-broadband, self-powered to flexible devices”. In: *RSC Advances* 10 (2020), pp. 30529–30602. DOI: 10.1039/D0RA03183F.